Carrier Dynamics in Single Semiconductor Nanocrystals

Pin-Hao (Benny) Sher
New College, Oxford

A thesis submitted for the degree of
Doctor of Philosophy
in the University of Oxford

Trinity Term 2009

Supervised by
Dr. Jason Smith
Department of Materials

ABSTRACT

Carrier Dynamics in Single Semiconductor Nanocrystals

Pin-Hao (Benny) Sher

New College, Oxford
Department of Materials, University of Oxford
A thesis submitted for the degree of Doctor of Philosophy in the University of Oxford

Trinity Term 2009

Power law behaviour in the fluorescence intermittence (blinking) of single semiconductor nanocrystal resulting from its unique carrier dynamics is investigated in this research. A neutral or ionised NC is generally accepted as the mechanism leading to a fluorescence on- or off-state. What is unclear is how the NC become ionised, then what happens to the ejected carrier and how it returns to the NC that leads to the distinct power law dynamics. Theoretical models attempting to elucidate the carrier dynamics can be broadly divided into two groups, namely, a charge tunnelling model or a diffusion based (either in energy or space) model. These two models differ mainly in the prediction of power law dynamics at short time regime. The tunnelling model suggested a constant and continuous power law over all time regimes whereas the diffusion model predicts a change in power law exponent at a critical time tc.

In light of the difference from the models, we attempt to measure the power law dynamics over the widest possible time range. We observed the multi-exponential characteristic of a Time-Resolved Photoluminescence (TRPL) decay in NCs actually contains a power law tail, this leads us to think it is related to the same mechanism that governs the blinking power law. A three level Monte Carlo model assuming a power law dependent trapping time provides a link between the TRPL decay and the blinking statistics. The power law exponent extracted from the TRPL tail is found to be similar to its blinking off-time power law exponent in some samples. The time gap between TRPL decay and blinking statistics is filled by calculating the autocorrelation function from the same intensity time trace used in blinking analysis. Combining the three experimental methods we are able to measure power law dynamics over 10 decades in time. Our results provide evidence in support of both the tunnelling model and the diffusion model suggesting both mechanisms may be involved in the real physical world.

An attempt to embedded single NCs in a ZnO thin film will be discussed. The idea is to reduce local disorder in the NC surrounding environment thereby providing surface passivation to the NCs.

ACKNOWLEDGMENT

I am very grateful to thank my supervisor, Dr. Jason Smith, it is your “Non-Blinking” support and guidance that makes this thesis possible.

I would like to thank all my colleagues from the Photonics Nanomaterials Group. It is an enjoyable time working with all of you, wish you all the best.

To my family with love, without your support and encouragement I won’t be who I am and where I am.

To my lovely girlfriend who is brave enough to become my fiancées, your love and your company makes all the difference. I love you!

Praise the Lord for your wonderful creations, particularly nanomaterials for they truly are one of a kind.
"For since the creation of the world God's invisible qualities-his eternal power and divine nature-have been clearly seen, being understood from what has been made, so that men are without excuse." Romans 1:20

CONTENTS

ABBREVIATIONS

NC	Nanocrystals
TRPL	Time Resolved Photoluminescence
QDQW	Quantum Dot Quantum Well
SPAD	Single Photon Avalanche Detector
DAQ	Data Acquisition
APD	Avalanche Photo Diode
PL	Photoluminescence
FWHM	Full-Width-Half-Maximum
TAC	Time-to-Amplitude Converter
SIMS	Secondary Ion Mass Spectrometry

Chapter 1
Introduction

Nanotechnology can be broadly defined as the manipulation of materials at atomic level, at such small size scale nanomaterials of the same composition as its bulk counterparts can have very different properties. For example, carbon atoms can be arranged into sheets as in graphite where the bulk material is “soft” or the sheet can be rolled to form a nanotube where it becomes tougher but lighter than steel. The special material properties have tremendous commercial value such as the sporting equipment industry is already utilizing nanotubes to make stronger and lighter racquets. On the other hand, to understand and explain why nanomaterials have such unique properties requires quantum physics, at the same time nanomaterials provides a system for us to test experimentally the fundamental science predicted by quantum mechanics. Owing to these revolutionary potential in the material world, nanotechnology is a key research area both in the scientific and in the commercial community. Quoting from an independent organisation, the European patent office[1], “The three most likely transformations and overlapping facets of the technology revolution that will dominate the first half of this century are genetics (biotechnology), nanotechnology and robotics (artificial intelligence).” Quantum dots is a nanomaterial that branches between two of these three facets, the study of quantum dots itself belongs to nanotechnology but it also finds applications in

biotechnology. Quantum dots refers to nanoscale semiconductor particles that exhibit a “quantum size effect”, where its energy bandgap scales with the size of the dot. Nanocrystal (NC) is a special class of quantum dot that are grown using colloidal chemical synthesis of crystalline semiconductor nanoparticles.

1.1 Nanocrystal applications

Semiconductor’s bandgap is a forbidden energy gap arising from the periodical crystal structure where no electron state exist. Valance band is the highest energy level below the bandgap that are filled with electrons bonded to crystals atoms. The conduction band is the lowest energy level above the bandgap that consist of free electrons. Electrons in the valance band have a finite probability to be thermally excited to the conduction band at temperature above absolute zero. Once excited the electron leave a *hole* in the valance band, the mobile electrons and the hole left behind, named intrinsic carriers, both contribute to the electrical conductivity. The concentration of thermally excited intrinsic carriers, C_{ic}, hence the electrical conductivity is proportional to the ratio between width of bandgap (E_g) and temperature (T) as $C_{ic} \propto exp(-E_g/K_bT)$, where K_b is the Boltzmann constant. On the other hand, optically generated electron-hole pair requires the absorption of a photon with energy above the bandgap, recombination of the electron-hole pair will then generate a second photon of energy defined by the bandgap. The width of the bandgap is no doubt the most important parameter that determines the electrical and optical properties of semiconductor materials. In semiconductors of macroscopic sizes, this gap is generally fixed by the material’s identity but maybe slightly tuneable by adjusting the material composition. Nanoscale quantum dots provide another degree

of freedom in bandgap engineering. Once the physical size of the quantum dot becomes comparable to or smaller than the natural length scale of the electron-hole pair (Bohr radius) the energy spectra is adjusted as a result of the presence of particle boundaries, with a smaller quantum dot size the energy gap increases.

The ability to engineer bandgap width by controlling the quantum dot sizes opens up new opportunities in semiconductor optoelectronic devices. Quantum dots can be fabricated either by epitaxial growth method or by chemical synthesis method, however the fact that epitaxial growth requires high cost vacuuming equipment and the dots need to grow on a substrate both imposed additional restrictions on applicability. On the other hand, colloidal nanocrystals are much cheaper to produce in large scale, have more freedom in structure and shape control, and its free-standing nature is more desirable from the application's aspect.

Cadmium Selenide (CdSe) is probably the most widely studied nanocrystal in the field owing to the reproducible synthesis recipe producing nanocrystals with high quantum yield (QY). Typical QY for commercially available NCs are ~50% but can be as high as 80% for some NCs. CdSe NCs can cover the entire visible spectrum at different nanocrystal sizes. Bulk CdSe has a direct bandgap of 1.74 eV that is equivalent to 713 nm while CdSe nanocrystals have bandgap ranging from 1.84 eV (674 nm) at nanocrystal size around 10 nm, to 3.65 eV (340 nm) at nanocrystal size around 1 nm[2]. The study of NC carrier dynamics using optical spectroscopy methods base on CdSe NCs are facilitated by the high sensitivity of silicon-based detectors at these wavelength range. Lead Sulphide (PbS) is another common NCs that emits in the NIR (≥800nm). Proper surface passivation is essential for high quantum yield and photostability; NCs are usually passivated by capping an inorganic shell outside the NC core that forms a core/shell structure, e.g. CdSe/ZnS.

The core/shell NC can be further passivated around the surface by organic ligands, besides passivation, the ligands will functionalised NCs for solubility or provide functional groups for binding to other molecules.

The characteristics of NC make it a strong candidate for biological labelling and could potentially replace the organic dyes that are current in use. The continuous absorption band towards shorter wavelength permits freedom in the choice of excitation source as opposed to the fixed excitation band that is close to the emission band in organic dyes. Selection of an excitation wavelength far from the emission wavelength results in easy filtering of excitation light. NCs of different size can be excited by a common source, combining this with the symmetric and narrow emission spectrum of NCs it is possible to create a full colour image of tagged biological cells. On the other hand, the improved photostability of NCs over organics dyes, that is, NCs photobleach much slower than dyes make it possible to tag smaller bio-molecule such as DNA using a single NC. However, as it is well known that single NC emission will blink between a binary on and off state, this seriously hinders the single NC for tagging applications. In addition, the non-single exponential decay of NC photoluminescence complicates the interpretation on time-resolved experiments with NC tagged bio-molecules[3]. We will discuss in later chapter that the non-single exponential decay of NC is related to blinking.

Bandgap engineering capability at the visible spectrum forms the basis for NC's impact on light emitting devices such as LED or laser diodes (LD). An intuitive scenario is to use NCs as a new type of tunable phosphor, by incorporating NCs of different size that emits in the red, blue and green in a polymer composite then deposit the composite on top of a blue or UV LED, it is possible to produce a white light LED. However the self-absorption of emission from smaller NCs by larger NCs

results in low overall device efficiency. Such scheme is a good proof of principle for research purposes but may have little commercial value due to the limited advantage over existing technology. However a small “magic-sized” CdSe NC (~1.5 nm) that is energetically favorable to grow shows a broad emission over the whole visible spectrum. Investigations have revealed interesting dynamics in these magic-sized NCs and it may have practical advantages in light emitting device industry[4-10]. The real advantage is to explore the electroluminescence of NCs in order to fabricate active devices. In such an arrangement the bandgap tunability of NCs provides an extra degree of freedom over bulk materials. For example, realization of green laser diode is hindered by no suitable material with desired bandgap. Although it is possible to modify the bandgap of GaN towards longer wavelength by including Indium to form InGaN, but to reach the “pure green” wavelength at 532 nm excessive amount of Indium is required and the efficiency of the device will decreases as the Indium concentration increases. The tailorable bandgap of colloidal CdSe NCs or epitaxially grown III-V QDs may shine new light in solving the material problem for green solid state lasers. In addition, the higher density of bandedge states for QDs may in principle reduce the lasing threshold and the large spacing of energy levels could improve temperature stability. Nevertheless QD based light emitting device will suffer from a fundamental problem named “statistical aging” where the ensemble of QDs undergoes a reversible photobleaching process[11], in other words, gradual degrade of overall device performance will happen over time for purely statistical reasons. This aging again roots from the power law dynamics seen in blinking phenomenon.

Photovoltaic is another area that takes advantage of the size dependent NC bandgap. By using a stack of cascaded layers of NCs each tuned to absorb a segment

of the solar spectrum, the theoretical conversion limit can reach about 66%. In addition, by dispersing NCs in organic semiconductor polymer matrix such as MEH-PPV it is possible to produce flexible solar cells. However, multiexciton generation by NCs absorbing a photon of energy higher than the bandgap is perhaps the most valuable property of NCs owing to the enhanced photocurrent. After all, having an in depth understanding on the carrier dynamics in NCs is valuable if not essential to optimise the device performance.

1.2 Nanocrystal growth

Epitaxial quantum dots are grown by a physical method that involves high energy input and are usually performed under a high vacuum environment. Examples of physical process include molecular-beam-epitaxy (MBE) and metalorganic-chemical -vapour-deposition (MOCVD), both methods involve vapor phase deposition and hence the high energy and high vacuum requirement. The formation process is termed Stranski-Krastinow (S-K) growth where several monolayers of two highly lattice-mismatched semiconductor materials are deposited one on top of another, quantum dot islands are formed to minimize the strain contained in the film. The growth of the island can continue coherently without forming dislocations until certain critical strain energy density is reached; this imposed a limit on the size of QD islands. Although such layer by layer growth at the atomic level can form quantum dot structures with very few defects, its application is limited due to the high cost in growth equipment and the restrain of QDs by the substrate.

Most epitaxial quantum dots are III-V semiconductors, chemical synthesis of colloidal III-V nanocrystals are more difficult due to its more covalent bonding and

higher synthesis temperature required. On the other hand II-VI semiconductor nanocrystals can be grown using a chemical synthesis method. As a comparison, III-V colloidal nanocrystals will require a reaction time of several days as opposed to a more immediate reaction in II-VI nanocrystal. The preparation of high quality and nearly monodisperse organically passivated NCs involve pyrolysis of metal-organic precursors in hot coordinating solvents (~150-350^{o}C). The growth process follows a model developed by La Mer and Dinegar in 1950, the initial nucleation is triggered by injection of precursors that raised its concentration above nucleation threshold, nuclei are formed to partially relieve the supersaturation. The nuclei will grow instead of forming new nuclei provided that further addition of precursors is controlled below the threshold. Restraining the duration of nucleation is the key to grow NCs with small size distribution. Following the nucleation stage when the precursor concentration are sufficiently depleted, the Ostwald ripening process begins. During this process the high surface energy of smaller particles encourages it dissolution, this will then promote further growth of larger particles to minimize the overall system energy. Careful control of growth reaction usually yields a size dispersion of about 10-15%. Post-processing can further minimize this size dispersion down to ≥5% at the cost of reduced yield rate. Typically this is done by titrating NC solution with a polar nonsolvent (usually methanol). The larger particles will precipitated out before the smaller particles, it is than collected by centrifuging the solution, this process can be iterate by redissolving the precipitate and precipitate again.

The growth of bare NCs (core only) passivated only by organic ligands usually results in a poor photoluminescence performance, that is, low quantum yield (~10%) and a signature of deep trap luminescence in the photoluminescence spectra.

Although later reports suggested a modified growth recipe utilizing a three component HAD-TOPO-TOP mixture can increase the quantum yield up to 50% at room temperature, it is a usual practice to cover the NC core with a wide-bandgap inorganic shell layer to form a core/shell structure. The inorganic shell served to passivate the NC core that results in a high quantum yield and the elimination of surface trap related luminescence from the spectra. The growth of the shell layer is conducted in a similar setup as for the core; in order to promote the heterogeneous nucleation of the shell over the core rather than the homogeneous nucleation of the shell material, the surface energy of the core and shell materials must be sufficiently similar. Some typical core/shell structures with CdSe core are CdSe/(ZnS,ZnSe,CdS) (REF), among all CdSe/ZnS is the most common type that is commercially available. One may expect the larger bandgap of a ZnS shell over the CdSe core to provide better confinement of the carriers, therefore isolating the electron-hole pair from the surrounding environment and hence provide an improved surface passivation. In fact this may be true to some extend since CdSe/ZnS NCs is relatively robust again photobleaching and it generally has a high photoluminescence quantum yield. However, even with an inorganic shell surrounding the core, the organic ligands outside the shell still plays an important role in the luminescence properties of a core/shell NC, this suggested there are still some imperfection in the passivation. One possibility is due to the large lattice mismatch between ZnS and CdSe (10.6%) that resulted in stacking fault type of defects during shell layer growth. This is supported by a systematic study by Daboussi et al.[12] who reported growing up to five monolayers of ZnS over CdSe core and found out that the maximum quantum yield is achieved with ~1.3 monolayers of ZnS whereas thicker layers of shell tend to degrade rather than improve. They attributed the decrease in quantum yield to arise

from defects creating new nonradiative relaxation path for the electron-hole pair. Some groups has attempted to make use of other shell materials that poses a smaller lattice mismatch such as ZnSe, Reiss et al. claimed as high as 85% quantum yield from CdSe/ZnSe NCs. They then continue to explore the possibility of taking advantages from both worlds by growing a core/multishell structure, namely, CdSe/ZnSe/ZnS.

Despite the high quantum yield figures reported, all colloidal NCs still suffer from luminescence blinking until in 2008 Mahler et al. and Chen et al. simultaneously reported on growing thick CdS shell over CdSe core with suppressed blinking. Mahler et al. grew up to 7 monolayers of CdS shell using standard methods and claimed to obtain QY of the order of 70%. However what is new from the report is the gradual suppression of blinking with increasing shell thickness, in sharp contrast to previous report on CdSe/ZnS where no correlation is found between shell thickness and blinking statistics. For NCs with 7 shell layers, they found no *off* events longer than 30 ms although blinking events are still present at time scales below the millisecond range. Furthermore, Chen et al. grow up to 19 monolayers of CdS shell over CdSe core using the SILAR (Successive Ion Layer Absorption and Reaction) method; however the QY is lower, only at 40%. The SILAR method somewhat mimics the layer-by-layer growth as in epitaxial QDs, it is a slow growing method that takes a few days to grow a complete core/shell structure. Both groups has the same strategy that is to make use of the small lattice mismatch between CdSe and CdS (4%) to grow thick shell layers without introducing defects. Although the increased shell layers in Chen's report may have a hint of improvement on blinking suppression over Mahler's NCs, blinking is yet to be removed completely. Chen also attempted to incorporate ZnS in to their shell structure by alloying CdS and ZnS

between the innermost CdS shell and the outermost ZnS shell, however such attempt resulted in even lower QY (10%) suggesting the introduction of ZnS created more defect sites in the shell which turn into extra nonradiative paths. However a recent report by Wang et al. suggested that by alloying the core with shell material to produce a gradual confinement potential resulted in a completely non-blinking NC. The structure of their NC is an alloyed core of CdZnSe that gradually blend into a ZnSe shell. The ensemble quantum yield is about 50%. These NCs have an unusual multi-peak PL spectrum as opposed to a single peak PL commonly found in other NCs.

1.3 Background on NC Photoluminescence

Electrons bonded to isolated atoms have discrete energy levels. When many of those atoms are brought together in close vicinity to form a solid such that the interatomic distance is comparative to the atomic size, the outer atomic orbitals will overlap and interact with each other resulted in bands of electronic levels. The inner atomic orbitals will not interact and remains discrete thus forming bandgaps in the overall solid energy levels where no wavelike electron orbitals exist. The distinction between metal, semiconductor and insulator is how the energy bands are filled with electrons. Metals have an energy band partly filled with electrons where the electrons are free to move thus can conduct electricity. In insulators and semiconductors, the allowed energy bands are either filled or empty at absolute zero thus no electrical conductivity. However if the bandgap is sufficiently small there existed a finite probability for the electrons in the lower energy band to be thermally excited to the next allowed band at temperature above absolute zero, hence partial

electrical conductivity is permitted as in the case of semiconductors. As for insulators, the bandgap is so large that even at elevated temperature no electrons can be thermally excited over the forbidden gap.

Photoluminescence in bulk CdSe semiconductor begins by absorption of a photon with energy higher than the bandgap, this energy than excite an electron from the valance band to the conduction band leaving a hole in the valance band, the electron and hole pair subsequently recombines and release the excess energy by emitting another photon. The emitted photon can be stoke shifted to a lower energy (longer wavelength) compared to the absorbed photon for the same transition by coupling with the vibrational modes, therefore lose a bit of energy by phonon (heat) emission.

1.3.1 Quantum confinement

As the NC size shrinks and become smaller than or comparable to the characteristic length scale of the charge carriers, the allowed energy levels for these carriers will be quantised, analogues to the discrete energy levels of isolated atoms and hence NCs (and QDs) are sometimes referred to as artificial atoms. Such size dependence is name quantum size effect or quantum confinement where it can be divided into three categories. We first define the bohr radius of a carrier type particle (electron, hole and exciton) as,

$$a_{Bohr} = \varepsilon \frac{m_e}{m^*} a_0 \qquad (1.1)$$

where ε is the dielectric constant of the semiconductor, m_e is the electron rest mass, m^* is the mass of the carrier and a_0 is the Bohr radius of hydrogen atom. We will then consider three different Bohr radii, namely, a_e – for electron, a_h – for hole, and

a_{exc} – for exciton. The quantum confinement can then be described as *strong confinement regime* such that the nanocrystal radius, a_{NC}, is much smaller than a_e, a_h, and a_{exc}; or as *weak confinement regime* such that a_{NC} is larger than a_e and a_h, but smaller than a_{exc}; or finally as *intermediate confinement regime* such that a_{NC} is between a_e and a_h where one carrier is strongly confined and the other is not. At the strong confinement regime, the electron and hole can be treated as independent particles, hence the NC optical properties (e.g. photoluminescence) can be considered as the transitions between the electron and hole quantum-confined levels.

1.3.2 Quantum confined NC electronic structure

Early publications by Norris et al.[13, 14] have optically resolved the quantum-confined electronic states of NCs through Photoluminescence Excitation (PLE) and Fluorescence Line Narrowing (FLN) experiments. They proved experimentally the possible optical transitions between different electron and hole states calculated from a 8 band theory. The band edge luminescence (i.e. $1S_e \rightarrow 1S_{3/2}$) is the most commonly investigated transition in NC experiments and in practical applications. The first excited state fine structure reveals the existence of a "Dark" exciton. The transition from the lowest excited state ($J = \pm 2$) to the ground state is optically forbidden because it requires two units of angular momentum while photons only have one unit of angular momentum ($J = \pm 1$). Nevertheless transition is still possible via a low probability LO-phonon-assisted coupling that converses momentum. The importance of the Dark exciton is that at cryogenic temperature k_BT (~0.34meV at 4K) is reduced to a level smaller than the fine structure splitting (~1meV for a 5nm CdSe NC) between the lowest excited state (±2) and the first bright state ($\pm 1^L$). This results in the increase of radiative lifetime due to the small probability of thermal

excitation from the dark state back to the first bright state. The Dark exciton does not affect radiative lifetime at RT since k_BT (~25.7meV) is much larger then the energy splitting. A schematic for the CdSe NC energy levels is illustrated in Fig. 1.1

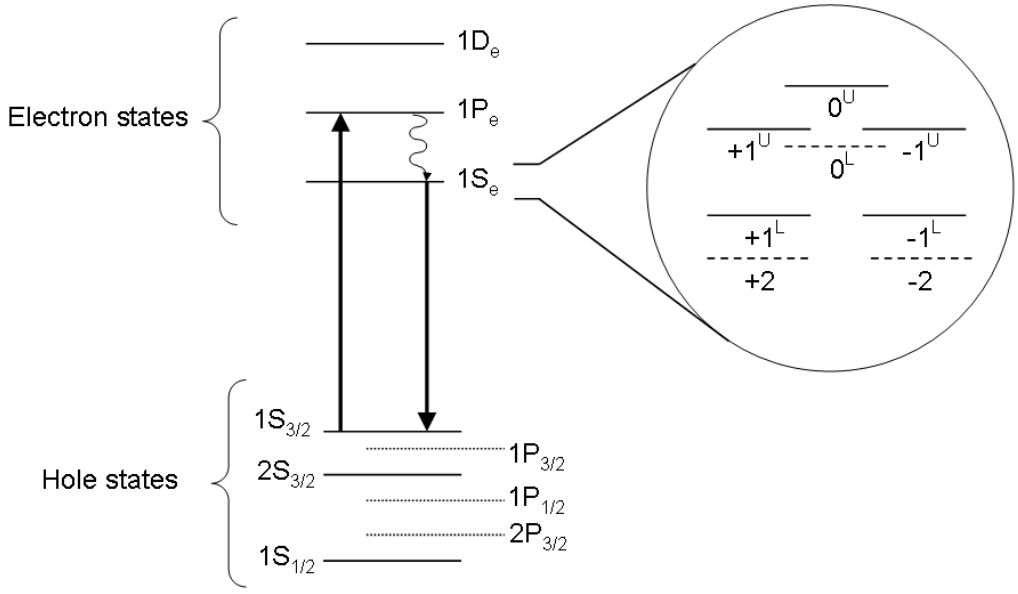

Fig. 1.1. Energy level diagram for CdSe NC (not in scale). S-type hole levels is represented by solid lines and P-type hole levels by dotted lines. Solid arrows represent the absorption and the radiative relaxation. Curved arrow is the fast non-radiative relaxation from higher excited state. Fine structure of the first excited sate is magnified inside the circle. Dashed line represent the optically dark levels

Chapter 2
Theoretical Models of Blinking

2.1 Single NC Blinking

In 1996, Nirmal et al. first observed fluorescence intermittency or blinking in a single CdSe NC[15]. Under continuous excitation, the single NCs exhibit a sequence of *on* and *off* periods that can last for tens of seconds. They suggested the fluorescence *on*- and *off*-states is related to a neutral or ionised NC respectively. Efros and Rosen took this further to propose a model for the observed blinking phenomenon[16]. In this model, a NC is ionised when one of the carriers is ejected to a surrounding acceptor level through a thermal or auger autoionisation process. Once the NC is ionised, further photon absorption results in a trion in the NCs core. The trion will relax through a nonradiative Auger recombination that is much faster then the radiative recombination[17-19], thus effectively quenches the NC luminescence. The NC stays off until subsequent neutralisation by the return of the ejected carrier or by capturing a different carrier of the same type as the ejected carrier. Electrostatic force microscopy confirmed that a photoionised single NC is positively charged and blinking can be related to the charged NC[20, 21]. Kuno et al. later recognised that the *on* and *off* blinking events follows a universal power law probability density[22]. This picture of a neutral and a charged NC is generally

accepted as the configuration leading to the *on*- and the *off*-state of NCs. What is unclear is the switching between the *on* and the *off* state, therefore what mechanism governs the ejection of the carrier that could lead to the power law statistics. Some possible carrier dynamics in fluorescence *on*- and *off*-state is illustrated in Fig. 2.1.

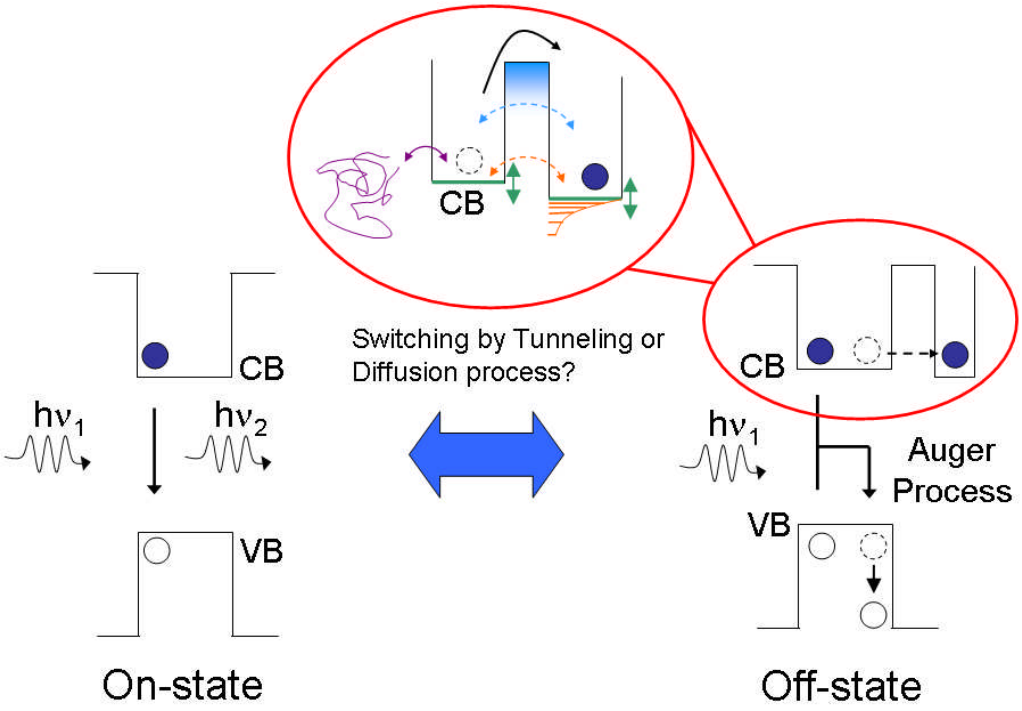

Fig. 2.1. Absorption of a photon in the *On*-state creates an electron-hole pair that subsequently recombines to emit another photon. The NC is *Off* when it is ionised, absorption of a photon creates an electron-hole pair that recombines nonradiatively, the excess energy is transferred to the lone carrier through an auger process. The charge carrier (shown as an electron but can also be the hole) may be ejected through different processes as illustrated by the diagram circled in red. (1) The electron can tunnel through the barrier to a static distribution of trap sites (orange dashed arrow). (2) The tunnelling barrier fluctuates (indicated by the blue gradient) as the electron tunnelled through the barrier, this results in a power law dynamic for both *on* and *off*-times (blue dashed arrow). (3) The electron may be ejected over the barrier through an auger assisted or thermal autoionisation process (black solid arrow). (4) The excited state and the trap state is diffusing in energy space, electron is transferred between the two states when they are in resonance (green solid line and arrow). (5) The ejected electron carries out a random walk in the surrounding and returns (purple solid arrow and line).

2.2 Theoretical Models for Blinking

Theoretical models aimed at explaining the power law blinking statistics could be broadly categorised in to two main groups, namely a tunnelling type or a diffusion

type model. A comprehensive reviews and discussions can be found in the literature[23-28], here we summarise the main aspects of the major theories.

2.2.1 Quantum jump

The fluorescence intermittency of a single NC resembles a random telegraph signal reminds us a historical quantum jump model first proposed by Bohr to explain a similar emission intensity fluctuation observed in an ion or atom. The quantum jump description refers to a non-emissive triplet state possessed by a molecule. Random jumps to this "dark" state result in a binary *on* and *off* emission intensity similar to what is observed in blinking intensity time trace. Nevertheless such a description will result in a single exponential *on*- and *off*-time probability density, in sharp contrast to the power law behaviours routinely found in blinking statistics.

2.2.2 Static distribution of traps model

An activated Arrhenius model was historically proposed to explain the inverse power law behaviour in the phosphorescence decay of amorphous semiconductors. This model assumes a static distribution of traps that varies exponentially in density $\rho(E_T)$ with trap depth, E_T, i.e. $\rho(E_T) \propto \exp(-\alpha E_T)$. The thermally activated detrapping from these trap sites result in a different exponential decay rate for each trap depth, $\gamma(E_T) \propto \exp(-E_T/kT)$. The exponentially distributed traps each with a different exponential detrapping rate lead to an *off*-time power law probability density of $P(\tau_{off}) \propto \tau^{-m}$ with $m = 1 + \alpha kT$, however, the *on*-time probability density is still a single exponential distribution. This is because there is only one associated transition rate for the electron to leave the NC at any particular instance, therefore the overall escape rate is a sum over all the individual rates, which is still an single exponential.

Moreover, the power law exponent *m* depends on *T* will predict a temperature dependent power law distribution, in sharp contrast to the experimental results that shows no change in *m* from 400K down to cryogenic temperature[22, 29].

Verberk et al. proposed an alternative static trap distribution model based on charge tunnelling. The electron wave function decays exponentially from the NC core into the ZnS shell and outside the NC, thus the charge tunnelling rate depends exponentially on the trap distance, *r*, from the NC core such that the trapping rate is $k_T \propto \exp(-\alpha r)$ and the detrapping rate is $k_D \propto \exp(-\beta r)$. The constants α and β relates to the tunnelling barrier height. For a static distribution of traps similar to the Arrhenius model, the off-time probability density turns out to be $P(\tau_{off}) \propto \tau^{-\mu}$ where $\mu = 1 + \alpha/\beta$. The merits of this model are (1) temperature insensitive power law dynamics is explained by the tunnelling process, and (2) it naturally explains the dependence of power law exponent on the surrounding dielectric material[30] through the different constants α and β. Nevertheless the model also fall shorts on two aspects, (1) still predicts an exponential *on*-time distribution, and (2) the NC wil spend most of its time in the ionized dark state because of the large tunnelling rates associated with the closest trap sites, in contrast to the long *on*-times observed experimentally.

2.2.3 Fluctuating barrier model / Dynamic traps model

Kuno et al. proposed a fluctuating barrier (in either width or height) model to account for both the *on*-time and *off*-time power law dynamics[23, 31]. They argue that a small fluctuation in the barrier would result in a large modulation to the tunnelling rate that leads to the power law dynamics. The barriers are postulated to change due fluctuation to the local environment around the NC.

Alternatively, Verberk et al. accounts for the long *on*-times by a dynamic traps model such that trapping can be switched off by making the traps inaccessible[32]. They proposed that after an ionisation event, Coulomb blockade will prevent further ionisation because it cost too much energy to extract another electron. However if the remaining hole now becomes delocalised and trapped in the shell, the NC core may radiate once more because the exciton wave function decreases exponentially into the shell thus reducing the nonradiative auger recombination rate. The NC will remain *on* until another electron that tunnels back from the traps annihilates the localised hole, hence the *on*-time distribution will behave like a power law similar to the *off*-time distribution.

2.2.4 Spectral diffusion model

Shimizu et al.[29] suggested the trap energy level might diffuse in a 1D energy space. Charge transfer will take place whenever the trap energy is in resonance with the excited state, thus switching the NC from *on* to *off* or from *off* to *on*. The 1D random walk immediately gives rise to the characteristic -1.5 power law exponent for both *on*- and *off*-times. Tang and Marcus[26, 27] further developed a Diffusion-Controlled Electron Transfer (DCET) model assuming both the excited state and the trap level are diffusing along a 1D reaction coordinate. Switching between *on* and *off* states occur at the crossing point of the two energy parabolas each represents the *on* and the *off* states respectively. The linkage between emission spectrum diffusion and blinking can be incorporated into the model by projecting the spectra diffusion alone another reaction coordinate. This model predicts three distinct time regimes for the power law dynamics, (1) at $t < t_c$, $m = -0.5$, (2) at $t_c < t < \Gamma$, $m = -1.5$, (3) at $t >> \Gamma$, the probability density shows an exponential roll-off. The parameter t_c is a critical

time for the power exponent to switch from -1.5 to -0.5 and its definition will depend on the different diffusing coordinates. Γ is defined as the power law saturation time. The exponential roll-off is observed experimentally for *on* times and its existence is postulated for *off* times but may be beyond experimental reach. The prediction of the power law exponent switching is distinctive for any 1D diffusion model with an absorption sink. Tang improved the DCET model to accommodate the deviation of the power law exponents from the nominal -1.5 by considering anomalous diffusion[33]. The power law exponent before t_c is then defined by $m = \mu/2$ and by $m = 2 - \mu/2$ after t_c, where $0 < \mu < 2$.

2.2.5 Spatial diffusion (random walk) model

Diffusion of an ejected carrier may take place in a three dimension space around the NC. Such spatial random walk model is suggested by Margolin et al.[34]. The time of first passage for a random walker to return to its starting point naturally predicts a -1.5 power law exponent. Common to any diffusion models, anomalous diffusion needs to be considered in order to account for the deviation from the -1.5 exponent. However according to Polya's theorem[35], there is a finite probability that the three dimension random walker will never return to its origin, therefore results in a permanently dark NC after few blinks, contrary to common experimental observation.

2.2.6 Diffusive non-radiative rate model

Frantsuzov and Marcus developed another diffusion model similar to DCET but with a different definition to the diffusing reaction coordinate. They proposed diffusing nonradiative rates that give rise to the -1.5 power law exponent. The fluctuation in

the nonradiative rate is attributed to deep surface states acting as hole traps, an Auger-assisted excitation from $1S_e$ to $1P_e$ electronic state results from the trapping of the $1S_{3/2}$ hole state to a deep surface state. Phonon-assisted relaxation of the electron in the second excited state back to the first excited state is then recombined non-radiatively with the trapped hole. The diffusion in energy of the $1P_e$ excited state effectively modulates the non-radiative recombination rate.

Chapter 3
Experimental methods

The key to investigate NC carrier dynamics lies in the ability to image and observe single NCs. This can be broken down into two main tasks, firstly, a method to prepare samples with bright NCs well separated from each other, and secondly, an optical microscope capable of gathering NC fluorescence signal while reducing unwanted background efficiently. With that facility in our pocket, we will want to measure the carrier dynamics in the widest possible time range. This is divided into three time regimes namely, slow-, mid- and fast-range. Each regime is analysed by measuring blinking statistics, autocorrelation function ($g^{(2)}$), and Time Resolved Photo-luminescence (TRPL) respectively. In this chapter, we will describe how we gather and process the raw data, leaving the analysis to subsequent chapters.

3.1 Sample preparation

The aim in sample preparation is a repeatable procedure to produce samples consisting of single NCs well separated from each other. Since the fluorescence intensity of a single emitter is limited, we want to keep the single NCs as bright as possible, or in other words, maintain a high quantum yield. On the other hand, using a substrate with minimum autofluorescence will ensure a low background level.

Combining the bright NCs with the low background will provide a high contrast in signal to background ratio.

The substrate we use is fused silica from UQG Optics (Spectrosil® 2000, fluorescence free grade) diced into 5mm (L) x 5mm (W) x 1mm (T) square plates. The fused silica substrate is further treated by heat for 5 minutes prior to use with a hot air gun capable of delivering up to 600^{o}C of airflow. This procedure is carried out to remove any residual organic substances remaining on the substrate to ensure the background level during measurement that comes from the auto-fluorescence of the substrate is at a minimum.

The NCs used in this project come from various sources, including commercially available Evidot (Evident technology), Qdot® (Invitrogen) and some custom made NCs from our collaborating partners, Prof. Paul O'Brien's group (University of Manchester), and Prof. Peter Dobson (University of Oxford). The structure of the NCs used include bare NCs (CdSe core only), core/shell NCs (CdSe/ZnS) and QDQW NCs (quantum dot quantum well), as illustrated in Fig. 3.1 below. These CdSe NCs are approximately 5 nm in diameter and its fluorescence emits in the orange-red region (approx. 580 nm to 620 nm) of the visible spectrum. The choice of the NC size and hence its emission wavelength is based on the effectiveness of a long pass filter to block out all blue laser (475 nm) excitation intensity and let through all the emission from the NC. The organic ligands surrounding the NCs are commonly TOPO, HDA, Oleic Acid or some long chain amine. They serve to passivate the NC surface and hence to improve the quantum yield of the fluorescence. These ligands also work to keep NCs separated from each other, to reduce agglomeration when NCs are in close contact.

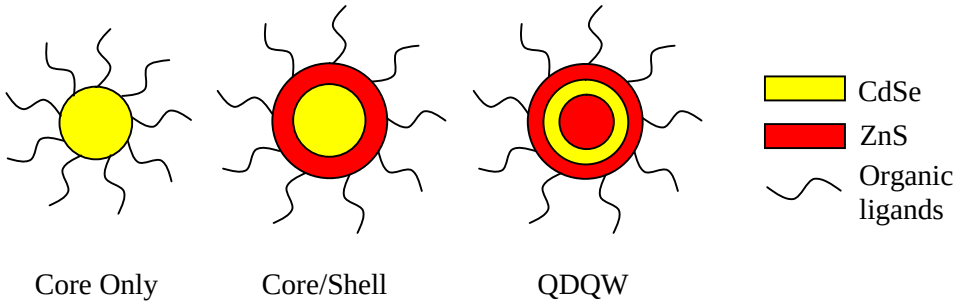

Fig. 3.1. Structure of NCs.

To make a sample containing identifiable single NCs we start from NCs dissolved in a solution then spin cast one drop of that solution onto a heat-treated substrate. One can observe single NCs well-separated from each other under an optical microscope if the solution is in a right concentration. If the solution is too concentrated it will be difficult to resolve single NCs, on the other hand if the solution is too dilute it will be challenging to locate a NC within the field of view. A diluted solution with concentration in the range of 0.2 nM to 0.4 nM works well for our setup. However, with such a diluted solution, the NCs tends to loose their brightness and they easily clot together to form a cluster. Ligands detached from the NCs surface could lead to both of these undesirable results. The way to overcome this issue is to ensure a sufficient level of ligand concentration in the solution throughout the dilution process; when there is a high concentration of ligands dissolved in the solution then it will be less energetically favourable for the bonded ligands to be detached from the NC surface. The excessive number of long chain ligands dissolved in the solution could entangle with the tail of a ligands bonded to the NC surface, such a process can further assist in the separation of NCs. In our experiments, HDA (hexadecylamine) is usually employed as the extra long chain ligand. In addition to the ligands, we usually include a polymer such as PMMA (poly(methyl methacrylate)) by dissolving it in the solution to allow for an evenly

distributed thin film of NC to be spin casted on to the substrate. The order to dilute a NC solution is as followed, firstly add ligands and PMMA into an empty vial, then pipette the NC solution to be diluted into the vial, and finally add solvents to dissolve and dilute the contents. For a 4 ml vial, a working recipe is to add about 50 mg (0.5 % wt) of HDA and PMMA each, then some amount of NC solution depending on the desired final concentration, finally add chloroform as the solvent and shake the vial for few minutes to promote a complete dissolution of all solids. This is a repeatable recipe to produce samples with about 10-30 single NCs in a ~20 μm diameter field of view.

3.2 Optical setup

In single molecule fluorescence studies, a high quality optical microscope is essential. We constructed a custom-made epifluorescence microscope from Thorlabs components as shown in Fig. 3.2 and a schematic in Fig. 3.3. The essence of an epifluorescence microscope is that it delivers the excitation and collects the emission with the same objective above (epi-) the sample. In this configuration, only a small portion of the excitation due to the reflection from sample surface is collected together with the weak fluorescent emission from the single emitter, this improves the signal to background ratio. The signal intensity can be enhanced by using objectives with higher numerical aperature (NA) given by

$$NA = n \sin\theta \qquad (3.1)$$

where n is the refractive index of medium between objective and sample, and θ is the half angle of the maximum collection cone of the objective. As one can see from Eq. 3.1, the enhancement is made possible through a larger collection cone, i.e. by

increasing θ, for an air objective (n = 1). One can also utilize an index matching medium such as oil (n =1.5) in an immersion lens to further improve the collection efficiency. We make use of two different objectives in our setup, one is a normal 60X objective (NA = 0.75) and the other is a 100X oil immersion lens (NA =1.25).

Underneath the objective is a sample stage mounted onto a differential micrometer controlled positioning unit. The XY-translator is capable with a coarse travel range up to 13 mm while maintaining a 25 μm/rev fine adjustment pitch, this property is desirable since it allows for a long scanning range that is advantageous when locating sample features; once an individual NCs is located, a precise submicron-level positioning is possible through the fine adjustment. The sample stage is interchangeable with a continuous flow cryostat if one needs to perform a temperature dependent experiment. Depending on the cryogen used, the cryostat can work from room temperature down to 4 K. At cryogenic temperatures, good heat insulation is important for temperature stability and efficient cryogen usage. In order to maintain the best heat insulation the local environment around the cold finger is always pumped down to a high vacuum state (~5×10^{-6} mbar) before the experiment. The cryostat can maintain a good vacuum level for several hours therefore the experiment can run without the vacuum pump pumping in the background. This is an essential feature for single NC experiments because the pump is a big vibration source that can introduce mechanical instability and make the experiment very difficult if not impossible. Due to the vacuum sealing requirement, an extra glass window is necessary above the cold finger and the sample, therefore a special objective lens with a correction ring is required to compensate for the extra spherical aberration introduced by the window. The objective lens we use is a Nikon Plan Fluor ELWD 60X (NA=0.7).

To the right of the objective is the excitation arm. It consists of a fibre coupled laser excitation, different laser sources (e.g. CW or pulsed; different wavelengths) can be adapted in to the system simply by coupling into the fibre. The fibre is collimated by a low magnification objective then passes through a laser clean up filter to remove any modes other than the designated main laser peak. Between the clean up band-pass filter and the collimator is a long focal length lens mounted on a flip mount, it provides a quick switching between broad illuminating area or a tightly focussed spot. A broad illumination provides a means to locate multiple NCs effectively while a tight focus can target a single NC without exciting any nearby elements therefore improving signal to background ratio. In the middle of the excitation arm is a beam splitter that reflects a small portion of the excitation to a small CCD camera, this allows for real-time monitoring of the laser spot and provides an approximate guide to place the objective near the exact focus on the sample surface.

Between the excitation arm and the objective is a 510 nm dichroic filter (Semrock), it reflects light of wavelength below 510 nm and transmits anything above it. Combining the dichroic and the 510 nm long-pass filter after it, the excitation laser is attenuated to a level much lower than the emitted fluorescence signal. The excitation arm, sample objective, dichroic and long-pass filter are all mounted on a platform supported by three rigid posts for added mechanical stability.

After the 510 nm long-pass filter is a set of lenses arranged telecentricly, where two identical doublets are placed two focal lengths apart from each other. Since both the object plane and image plane of the telecentric lenses are at infinity (collimated) so the system is called bi-telecentric. The telecentric lenses make sure all the incoming rays hits the centre of the eyepiece coupling into the spectrograph. A

pinhole can be placed in the middle of the telecentric lenses, where the focal points of both lenses coincide with each other to turn the microscope into a confocal system.

The emission signal is finally focussed by a 150 mm focal length doublet into the spectrograph (Princeton instruments – Acton SpectraPro 2500i) coupled with a high sensitivity liquid nitrogen cooled CCD camera (Spec-10 100B/LN). Inside the spectrograph a mirror and two gratings are installed on a triple grating turret. The mirror enables the system to work in image mode such that an emitting source can be identified, then moved to a specific pixel on the CCD with ease. Once the source of interest is in the centre of the CCD, the entrance slit of the spectrograph will be narrowed to cover only a few more pixels then the emitting source. The narrowed slit and software bracketing allows a single emitting source to be pinpointed. Once the emitter is isolated, we can measure its spectrum by changing the mirror to a grating. Two gratings with different resolutions are available in our spectrograph, one has 300 grooves/mm with a minimum FWHM wavelength resolution of 0.3 nm and the other one has 1200 grooves/mm providing a higher resolution of 0.07 nm. The side exit of the spectrograph allows one to redirect the emission signal to a single photon detector (PerkinElmer, SPCM-AQR-14-FC; PicoQuant, PDM series) instead of the CCD camera for even higher intensity detection sensitivity. The single photon detector route is the basis for measuring and recording intensity time trace of a blinking NC. Our single photon detectors have timing resolutions of 500 ps (Perkin Elmer) and 50 ps (PicoQuant) respectively.

We have different solid-state lasers that can be used as the excitation source. One is a 532 nm green laser and the other one is a 475 nm blue laser; the blue laser is the main excitation source used in our experiments. The blue laser from PicoQuant can work in continues wave (CW) mode or in pulsed mode. The minimum pulse

width is as short as 70 ps with repetition rate from 80 MHz to 31.25 kHz selectable from the build-in frequency divider. A slower repetition rate is possible through a pulse generator connected as an external trigger.

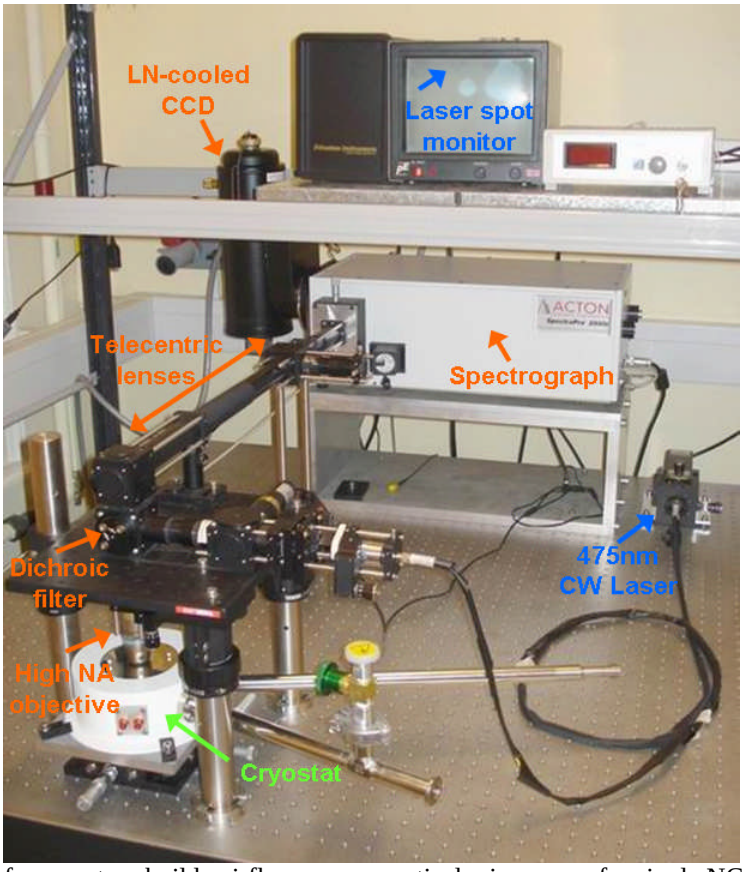

Fig. 3.2. Photo of our custom build epi-fluorescence optical microscope for single NCs studies.

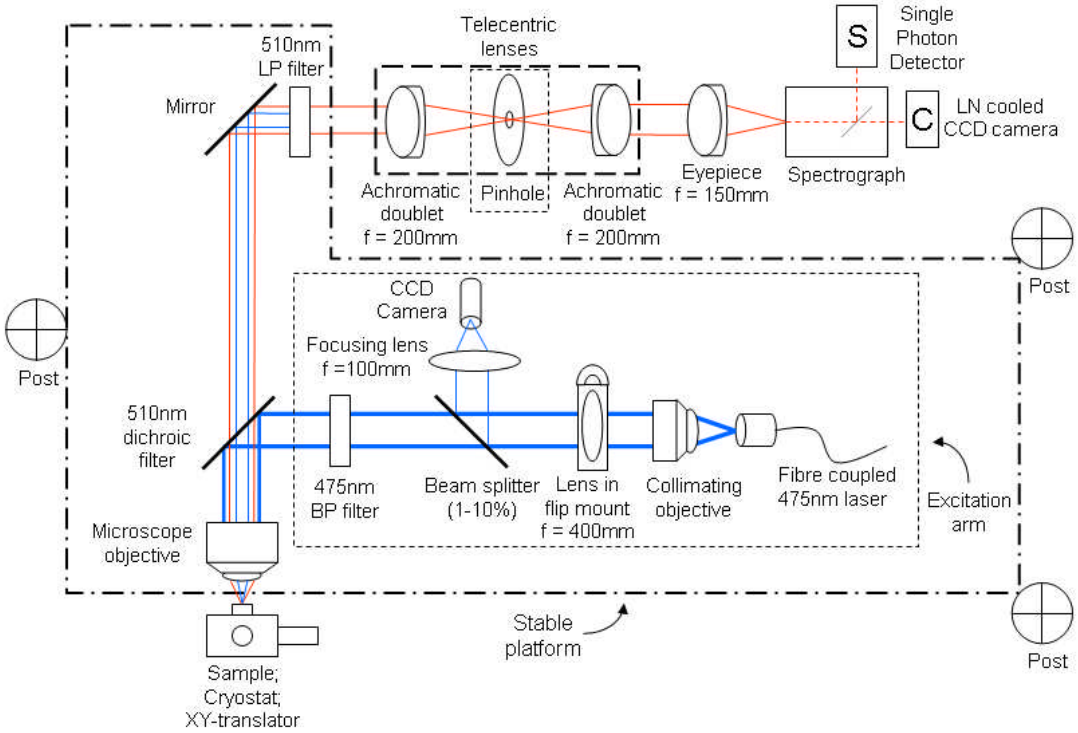

Fig. 3.3. Schematic of optical microscope setup.

3.3 Blinking statistics

Fluorescence intermittency, more commonly known as blinking, refers to the fluorescence of a single NC switching between an *on*- and *off*-state. The *on*-state is when the NC emits photons when excited and the *off*-state is when the NC does not emit photons even under a constant excitation. Using the microscope in image mode described in the previous section makes the switching event quite obvious as one would observe a bright pixel in the *on*-state and a dark pixel (the pixel has a same intensity as the background level) in the *off*-state. Observing blinking provides a simple method to identify single NCs since a cluster of NCs would not blink. However, several single NCs in close proximity exceeding the resolving power of the microscope, will appear as a single bright spot with fluctuating intensity analogous to a blinking single NC. This group of emitters will appear to be brighter then other single emitters if more than one of the NCs are simultaneously *on*. Recording multiple spectra of a bright spot over time provides a further evidence to differentiate a group of NCs from a single NC. Due to the inhomogeneity in the NC size distribution, different NCs will have a slightly different peak emission wavelength, therefore the spectra of a NC group will show multiple peaks while a single NC possess only a single peak. For an unambiguous proof of a single emitter, one can conduct a Hanbury Brown Twiss (HBT) experiment. Nevertheless, in general practice, by observing blinking events and recording spectra over time, one can be reasonably confident in identifying a single NC. Example images and spectra from different NCs are shown in Fig. 3.4.

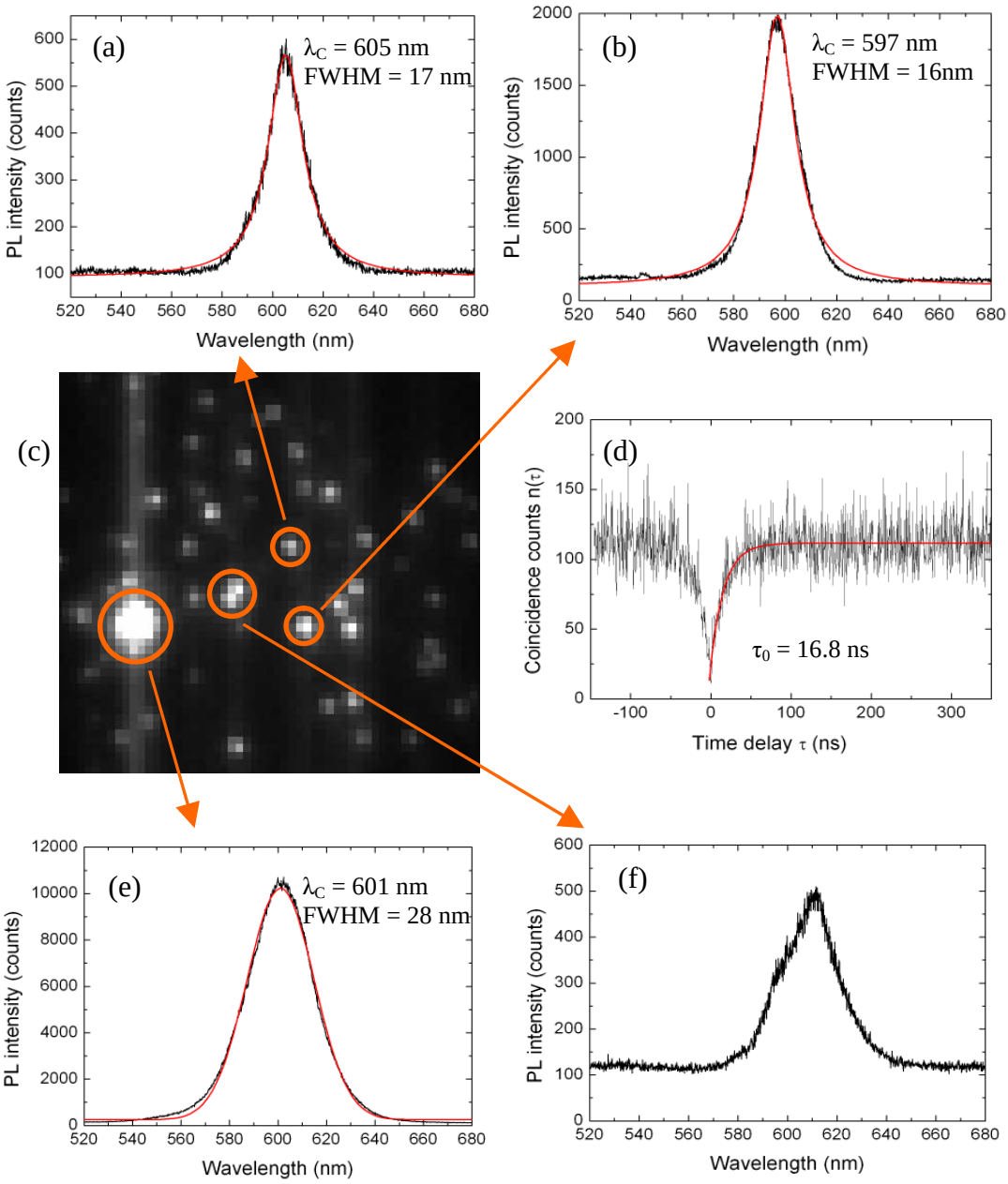

Fig. 3.4. Typical results from single NC measurements. (a) and (b) shows the spectrum of two separate single NCs indicated by the orange arrows from the image. The peak wavelength and FWHM indicated on the plot are obtained from the Lorentz fit (red solid line). (c) An image shows NCs within the field of view. (d) HBT data showing antibunching at zero time delay provideing unambiguous proof of a single NC. The solid red line is an exponential fit that gives a radiative lifetime of 16.8 ns. (e) Spectrum from a big bright cluster. Red solid line is a Gaussian fit that shows a much broader FWHM than the single NCs. (f) Spectrum of two NCs in close vicinity. The asymmetric shape suggested two NCs with two different wavelength peaks.

Once a single NC is located, recording its intensity time trace is done through a DAQ card (National instruments) that monitors the TTL output of the single photon detector. Whenever a photon arrives at the single photon detector a TTL pulse is generated, counting the number of TTL pulses within a fixed time bin over a period translates into the intensity time trace. The DAQ card makes use of an internal counter to count the number of TTL pulses, however, for high frequency counting it uses two counters where one is used to generate a reference pulse train with known period and the other one counts the source frequency in between the reference pulses. Despite the technical details behind data acquisition, controlling the DAQ card is straightforward as a result of a Labview software interface (Fig. 3.5) developed in-house. A few settings and some monitoring displays are available from the interface. Firstly, two timing parameters can be set at run time, which include a “Total measurement time” in units of seconds and an “Integration time” in units of milliseconds. The Integration time defines the minimum timing resolution of the intensity time trace. Using the DAQ card in the two counters mode, the fastest timing resolution of the whole system can go down to 5μs. Secondly, a real-time monitor of photons detected over time is displayed in a running chart and a digital counter gives the instantaneous photon counts per integration time. Finally, the completed time trace can be saved to any path defined by the user.

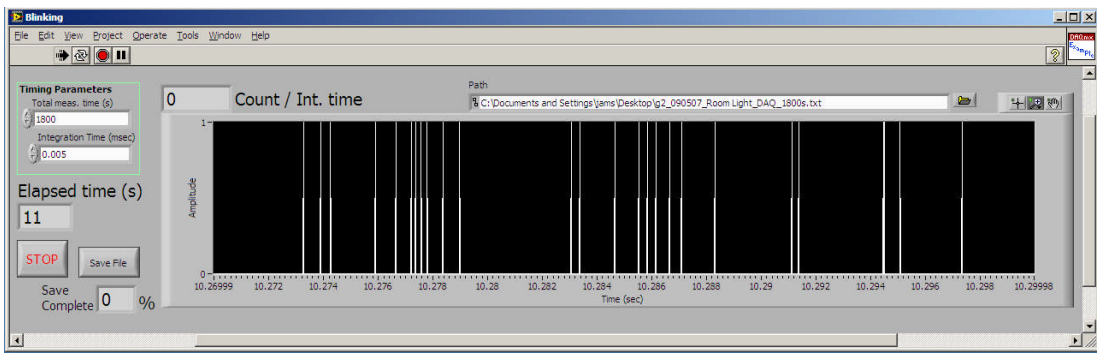

Fig. 3.5. Labview program interface for acquiring intensity-time trace data.

A typical intensity time trace is shown in Fig. 3.6. To the right of the trace is a frequency histogram of different intensities (photon counts). From this histogram, it is clear that the intensities are divided into two main peaks with counts of ~35 and 0 respectively. This signifies an *on* and *off* state but since the two states are not separated by two distinct binary levels, it is necessary to define an arbitrary threshold level to distinguish between the *on* and *off* states. A sensible choice of the threshold level would be at the valley between the two peaks. However, some NCs did not show a clear two peak frequency distribution as shown in Fig. 3.7, this makes it difficult to define a threshold in this manner. Therefore we define the threshold as three times the background APD level, the *on*- and *off*-time duration is subsequently defined as the time interval when the NC stays *on* or *off* before switching. This definition is applied to all NCs studied and is consistent with other research groups[36].

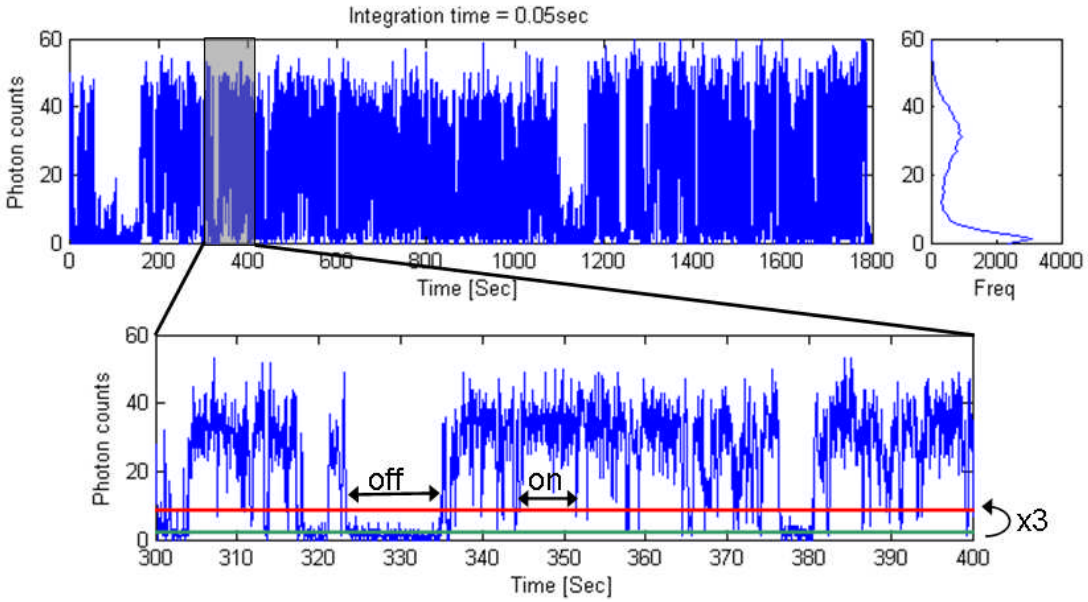

Fig. 3.6. A typical intensity time trace showing clear binary on/off events

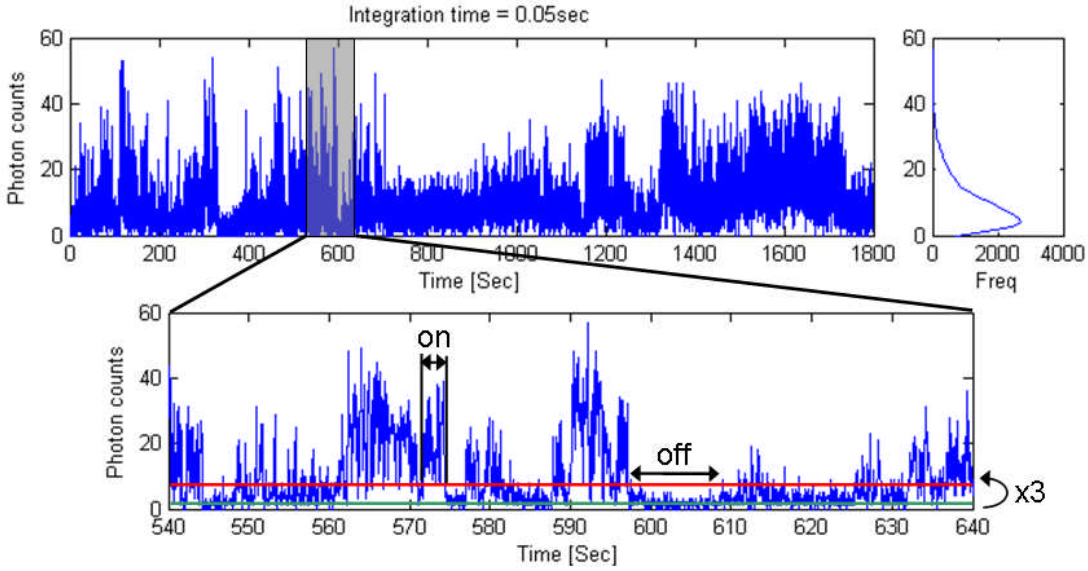

Fig. 3.7. An intensity time trace that does not show clear binary on-/off-state.

Since a threshold is necessary to separate the *on* and *off* states, the *on*-state needs to have sufficiently more photon counts in order to be distinguished from the *off*-state. Such a constraint sets a lower limit in the minimum integration time (or bin time). Depending on experimental setup, this limit usually lies in the regime of tens of milliseconds although some reports suggest it is possible to go down to 200 μs[22]. The limited integration time restricts the shortest on- or off-time intervals observable in blinking events. For example, with a 100 ms bin time, the photons detected has to be below (or above) the threshold level for at least 100 ms for it to be registered as an *off*- (or *on*-) event. The fixed bin time would also explain why sometimes a NC seems to emit only at a fraction of its maximum intensity, this is due to the NC switching between *on*- and *off-state* within a time interval faster then the minimum bin time resulting in a partially filled bin.

To analyze the statistical behaviour of blinking events, the general approach is to plot the frequency of *off*-time (or *on*-time) events against the off-time (or *on*-time) event duration. Similarly a probability density, $P(t_{off/on})$, can be plotted against the *off*-/*on*-time event duration ($t_{off/on}$) by means of a common definition of the probability density as

$$P(t_{off/on}) = \frac{N(t_{off/on})}{N_{off/on}^{Tot}} \times \frac{1}{\Delta t} \qquad (3.2)$$

where $N(t_{off/on})$ is the number of events of duration $t_{off/on}$, $N_{off/on}^{Tot}$ is the total number of *off* or *on* events and Δt is the minimum integration time. Such a definition will give all rare events that occur only once with the same probability and assign a zero probability to events that did not occur. However due to the finite acquisition time, long rare events will posses different statistics if the experiment is allowed to run infinitely long. In order to calculate a continuous probability density from the data

with finite experiment duration, we followed Kuno et al.[31] to introduce a weighting method in the estimation of most probable statistics in long rare events. This is done by replacing Δt in Eq. 3.2 by the average time between nearest neighbour events. For short events where the frequency of occurrence is high, this weighting has no effect since each neighbouring bin time has a frequency equal to or larger than one. This simply reduces the weighting back to the minimum bin time. On the other hand, for long events where the frequency of occurrence is low, the weighting reduces the probability density of that event by a factor according to neighbouring events. In other words, the weighting allows a frequency event smaller than one to occur within the limited acquisition time.

A Matlab program is create to import the intensity time trace in the form of an ascii text file. After the user sets a threshold level, the program will then automatically analyze the input file according to the methods described above. It will then plot the intensity time trace, frequency histogram of intensity counts and probability density against both *on*- and *off*-time durations in an organised interface shown in Fig. 3.8

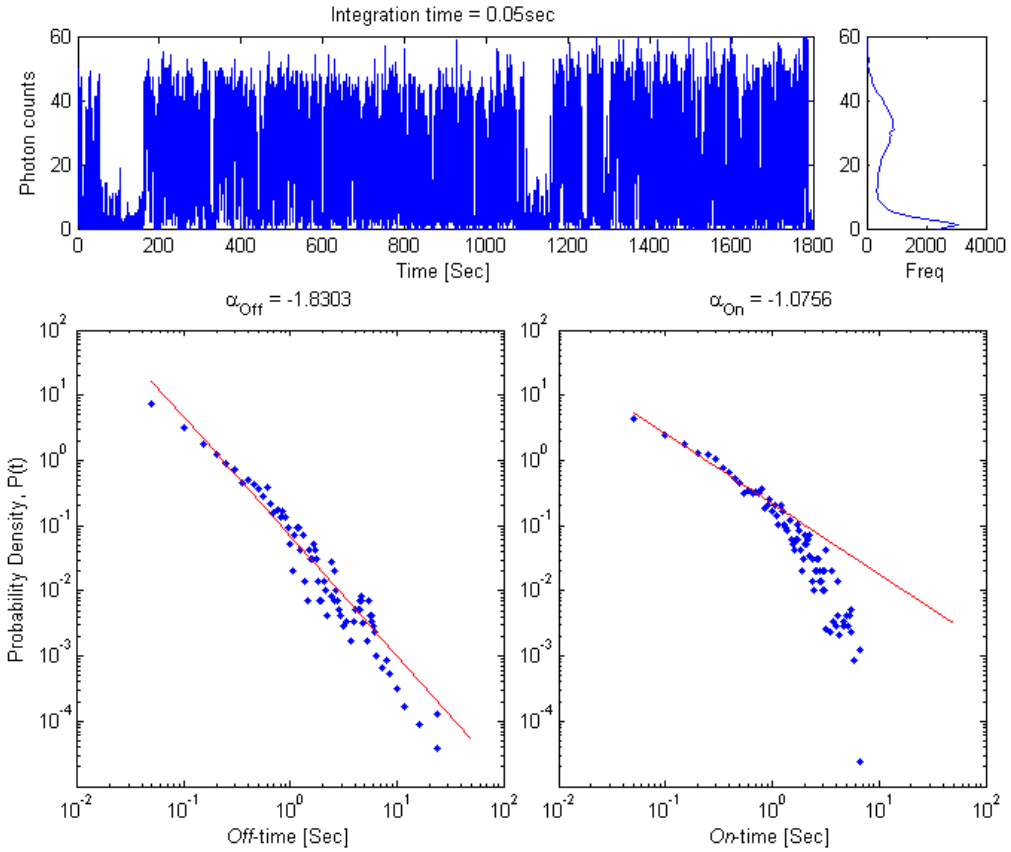

Fig. 3.8. Matlab graphical interface combining intensity time trace, frequency histogram of intensity counts, and probability density of on- and off-time events. Red line is a linear fit through the data points where its gradient gives the power law exponent α_{on} and α_{off} respectively.

From the log-log plot of the probability density against the duration of events, one can observe a linear relationship. This suggested a power-law dependence. Fitting a straight line through $\log[P(t_{off/on})]$ and $\log[t_{off/on}]$ gives a gradient that is equal to the power-law exponent, $-(1+\mu)$described by the following equation

$$P(t_{off/on}) = At_{off/on}^{-(1+\mu)} \qquad (3.3)$$

where A is a constant. The power-law coefficient μ is a common quantity used in the analysis and characterisation of NC blinking phenomenon and μ is universally found to be around 0.5. The *on* time events follow the same power-law dependence but usually has a different α compared to the *off* time events. Also the *on* time statitics tend to tail off from a pure power-law at longer time events[29].

3.4 Time-Resolved Photoluminescence (TRPL)

TRPL is a standard method to explore the carrier dynamics between two optically active states by means of the carrier decay rate between these two states. As an example, let us consider a simple two level system where the lower level is the ground state and the upper level is the excited state. When an electron is promoted from the ground state to the excited state by an incident photon, the electron will decay from the excited state and recombine with a hole in the ground state to release its excess energy by emitting a photon. Such a process regards the two states as optically active and the electron-hole pair is called an exciton. A certain time interval is required for the excited electron to decay from the excited state down to the ground state, this time interval is referred to as the exciton lifetime. The reciprocal of the lifetime is termed decay rate. In short, TRPL is a measurement of the excited state population decay rate. Let N be the excited state population, the decay rate of excited state population is proportional to N through a decay constant k, this can be represented by the differential equation

$$\frac{dN}{dt} = -kN \qquad (3.4)$$

and the solution is

$$N(t) = N_0 e^{-kt} \qquad (3.5)$$

where $N(t)$ is the population at time t and N_o is the initial population at time $t = 0$. This is an exponential decay with a decay rate of k or a lifetime of $\tau = 1/k$. If a radiative recombination is the only decay route between the two states then the measured lifetime represents the exciton radiative lifetime between the two states. If

there are other non-radative routes between the two states then the measured decay rate is a sum of the different decay constants.

To measure the exciton lifetime one could make use of TCSPC (Time-Correlated Single Photon Counting) hardware, such as the Edinburgh Instruments TCC900 computer plug-in card used in our setup. Then a pulsed laser excitation capable of delivering pulses with widths shorter than the expected lifetime to be measured is required. As an example, our PicoQuant laser is capable of delivering pulses as short as 70 ps. The output signal from the laser driver synchronised with the laser pulses is then connected to the START trigger of the TCSPC hardware in order to start an internal clock. At the same time, the TTL output of the single photon detector is connected to the STOP trigger of the TCSPC hardware, whenever a photon is detected the internal clock will be stopped. The time difference between the START trigger and the STOP trigger is the photon arrival time after the pulse excitation. To obtain the true statistics, one need to make sure that between two adjacent laser pulses there should only be at most one photon arriving. Subsequent photons arriving after the first photon will not be counted until the next excitation pulse, therefore it will skew the statistics towards shorter arrival times, such an effect is termed “pulse piled up”. To prevent this artifact the STOP frequency should be kept below 5 % of the START frequency. Typically data is acquired over ~10^6 excitation/decay cycles. Plotting the photon arrival times against their frequencies provides statistics for the decay process. The single exponential decay is characterised by a linear gradient in a log-linear plot. Fitting an exponential to the data points give a time constant for the lifetime of interest.

Typical data for single NC TRPL is shown in

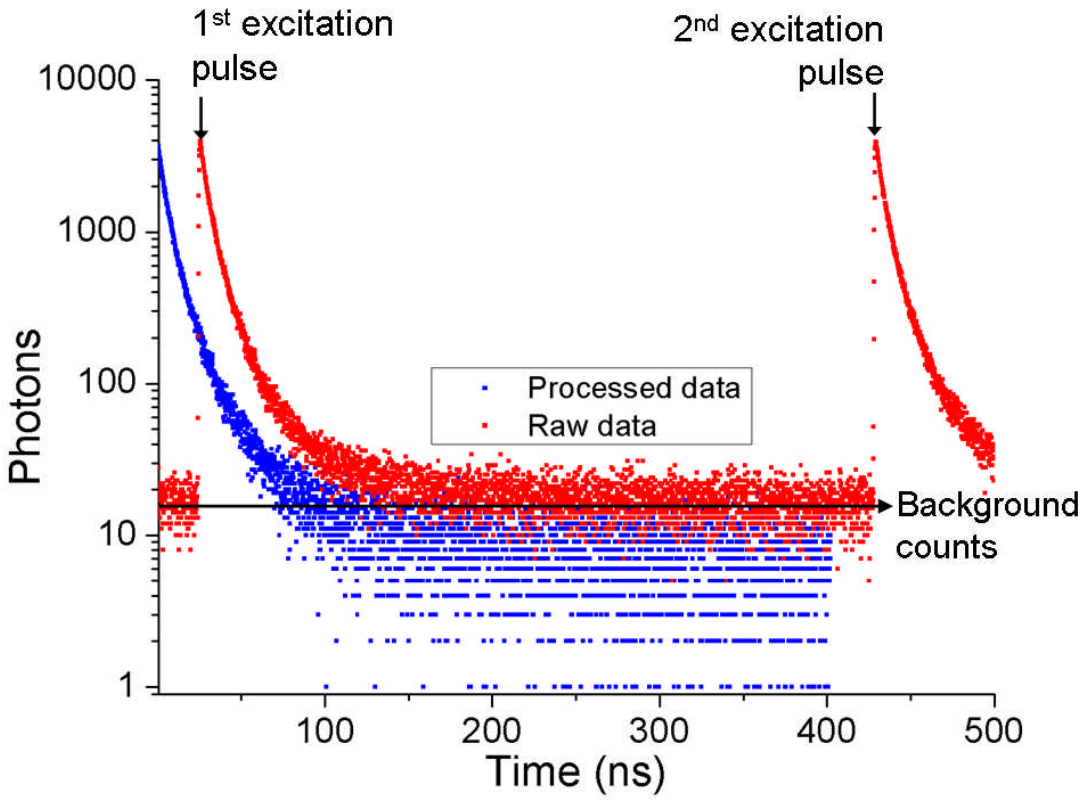

Fig. 3.9. The red dots represent unprocessed raw data. Useful data for exciton decay process is in between the two excitation pulses, therefore we remove data before the first excitation peak and after the second excitation peak then shift the entire curve towards left so that the peak of the decay corresponds to time zero second. Uncorrelated background photon counts can be identified if the tail of the decay curve comes to a clear flat background level, this figure is usually determined as the average counts just before the first excitation peak. Background counts are subtracted from the entire decay curve as an offset in the y-axis. The processed data is represented by blue dots in the figure. The curvature of the decay curve in a log-linear plot suggests a lifetime with a single exponential time constant is not sufficient to describe the decay process.

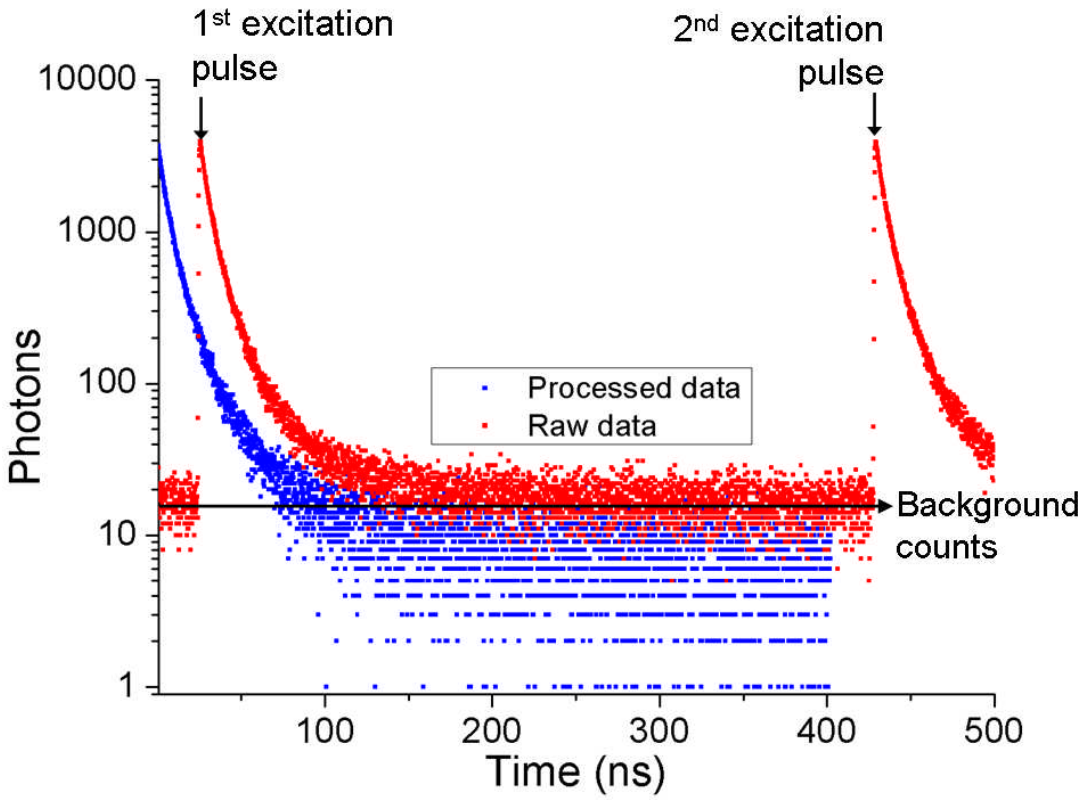

Fig. 3.9. Raw data for single NC TRPL.

3.5 Autocorrelation (g(2)) measurements

Autocorrelation is the cross-correlation of an intensity time trace with itself shifted by a time τ. An autocorrelation function monitors intensity fluctuation over a long period hence it is well suited for analyzing blinking statistics. The normalized autocorrelation function is defined as

$$g^{(2)}(\tau) = \frac{\langle I(t)I(t+\tau)\rangle}{\langle I(t)\rangle^2} \qquad (3.6)$$

where *I(t)* is the intensity (photon counts) at time *t* and *I(t+τ)* is the intensity shifted by a time τ. This definition expressed the autocorrelation function as the correlation between the intensity at time t_0 and the intensity at some later time. *I(t)* can be read directly from a single photon detector output without further processing that might

involve incorporating an arbitrary threshold. The absence of a threshold means that the $g^{(2)}(\tau)$ function is insensitive to detection yield. Furthermore, background noise only reduces the overall contrast of the autocorrelation function.

The intensity time trace needed for autocorrelation analysis can be obtained using a similar setup as for blinking statistics. However, without the required threshold, the timing resolution (bin size) goes right down to the equipment limit, which is 5 μs for the DAQ card.

At such small bin size, the intensity raw data is in the form of zeros and unit photon counts. The discrete intensities are measured at multiples of bin time, t_i, where the whole series is represented by $\{I(t_1), I(t_2), I(t_3),\ldots, I(t_N)\}$. The discrete-time autocorrelation function is calculated from the series using the following equations.

$$G^{(2)}(\tau_m) = \frac{1}{N-m}\sum_{i=1}^{N-m} I(t_i)I(t_{i+m}) \qquad (3.7)$$

$$\langle I(t)\rangle^2 = \left(\frac{1}{N}\sum_{i=1}^{N} I(t_i)\right)^2 \qquad (3.8)$$

$$g^{(2)}(\tau) = \frac{G^{(2)}(\tau)}{\langle I(t)\rangle^2} \qquad (3.9)$$

A different hardware setup to obtain the discrete-time intensity series is to make use of the TCSPC card in time-tagging mode. This arrangement is advantageous because the minimum timing resolution decreases down to 25 ns. However, the data format recorded by the TCSPC card is slightly different from that recorded by the DAQ card. Explicitly, instead of discrete intensities recorded at each multiple of bin time, each arriving photons is recorded by means of a running global

time. Therefore the series becomes $\{t_1, t_2, t_3, t_4,\ldots, t_N\}$ where t_i is the global arrival time of *i*th photon and t_N equals to the total acquisition time. This method of recording greatly reduces the raw data file size especially for a small bin size by dropping the massive number of zeros in the series.

However processing such series to obtain the autocorrelation function will require a slightly different algorithm. Namely each pair of the difference in time, $t_m - t_n$, will provide a frequency count of one at time $\tau = t_m - t_n$. Fig. 3.10 illustrates the process of building up the frequency histogram from the time difference pairs. Under such algorithm, it is necessary to calculate the whole set of time difference pairs before the frequency counts can be converted to $G^{(2)}(\tau)$ because the photon arrival time is randomly distributed. The conversion is done through an averaging factor 1/(N-m) similar to Eq. 3.7, where m = integers from 1 to N-1 corresponding to $\tau_1, \tau_2,\ldots,\tau_{N-1}$.

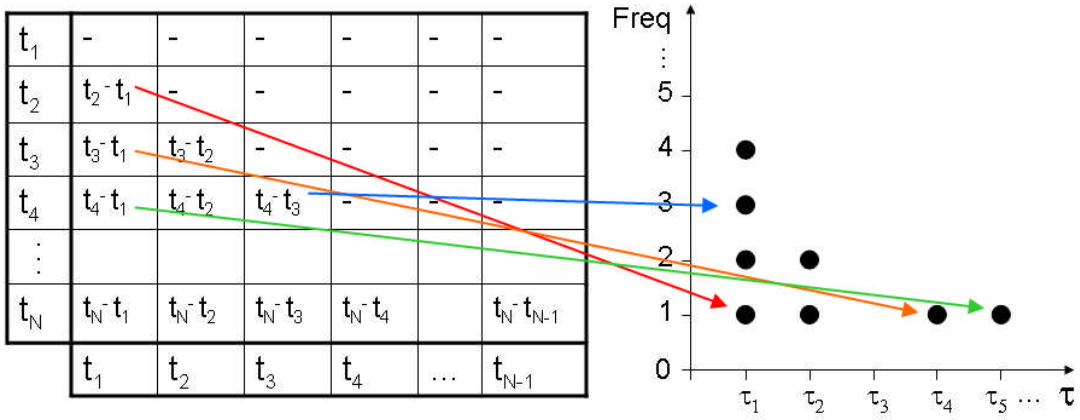

Fig. 3.10. A Process of building up frequency histogram from time difference pairs.

The computation time for both methods can vary in different scenarios as we can see from the following simplified order of complexity analysis. As one can see from Eq. 3.7, for the "multiply intensity method", the number of calculations scales as "number of elements in series", N_{MI}. Since we can calculate each $G^{(2)}(\tau_m)$ value independently, and typically we calculat 1000 values that spread logarithmically over

the entire time range, therefore the order of complexity scales as ~$1000N_{MI}$. For an acquisition time of 1800 sec with 5 μs time bin, $N_{MI} = 3.6 \times 10^8$. On the other hand, the order of complexity for the time difference method scales as $½N_{TD}^2$ as one can see from Fig. 3.10. N_{TD} increases as the acquisition time or average photon count rate increases but is less affected with smaller bin size. Typically in our experiments, N_{TD} ~10^5 within an acquisition time of 1800 sec. Therefore under these scenarios, the time difference method is faster than the multiply intensity method (the order of complexity for the time difference method ~10^{10} compared to ~10^{11} for the multiply intensity method). The advantages of the time difference method is firstly, as noted, its invariant calculation time with smaller bin size. Secondly it's less memory hungry during the calculation process and finally it is generally faster in most scenarios.

One problem with the autocorrelation analysis is the afterpulse artifact of a single photon defector, which means there is a small probability of a second artificial pulse being generated at a certain time after the first detection event. This is due to electrons being captured by defect sites in the SPAD when current flows through the device during a previous avalanche event, the trapped electron is then released at a later time causing a "false" avalanche breakdown. The afterpulsing will produce an artificial peak towards the shorter τ time delays. This is illustrated in Fig. 3.11 (red line) where a peak is clearly identified in the autocorrelation function of uncorrelated light. Usually this effect is countered by using a beam splitter that directs the signal into two single photon detectors, the autocorrelation function is then calculated as the crosscorrelation between the two detectors. However, this effect is not too critical for us since our minimum delay time is 5 μs, by which time the afterpulsing effect has flattened out.

One final remark on the practical issues in gathering intensity-time trace data

for autocorrelation analysis is mechanical vibration sources. Any vibration within the optical detection path could in principle affect the instantaneous optical intensity, such fluctuation in intensity will appear as a peak in the autocorrelation curve with a characteristic lag time equal to the inverse of the vibration frequency. If multiple vibration sources each with a difference frequency existed then the combined effect can introduce an artificial gradient into the autocorrelation curve. Some possible vibration sources include the motor for the grating turret in the spectrograph or strong cooling fans in a nearby controller that can have a physical contact with the SPAD through the rack framing. The blue line in Fig. 3.11 illustrates this artifact where an extra shoulder appeared between 10μs and 300μs.

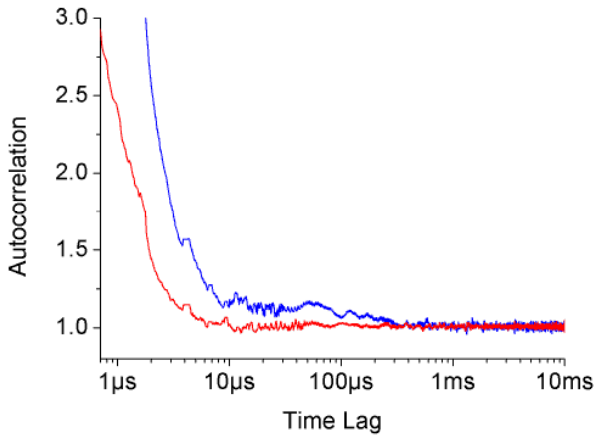

Fig. 3.11. (Red line) Autocorrelation function calculated from an intensity time trace of uncorrelated sunlight. (Blue line) Autocorrelation function of uncorrelated sunlight affected by vibration source nearby.

Chapter 4
Single NC Analysis I – TRPL and Blinking

The power law behaviour observed in blinking statistics originated from the carrier dynamics in a single NC. It is widely accepted that the *on* and *off*-state is related to a neutral or charged NC respectively. The ejected charge carrier may undergo a tunnelling or a diffusion process that leads to a power law dynamics. The tunnelling model[23, 31, 32] predicts a constant power law over all time regimes whereas the diffusion model[26, 27, 29, 33, 34, 37, 38] predicts a change in power law at some critical time t_c. Depending on the experimental setup, blinking statistics are routinely measured at time scales longer than tens of milliseconds[15, 29, 30, 36, 39-44] although faster measurements down to milliseconds or even sub-millisecond have been reported[22, 31]. Nevertheless, a limit is imposed by the threshold level that is required to distinguish between an *on*- and an *off*-event. Our approach to study the carrier dynamics is to measure the power law statistics over the widest possible time range. A Time-Resolved Photoluminescence (TRPL) experiment probes the population decay of an excited state with timing resolution of picoseconds to nanoseconds depending on the pulse width of a laser and timing jitter of the detector. With the 500 ps timing jitter of our Perkin Elmer SPAD as the limiting resolution, we are able to measure TRPL decay from nanoseconds up to tens of microseconds. Realizing the multi-exponential characteristic of a typical single NC TRPL decay

actually has a power law appearance suggests that it may be linked to the power law dynamics observed in blinking statistics at a much longer time regime. In this chapter we will describe how we can extract the power law exponent from the tail of the TRPL and link it to the blinking statistics whereby extending the ability to measure power law dynamics down to nanoseconds time regime.

4.1 Non-exponential decays of single NC TRPL

The common Markovian treatment of the radiative decay of an electronic two level system utilises Fermi's Golden Rule[45], an approximation derived using first order perturbation theory, to calculate a time independent transition rate which in turn leads to a distribution of photon emission times that follows a single exponential decay function. Such fluorescence decays are a feature of many simple quantum systems including atoms, dye molecules, and some semiconductor quantum dots. The inclusion of more complex recombination routes, such as those involving temporary shelving into a non radiative ‘dark’ state, may result in two or more terms in the fluorescence decay function, but nonetheless a Markovian treatment of each quantum transition dictates that each term will take an exponential form. It is therefore common practice to analyse non-exponential decays from quasi-isolated emitters such as semiconductor NCs in terms of either multiple or stretched exponential (Kohlrausch) functions[46-48], even when a detailed description of the energy levels that may cause such behaviour is missing. However, by re-plotting the multiexponential TRPL decay on a fully logarithmic scale as shown in Fig. 4.1, we observed the “curvature” of the multiexponential decay on the log-linear plot is actually linear on the log-log plot suggesting a power law relationship. Surprisingly

the gradient, α, of the linear component has a value common to what is found in blinking statistics, i.e. $1 < \alpha < 2$. This led us to believe the multiexponential or power law nature of the TRPL decay tail has the same origin as the blinking statistics.

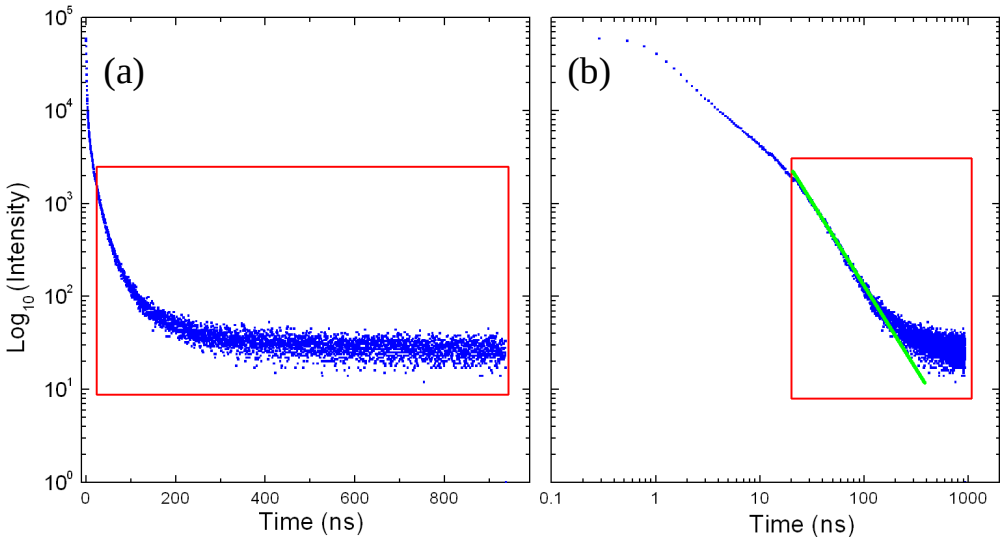

Fig. 4.1. Re-plotting the single NC multiexponential TRPL decay curve as seen on a log-linear axis (a) on to a log-log axis (b). Green line highlights a linear component at the tail (red box) of the TRPL.

The TRPL decay shown in Fig. 4.1(b) fades into the background as indicated by the flat region near the end of the decay. This background can be corrected through a control experiment by means of acquiring the TRPL data from a sample area where the is no NC present, if the acquisition time is fixed the intensity counts from the control experiment represents the true background induced by the system. The background corrected TRPL decay for the data shown in Fig. 4.1 is illustrated in Fig. 4.2. The tail of the background corrected TRPL decay represents the true power law gradient. In practice, if the tail of the TRPL goes into a clear flat level then it is safe to work out the background contribution from the average counts at the very end of the decay. However if the very end of the decay appears to have a gradient then one should acquire the TRPL with a larger TAC window so the flat background level is apparent or the background needs to be corrected through a control experiment.

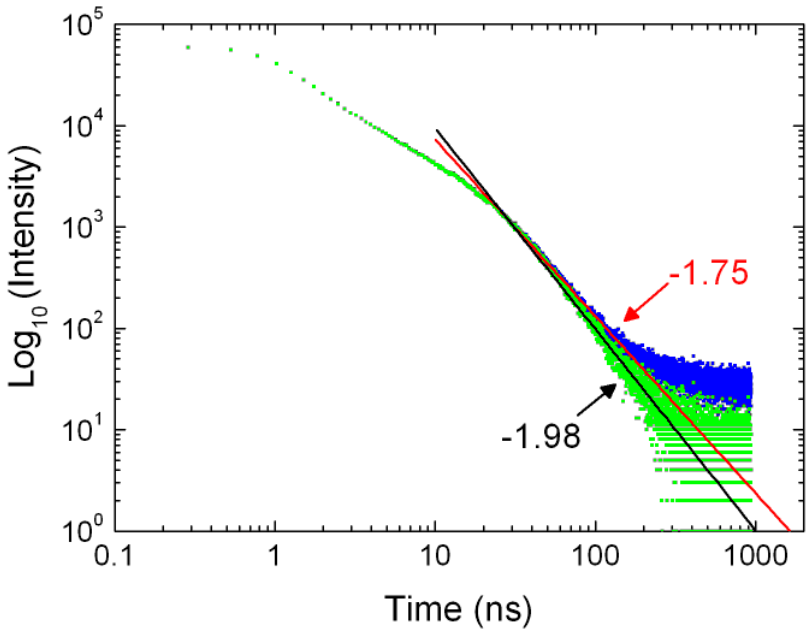

Fig. 4.2. Original (blue dots) and background corrected (green dots) single NC TRPL decay curve. Red and black solid line is an apparent linear fit to the tail of the original and background corrected TRPL respectively. The gradient of the fits is indicated on the plot.

4.2 TRPL data of single NCs and ensembles

Fluorescence blinking behavior of single semiconductor nanocrystals is found to follow power law dynamics. The probability density of measuring a period of duration τ for both the fluorescence *on* and *off* periods have been shown to follow a power law distributions given by,

$$P(\tau) = A\tau^{-(1+\mu)} \qquad (4.1)$$

where A is a proportionality constant and μ is the time independent power law coefficient.

To probe the relationship between the TRPL decay power law and the blinking power law statistics, we measured room temperature TRPL of three different nanocrystal types: bare CdSe nanocrystals (sample A), CdSe/ZnS core-shell structures (sample B), and $Zn_{0.5}Cd_{0.5}S$/CdSe/ZnS quantum dot quantum well (QDQW) structures (sample C). The core shells were fabricated by standard methods;

the bare nanocrystals (X. Chen, University of Oxford)[49], and the QDQW structures (S. M. Daniels, University of Manchester)[50] is fabricated by our collaborators. All of the samples showed strong ensemble luminescence at around 600 nm with no deep trap luminescence[12] as indicated in Fig. 4.3, but more importantly were not optimized for high quantum yield so that long fluorescence on times were absent.

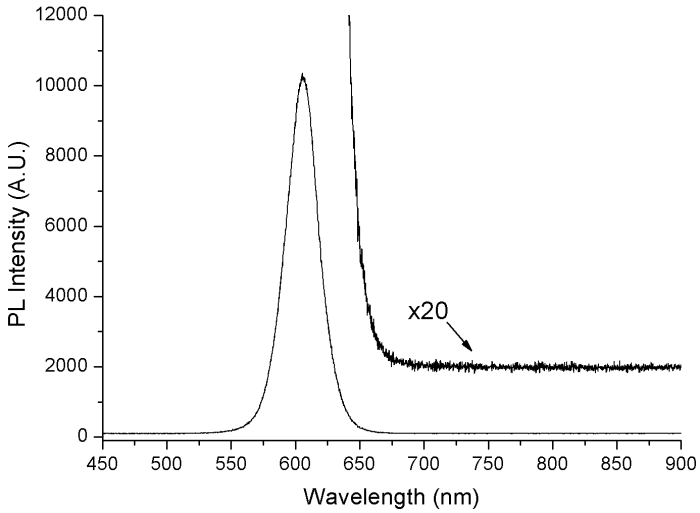

Fig. 4.3. A typical ensemble spectrum showing strong band-edge luminescence at around 600 nm. Absence of the deep trap luminescence is supported by the lack of broad band emission to the red of the band-edge luminescence (magnified by ×20).

Fig. 4.4 shows the fluorescence decay data for three single nanocrystals and an ensemble of each of the sample types A, B, and C. The same data (black squares) are displayed on semi-logarithmic axis in the left hand column and fully logarithmic axes in the right hand column of the figure. Power law behaviour appears as a straight line of gradient $-(\mu+1)$ on the fully logarithmic axes. Previously, single nanocrystal fluorescence decays have been fitted with biexponential functions with lifetimes of about 1 and 15 ns, attributed to Auger and radiative recombination processes, respectively[19]. Fitting biexponential functions to our data (solid red lines in Fig. 4.4) reveals excellent agreement up to about 50 ns after the excitation

pulse, but for longer delays, the fluorescence consistently decays more slowly than the biexponential function.

To fit the slowly decaying tails in our single nanocrystal data using exponential decays requires two further terms of lifetimes ≈ 70 ns and ≈ 200 ns. For the ensemble data, in which the higher intensity fluorescence allows us to measure their decay to a delay of 10 μs, four further exponential terms are required with a longest lifetime of ≈ 3 μs. Such ad-hoc introduction of further exponential decay terms to the fitting function is unsatisfactory, not least because each additional term requires two independent fitting parameters.

The presence of this slow tail indicates that between excitation and emission, the photogenerated exciton can enter a “dark” state from which it cannot radiate. We do not believe this state to be the dark spin configuration of the confined exciton ground state since the lowest energy “bright” exciton states for nanocrystals of this size (~5 nm) lie less than 1 meV (<< kT, 26 meV at RT) higher in energy[14] and the spin relaxation time is fast compared with the radiative lifetime[51, 52]. We also note the paper by Rothe et al reporting power law decay characteristics in a number of dissolved organic materials[53]. They analyze their data in terms of a first principles theoretical treatment of quantum transitions[54] in which power law decay at long delay times results from the fact that the radiatively broadened Lorentzian line shape is limited in extent to positive values of energy - a physical constraint that is neglected by Fermi's Golden Rule. However this effect appears far too weak to describe our data. Applying appropriate parameters for our material to equations 6.6 - 6.9 of reference[54] reveal that the onset of power law behaviour due to this mechanism is not expected to occur until the luminescence intensity has decayed to 10^{-19} of its peak value. In short, homogeneous broadening at room temperature is

dominated by rapid dephasing of the exciton and not by population decay. We propose that the power law behaviour observed in our TRPL data has the same origin as that observed in PL blinking measurements. In the relatively poorly passivated nanocrystals studied here, carrier escape into a surrounding trap state competes with the radiative recombination process, and so a few nanoseconds after photoexcitation, the nanocrystal is likely to be found in the charged fluorescence off state. Only when the ejected carrier, or another similar carrier, is captured back into the nanocrystal can radiative recombination occur, and so the fluorescence decay function reflects the distribution of time durations that the nanocrystal is in the fluorescence off state.

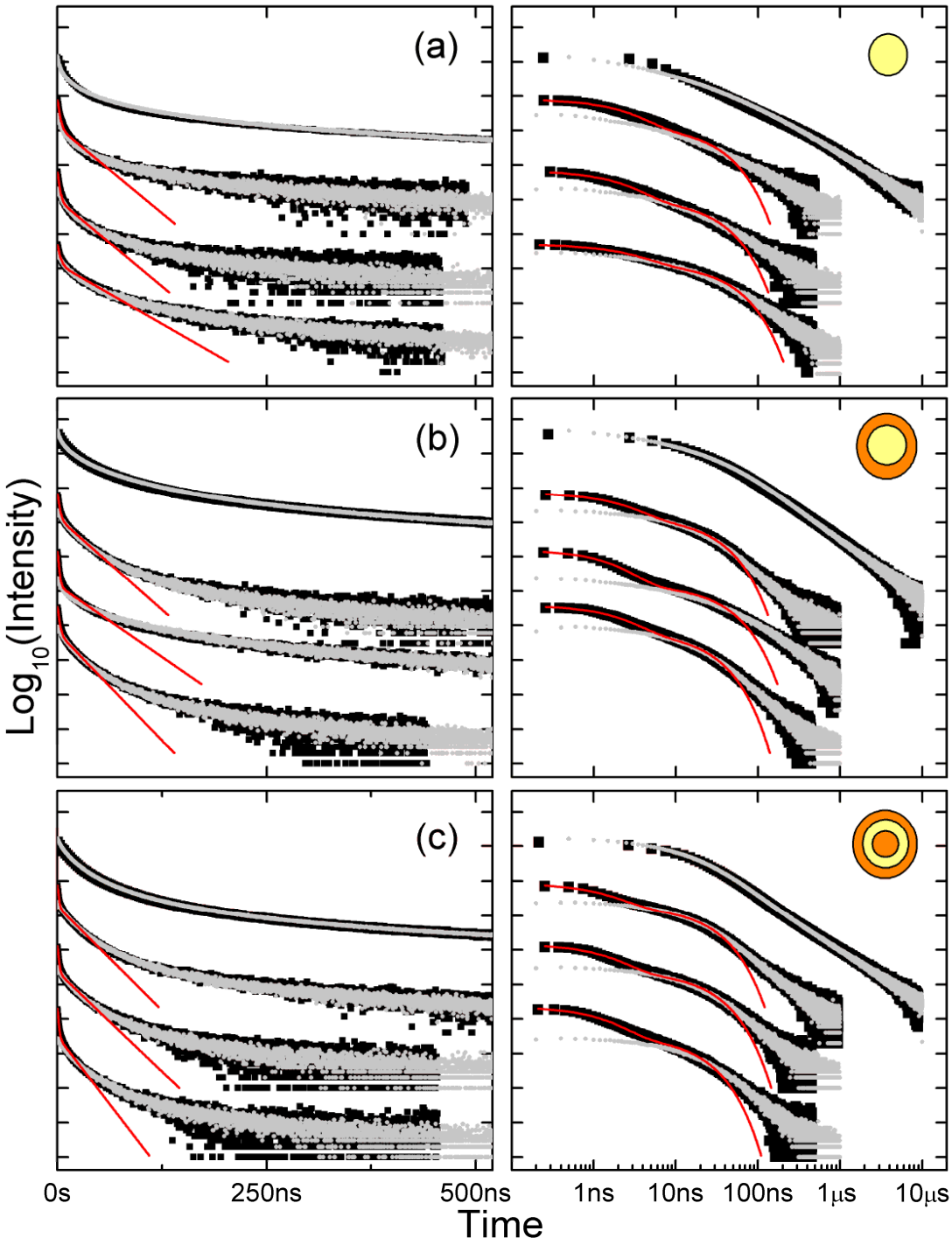

Fig. 4.4. TRPL data from semiconductor nanocrystals on semi-logarithmic (left column) and logarithmic (right column) axes. The three rows correspond to the different nanocrystal structures: (a) bare CdSe (sample A), (b) core shell (sample B), and (c) QDQW structure (sample C). All data sets are from single nanocrystals except for the uppermost one in each window, which is from an ensemble. The black scatter plots are raw data, the gray scatter plots are results of our MC simulation, and the solid red lines are analytical biexponential fits. In all cases, t = 0 corresponds to the peak of the TRPL signal.

4.3 Monte Carlo (MC) simulation

To model the fluorescence decay data we use the three level system shown schematically in Fig. 4.5 and a Monte Carlo method to generate simulated data sets.

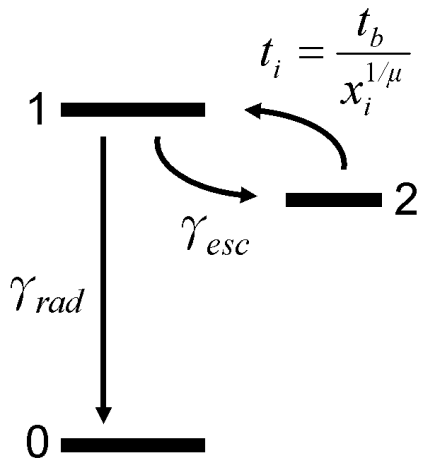

Fig. 4.5. Three level system used to simulate the tails of the TRPL data

Level 0 represents the nanocrystal in the ground state, level 1 represents the lowest energy state of the confined exciton - the fluorescence *on* state - and level 2 represents the fluorescence *off* state in which one of the photoexcited carriers occupies an external trap state. The radiative recombination rate is represented by γ_{rad}. When the system enters the *off* state 2, the time that passes before it re-enters the *on* state, t_i, follows a power law distribution generated using the function

$$t_i = t_b x_i^{-1/\mu} \qquad (4.2)$$

where x_i is a random variable in the range $0 < x_i < 1$, and t_b is the minimum measurable trapping duration[55], which in our experiment is equal to t_{res}, the timing jitter of our single photon detector (≈ 500 ps). At this stage we simply assume that t_i follows a power law distribution without implying any physical nature of state 2 (e.g. energy level relative to state 1) that may result in the power law distribution. It is

natural that the value of μ in Eq. 4.2 is compared to the blinking *off* power law coefficient, μ_{off}, since $P(t_{off})$ gives the probability density of time, t_{off}, for the NC in the *off*-state. To confirm Eq. 4.2 is sampling the power law distribution defined by Eq. 4.1, a frequency plot of t_i generated using 10^9 random numbers is shown in Fig. 4.6; the power law probability distribution calculated from the analytical expression is drawn on the same plot (red line). For both cases μ is set to 0.5 which translates to a power law gradient of -1.5. The randomly generated sampling of the power distribution coincides exactly with the analytical calculation proved the robustness of Eq. 4.2.

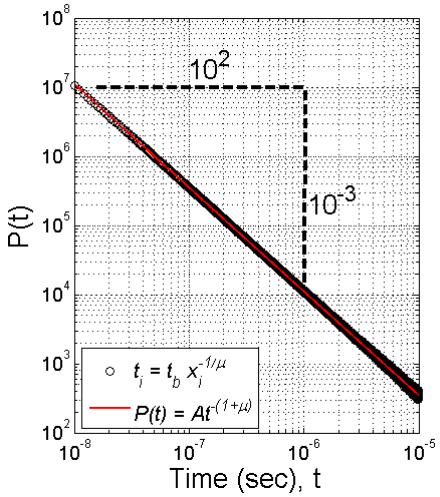

Fig. 4.6. A plot to justify Eq. 4.2 is randomly sampling a time, t_i, from the power law distribution defined by Eq.4.1. Frequency of t_i is generated from 10^9 random numbers, x_i, then binned linearly on the time axes with a bin size of 1 ns. Both the random sampling and the analytical calculation is generated using $\mu = 0.5$.

Despite the fact that *on* blinking statistics have also been shown to follow power law statistics, it is not trivial to represent γ_{esc} by a power law distribution in Monte Carlo simulation. However our samples are not well passivated so long *on* times are absent, therefore the carrier escape rate is fast compared to the radiative recombination rate hence it can be approximated by a single exponential at the time regime of interest in TRPL experiments.

For each MC iteration, the system is initialized in the exciton state at time t =

0 and is allowed to evolve until it undergoes radiative recombination to the ground state. The evolution times over many iterations are then plotted as a histogram. This provides a close analogy to the TCSPC data, which is a histogram of delay times between the excitation pulse and a single photon detection event.

Our simulation therefore contains just three fitting parameters (γ_{rad}, γ_{esc}, and μ_{off}). The interdependence of these fitting parameters is low: on the log-log plot γ_{rad} determines the delay time at which the 'shoulder' of the curve occurs; γ_{esc} determines the relative intensities of the exponential and power law components; and μ_{off} determines the gradient of the decay at long delay times. Clearly in the limit that $\gamma_{esc} << \gamma_{rad}$ the system will relax radiatively and the fluorescence decay will be exponential. For $\gamma_{esc} \approx \gamma_{rad}$ there is a non-negligible probability that the system will enter the trap state at least once before relaxing to level 0, whereupon a large number of excitation/relaxation cycles will yield a distribution of emission times with a significant power law component. In the extreme case where $\gamma_{esc} >> \gamma_{rad}$, the system will enter the off state on average $N = \gamma_{esc} / \gamma_{rad}$ times before emitting a photon and relaxing to level 0, and the total time spent in the trap state, $T_N = \sum_{i=1}^{N} t_{2i}$, is a *Lévy sum*, resulting from the fact that the mean value of the random variable t_2 is formally infinite, and is given by $T_N = t_b N^{1/\mu} L(\xi)$. Here $L(\xi)$ is a further random variable which at long times is distributed with the same power law relationship as the individual trap times t_2[55]. The importance of this fact is that at long time delays the power law behavior is independent of the choice of γ_{esc}, and so the gradients of the log-log plots in Fig. 2 can be taken as equal to $-(1 + \mu)$. The effect of the three fitting parameters on the Monte Carlo simulation as described above is illustrated in Fig. 4.7.

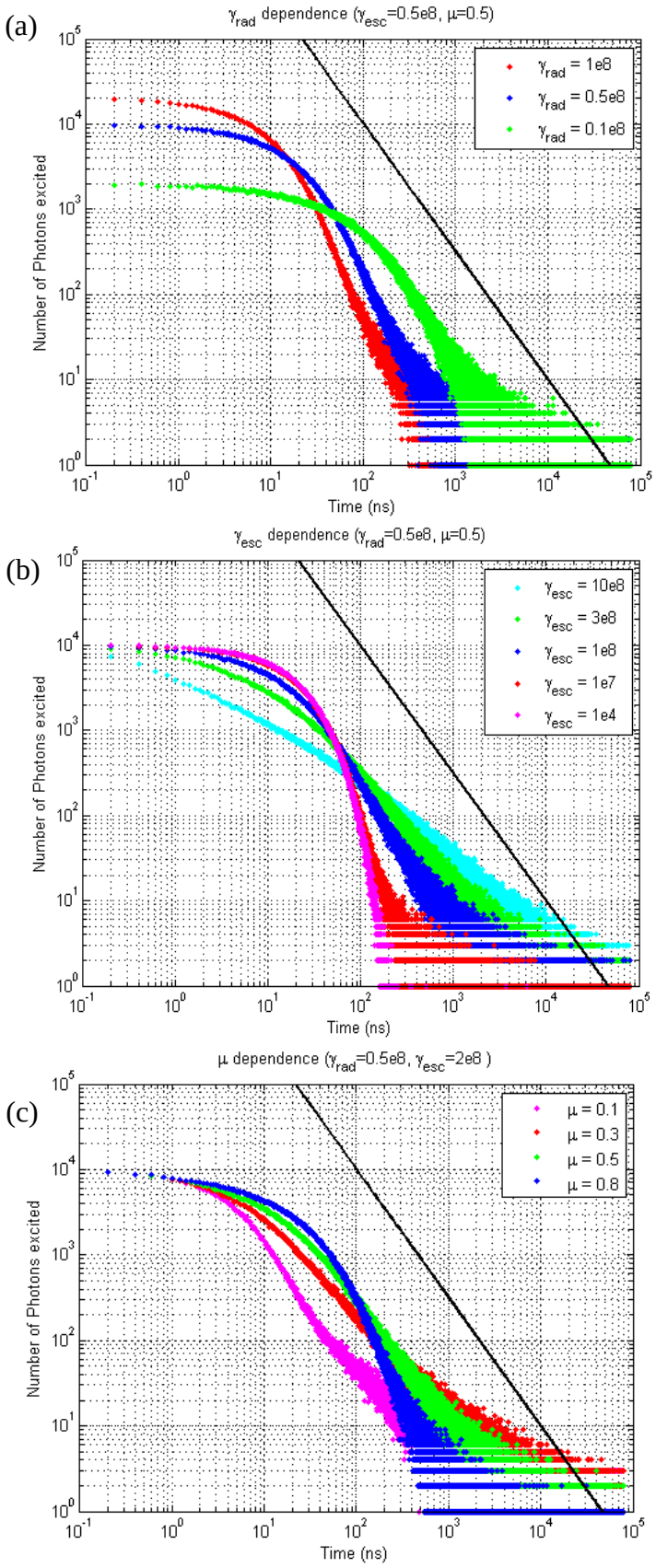

Fig. 4.7. The effect of varying fitting parameters, (a) $\gamma_{rad,}$ (b) $\gamma_{esc,}$ and (c) μ , on the Monte Carlo simulation. In each plot the solid black line is an analytical power law function with power law coefficient $\mu = 0.5$.

Inherent in our model are the assumptions that all of the fluorescence measured is a result of the most recent excitation pulse and that the fluorescence from nanocrystals in the off state is negligible. Klimov et al. have reported that weak Auger-limited fluorescence decay can be observed from nanocrystals in the *off* state or excited with a biexciton[56], but we neglect these processes so as to keep the number of fitting parameters small. The result is a model which provides high quality fits under conditions of weak excitation, and therefore is well suited to our ensemble TRPL data, but which does not follow the single nanocrystal data accurately at short delays. However, to confirm the deviation from the Monte Carol simulation to the single NC TRPL at short delay is due to Auger-limited fluorescence, we compared the ensemble TRPL measured at low peak intensity (~1kW/cm^2, typical for ensemble TRPL) and at high peak intensity (~20kW/cm^2, typical for single NC TRPL) respectively. The comparison measurement is qualitatively similar to the difference between simulation and single NC TRPL. For example the magnitude of the peak difference is small for core only NC whereas for core/shell NCs it is larger. Also, the deviation between low and high excitation intensity for QDQW begins at a longer time delay.

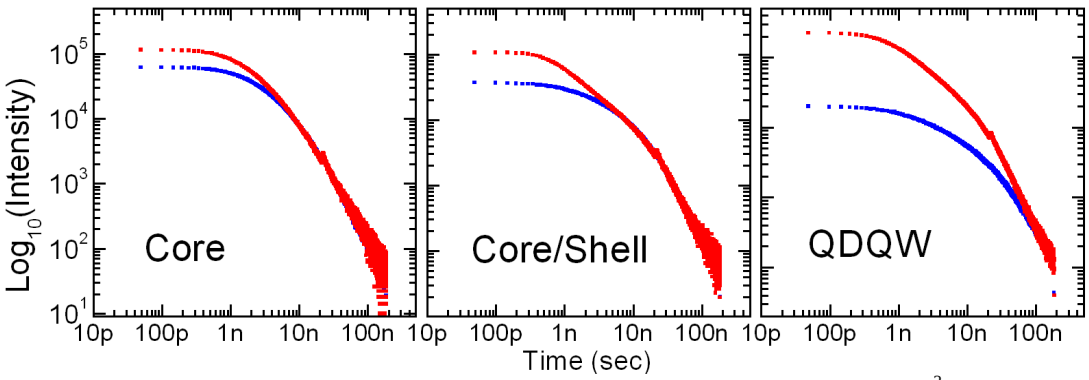

Fig. 4.8. Ensemble TRPL for three different types of NC measured at low (~1kW/cm^2, blue) and at high peak intensity (~20kW/cm^2, red) respectively.

Fits of our MC simulation data sets to the measured TRPL data are shown as gray scatter graphs overlaying the experimental data in Fig. 4.4. In all cases, the model provides exact fits to the experimental data for time delays greater than about 10 ns. The fitting parameters for the 12 Monte Carlo data sets in Fig. 4.4 are listed in Table 4.1, γ_{rad} and γ_{esc} are converted to an average lifetime $\tau=1/\gamma$ for easy comparison with the biexponential lifetime fits. We find that over the limited range of the single nanocrystal data it is possible to obtain good fits for a range of parameter values, and so in each case we have used the μ value from the ensemble fit and chosen τ_{rad} closest to the corresponding value obtained in the analytic biexponential fit. The tabulated parameters reveal that most of the differences between the data sets are primarily attributable to differences in τ_{esc}, which is determined by the degree of surface passivation of the individual nanocrystals. All values of τ_{esc} fitted are smaller than τ_{rad} shows that the off state plays an important role. The value of the simple three level Monte Carlo simulation lies in the fact that the long tail of the TRPL can be fitted exactly by noting that each is well described by a uniform power law function.

Table 4.1. Analytic biexponential fits τ_{1_exp} and τ_{2_exp}; Monte Carlo fitting parameters τ_{rad}, τ_{esc}, and μ for the best fits to the data shown in Fig. 4.4 and for the average μ values from the blinking data in Fig. 4.9. The numbers in parentheses represent estimated error bars for the values stated.

Sample	τ_{1_exp} (ns)	τ_{2_exp} (ns)	τ_{rad} (ns)	τ_{esc} (ns)	μ	μ_{blink}
Aens	-	-	14(2)	2 (1)	0.50(0.05)	0.54(0.05)
A1	2.2	21.7	14(2)	2.5(1)	0.50(0.1)	0.7
A2	1.9	21.5	14(2)	4 (1)	0.50(0.1)	
A3	2.7	31.3	20(2)	5 (1)	0.50(0.1)	
Bens	-	-	14(2)	2.5(1)	0.63(0.05)	0.67(0.05)
B1	2.0	20.2	14(2)	7 (1)	0.63(0.1)	
B2	1.4	26.0	20(2)	3 (1)	0.63(0.1)	
B3	1.8	17.3	12(2)	7 (1)	0.63(0.1)	
Cens	-	-	17(2)	6 (1)	0.50(0.05)	0.37(0.05)
C1	1.3	18.0	17(2)	10 (2)	0.50(0.1)	
C2	1.3	18.8	17(2)	10 (2)	0.50(0.1)	
C3	2.4	27.6	17(2)	10 (2)	0.50(0.1)	

An attempt to model the escape rate, γ_{esc}, which follows the *on* time power law function is to set $\gamma_{esc} = 1/t_i = t_b^{-1} x_i^{1/\mu_{on}}$. In this way, instead of using a uniform exponential escape rate, γ_{esc} is variable by sampling the *on* time power law function. However if we generate an intensity trajectory under such a condition the *on* time statistics still follows a single exponential rather than a power law. This is because each sampling of γ_{esc} from the power law only has a one-off effect during each iteration, therefore it converts the *on* time duration to a probability of whether the carrier will escape to a trap state but does not force the NC to stay *on* for that duration. Therefore even though γ_{esc} can take multiple exponential values from a power law distribution but the overall effect still 'average' to a single exponential.

The Monte Carlo simulation provides evidence that the tail of the TRPL follows a power law and the gradient is related to the power law exponent, μ, from blinking statistics. Tachiya et al. worked out an analytical solution to the three level system in time domain and Laplace domain[57] and showed that the tail of the TRPL is the asymptotic power law decay. Therefore, in practice one can extract the power law exponent from the tail of the TRPL by a simple linear fit. However care must be taken if the TRPL appears more like an exponential decay rather than an asymptotic gradient of the power law component.

4.3.1 Kinetic Monte Carlo (KMC) simulation

The Monte Carlo simulation steps through a small time-segment, Δt, in each iteration. During each iterations it checks through a set of conditions then decides whether or not to switch to a different state, and it is very likely for the simulation to remain in the current state by stepping through time without further changes. Even though such implementation is intuitive with a clear tracking of real time, it is not an efficient

algorithm as many processing cycles are wasted if the system remains unchanged within Δt. A more efficient algorithm is to trigger a change of state in each single iteration and then increment the time passed accordingly. Kinetic Monte Carlo is a modified Monte Carlo simulation that addresses the above issue for systems with exponential transition rates between two states.

The underlying assumptions for KMC algorithm are 1) the transition rates are Poissonian, and 2) the transition processes are independent, i.e. there is no memory. Now consider a system with a set of transitions U_i from state S_a into other possible states S_b. For each U_i there is a transition rate r_i where i loops over all possible transitions. During every iteration, we want a transition to be picked at random with a probability proportional to its transition rate (i.e. transition probability). The general KMC algorithm is summarised as follows:

0) Initial time to t = 0

1) Form a list of all the rates r_i of all possible transitions U_i in the system

2) Calculate the cumulative function $R_i = \sum_{j=1}^{i} r_j$ for i = 1,…,N where N is the total number of transitions. Denote R = R_N

3) Get a uniform random number $u \in (0, 1]$

4) Find the event to carry out i by finding the i for which $R_{i-1} < uR \leq R_i$

5) Carry out event i

6) Find all U_i and recalculate all r_i which may have changed due to the transition

7) Get a new uniform random number $v \in (0, 1]$

8) Update the time with t = t + Δt where

$$\Delta t = -\frac{\ln v}{R}$$

9) Return to step 1

The algorithm possess two main elements 1) the proportionality of picking an event, and 2) the stepping of time. Consider a system with possible transistions A→a, B→b and C→c and the transition rates r_1, r_2, and r_3 are associated with each transition respectively. Say the transition rates has an arbitrary value of r_1 = 0.4, r_2 = 0.6, and r_3 = 1.3 that corresponds to the cumulative functions R_1 = 0.4, R_2 = 1.0 and R_3 = 2.3. If we now plot r_i as regions and R_i as points on a line we get:

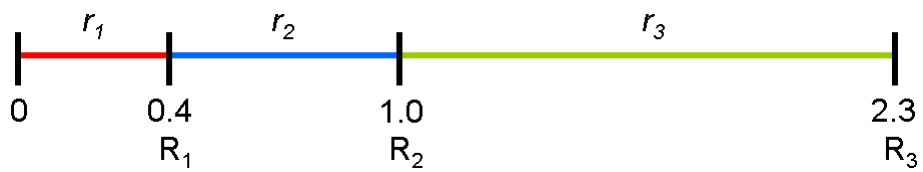

If we then multiply R (2.3 in this case) by a random number *u* between 0 and 1, then *uR* corresponds to a point on the line. The probability of picking an event, say r_3, is $1.0 < uR \leq 2.3$ therefore it is proportional to r_3/R, in other words the chance of picking a transition event corresponds to its transition rate, r_i. To prove the time advancement formula, consider an object with a uniform transition probability *r*, let *f* represent the transition probability density where *f(t)* gives the probability rate that transition occurs at time *t*, or in other words *f(t)* provides the probability density that particles still remain (a jump has not yet occurred) at time *t*. This can be formulated into a differential equation,

$$df(t) = -rf(t)dt \tag{4.3}$$

which has a solution of $f(t) = Ae^{-rt}$ and we know $f(0) = r$, i.e.

$$f(t) = re^{-rt} \tag{4.4}$$

since the transitions are Poissonian and are independent hence from the property of a Poisson distribution we know the overall system transition probability has the same characteristic as a single transition, i.e.

$$F(t) = Re^{-Rt} \tag{4.5}$$

where *F(t)* represents the overall system transition probability density and

$$R = \sum_{i}^{N} r_i \tag{4.6}$$

where N is the total number of possible transitions. Drawing a random number from the distribution described by Eq. 4.5 can be done analytically through the inversion method and it turns out to be

$$t = -\frac{\ln u}{R} \qquad (4.7)$$

where u is a uniform random number, and this is exactly the time advancement formula used in the KMC algorithm.

In practice, the KMC algorithm processing time is two orders of magnitude faster than the normal Monte Carlo. The significant improvement in processing speed allowed modelling of dynamics in the minutes regime based on nanosecond rates.

Taking advantage of the faster KMC algorithm, we can generate intensity trajectories in the minute regime. Our three level model is able to generate long *off* times with spiky *on* times that is typically found in our unwell passivated NC samples. Extracting the blinking *off*-time power law exponents from the simulated trajectories recovered the original power law exponents set in the model if the data is not binned, i.e. maintaining the minimum timing resolution at nanosecond regime. However, if the data are binned, the extracted power law exponent tends to be slightly smaller then the original value set in the model.

4.4 Relationship between TRPL and blinking

To probe the relationship between the fluorescence decay function and distribution of *off* times from blinking measurements, we performed both experiments simultaneously on the same nanocrystal. Pulsed excitation at a repetition rate of 500 kHz allowed us to use a TCSPC TAC window of 1 μs and a blinking sampling time of 50 ms. Fig. 4.9 shows both TCSPC and fluorescence *off* histograms for 14 single nanocrystals of the different types.

We have scaled the TCSPC data in Fig. 4.9 to enable the two data sets to be

presented on the same *y*-axis. The scaling factor used is the product of two subfactors—the first, F_1, corrects for the difference between the widths of the time bins, generally 50 ms for blinking and 200 ps for TCSPC, giving $F_1=2.5\times10^8$, while the second, F_2, corrects for the difference between the measurement efficiencies of the two methods. While the blinking data record all of the *off*-periods with duration >100 ms, the TCSPC data record a timing event for only about 4% of the excitation pulses so that $F_2 \approx 25$. The result of this scaling is therefore to shift the TCSPC data up the *y*-axis of the logarithmic plot by about ten decades without distortion to the curve shape.

Although there is clearly a large time gap between the two data sets and some variation between individual nanocrystals, in each case, their relative positions suggest that the power law decay at the short and long timescales measured here may be continuous across the entire time range with $\mu \approx 0.5$ throughout. There is also some correlation between the values of μ measured on different timescales. The mean values measured from the blinking data, listed alongside the ensemble fitting parameters for each of the three nanocrystal types in Table 4.1, agree well with those fitted to the ensemble TRPL tails, with nanocrystals of type B providing a noticeably larger value of μ in both measurements. This degree of correspondence between the two data sets provides further evidence that the tail in the fluorescence decay is a result of the same trapping behavior that causes fluorescence blinking. The diffusion based models of Refs. [26] and [28] suggest a change in power law exponent at some time t_c, however the correlation between the values of μ at 100 ns timescale and the value found in the blinking analysis suggested an unchanged power law exponent over the time range measured.

Table 4.2 gives the characterizing parameters for each NCs data illustrated in

Fig. 4.9. The power law coefficient for blinking is calculated by a linear least-square fit through a long event weighted blinking probability distribution. This method may over estimate the power law coefficient since it gives more weight to the long time events, such result is also found by other researchers[58].

To summarise, our study provides evidence that the same carrier trapping dynamics that lead to power law statistics in fluorescence blinking of single semiconductor nanocrystals can be observed on much faster timescales in fluorescence decay experiments.

Table 4.2. Analytic biexponential fits τ_{1_exp} and τ_{2_exp}; Monte Carlo fitting parameters τ_{rad}, τ_{esc}, and μ for the best fits to the TRPL data and μ_{blink_off}, μ_{blink_on} for blinking histograms shown in Fig. 4.9**Fig. 4.4**. The numbers in parentheses represent estimated error bars for the values stated.

Sample	τ_{1_exp} (ns)	τ_{2_exp} (ns)	τ_{rad} (ns)	τ_{esc} (ns)	μ	μ_{blink_off}	μ_{blink_on}
A1_NC8	2.2	22	20	3.5(1)	0.2 (0.1)	0.75(0.1)	0.75(0.1)
A2_NC6	1.9	22	20	5 (2)	0.3 (0.1)	0.55(0.05)	0.6 (0.1)
A4_NC9	1.8	16	17	10 (5)	0.4 (0.1)	0.8 (0.05)	0.4 (0.1)
A5_NC10	2.8	22	20	3.5(1)	0.25(0.1)	0.7 (0.1)	0.5 (0.1)
B4_NC10	1.7	22	20	5 (2)	0.6 (0.1)	0.7 (0.1)	0.8 (0.1)
B5_NC11	1.0	9	9	7 (3)	0.6 (0.1)	0.6 (0.1)	0.8 (0.1)
B6_NC12	1.2	17	17	7 (3)	0.6 (0.1)	0.8 (0.1)	0.7 (0.1)
B7_NC13	1.2	12	13	8 (4)	0.8 (0.1)	0.95(0.05)	0.1 (0.1)
B8_NC14	1.3	14	14	9 (5)	0.6 (0.1)	0.85(0.1)	0.2 (0.1)
C4_NC11	1.2	10	10	5 (2)	0.3 (0.1)	0.55(0.05)	0.8 (0.1)
C5_NC12	1.7	18	20	7 (3)	0.6 (0.1)	1.0 (0.1)	0.3 (0.1)
C2_NC5	2.0	21	20	5 (2)	0.5 (0.1)	0.6 (0.1)	0.7 (0.1)
C6_NC3	1.9	23	25	5 (2)	0.5 (0.1)	0.6 (0.1)	0.7 (0.1)
C7_NC4	1.9	25	25	5 (2)	0.6 (0.1)	0.55(0.05)	0.3 (0.1)

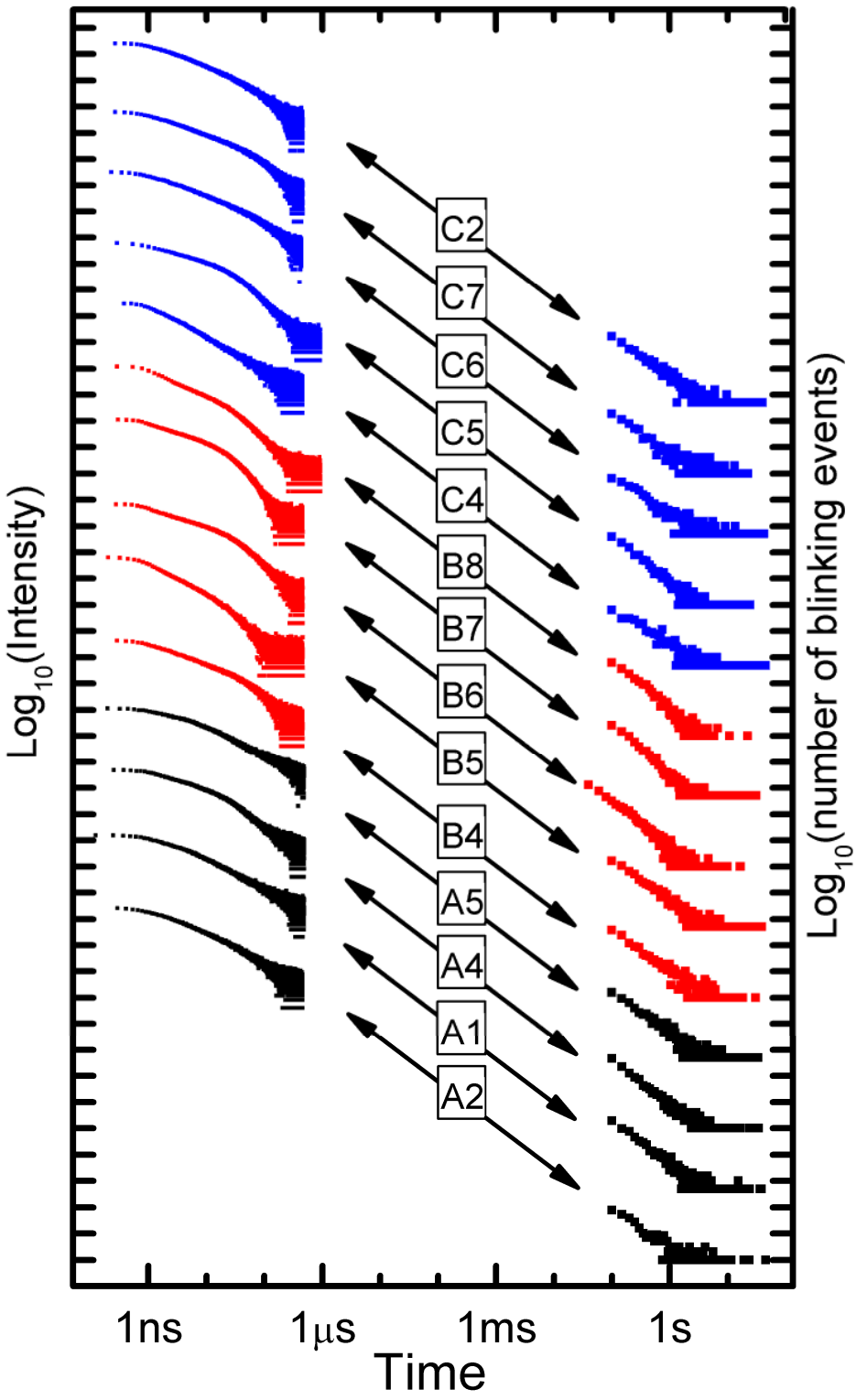

Fig. 4.9. TCSPC and blinking data histograms on common logarithmic axes for 14 different single nanocrystals. The increments on both axes of the figure correspond to factors of 10.

4.5 Low Temperature TRPL

One obvious question to ask is what happens when we turn down the temperature. Norris et al.[14] experimentally verified the fine structure splitting of exciton state. The energy difference between the bright exciton (higher in energy) and the dark exciton (lower in energy) for the size of our nanocrystal (~5 nm) is about 1 meV. Consider the thermal energy, kT, at RT is ~25.7 meV, ~6.6 meV at 77K, and ~0.3 meV at 4K, therefore as the temperature decreases below 77K we will expect the thermally activated depopulation of the dark exciton state to the bright exciton state to be less efficient, hence results in an increased radiative decay lifetime. Crooker et al.[52] measured the TRPL decay of CdSe and CdSe/ZnS NCs (size ~2 nm) at temperatures ranging from 0.38 K to 300 K. They found a rapid increase in lifetime as the temperature drops below 100K and the lifetime can reach as long as 1μs at 1K and below. Assuming the lifetime is inversely proportional to the NC size, a rough estimate from their size dependence data suggested a 200 ns lifetime for the size of our NC at 4.2K.

Fig. 4.10 shows the TRPL of a core/shell ensemble (Evident Technology, Evi620) at three different temperatures. The complete decay curve is a combination of two data sets measured with different TAC windows, this is so that the tail at long delay can be captured but maintaining a good timing resolution at short delay. The overlap between the two curves is over two decades in time (10ns to 1μs) but the tail of the left hand curve (300 ns to 1μs) is deleted for clarity. At room temperature both an exponential and a power law component is evident and the curves meet at about 100 ns. A bi-exponential fit at the short time regime gives two time constants of 2.5 ns and 16 ns respectively. The 16 ns time constant matches well with the usual 20 ns

radiative lifetime measured from core/shell NCs. The power law component has a gradient of -1.46. At 77K, the exponential component is qualitatively the same and a bi-exponential fit gives a lifetime of 15 ns. However the power law exponent appears to have changed dramatically at times less than a few microseconds, to a value of about 0.7, and is suppressed so that the exponential behaviour is much more visible. Beyond 2 μs the power law exponent appears to increase to 1.4. The change in power law behaviour at 2 μs may provide some evidence for a diffusion controlled carrier dynamics, moreover the temperature dependence of this behaviour could shed more light on the exact mechanism that is diffusing. At 4K, the radiative lifetime appears to have increased as expected, a bi-exponential fit to the time region from 10 ns to 2 μs gives a radiative lifetime of 198 ns, similar to what we estimated from Crooker's paper. The increased radiative lifetime dominates the TRPL decay up to long delays and it makes the power law component less obvious. In the time regime from 0.4 ns to 10 ns the decay deviates from what we would expect from a pure exponential radiative decay. This may be due to the inhomogeneity of the ensemble in which some of the larger NCs may have a smaller fine structure splitting such that even at 4K the bright exciton state is thermally populated. Such NCs would have a shorter radiative lifetime and would dominate the TRPL at shorter time regime.

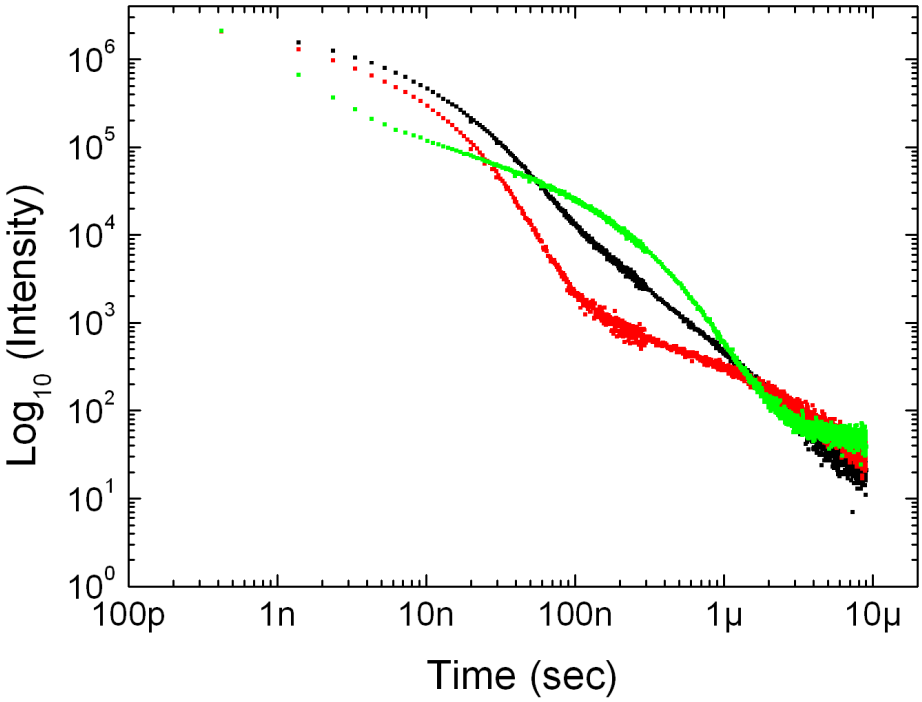

Fig. 4.10. A plot for Evi620 (core/shell) ensemble TRPL at RT(black), 77K (red) and 4K (green). Each curve is a combination of two data sets measured with a TAC window of 1µs and 10µs respectively. Each curve is scaled to a same peak at shortest time delay for direct comparison. The larger time constant from a bi-exponential fit (not shown) gives lifetime values as 16 ns (RT), 15 ns (77K), and 198 ns (4K). The power law exponents are 1.5 (RT), 1.4 or 0.7 (77K). See text for detail.

If we turn to a different core/shell NC (CdSe/ZnS, Manchester University, OMN13) that has an average size of 6 nm where the TRPL decay is shown in Fig. 4.11. These NCs are less well passivated therefore the exponential component at RT is less obvious, but the power law component is clear and holds a value of 1.56. At 77 K, a bi-exponential fit to the short time regime gives a radiative lifetime of 14 ns. There is still a hint of change in power law gradient at around 2 µs where it changes from 1.2 to 1.5. These NCs are larger on average therefore a considerable amount of NCs in the ensemble may have a fine structure splitting smaller then kT at 4K, hence these NCs with short lifetime will dominate the 4K TRPL in short time delay. However a contribution from the increased radiative lifetime is pointed out by the curvature at ~200 ns. The power law tail is more obvious in this case but will need to go to longer time delays for a more accurate justification.

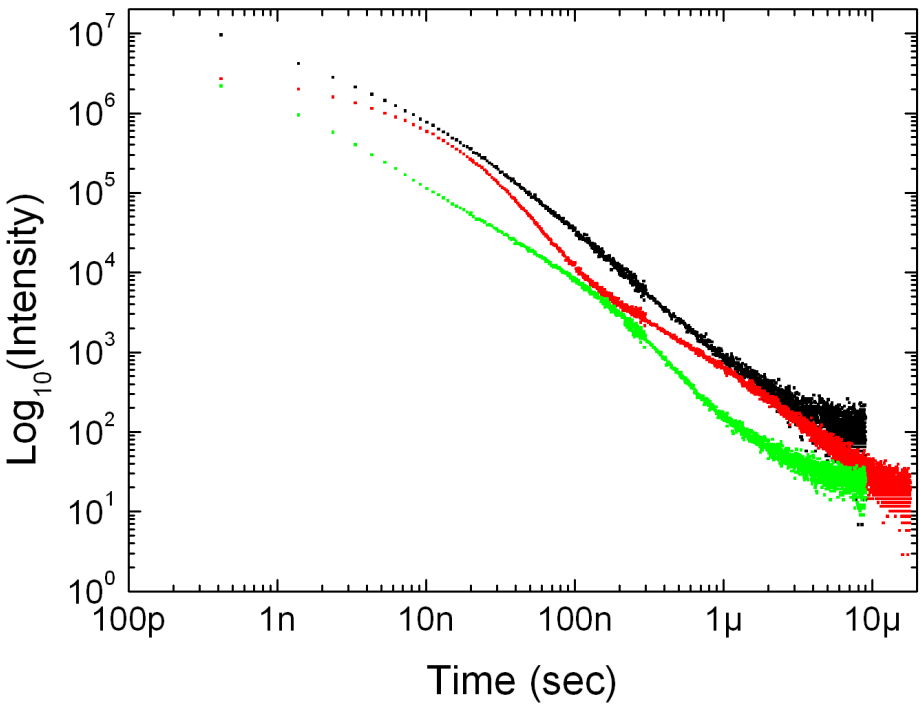

Fig. 4.11. A plot for OMN13 (core/shell) ensemble TRPL at RT(black), 77K (red) and 4K (green). Each curve is a combination of two data sets measured with a TAC window of 1µs and 10µs respectively. Each curve is scaled in y-axis for clarity. The larger time constant from a bi-exponential fit (not shown) gives lifetime value of 14ns at 77K. The power law exponents are 1.6 (RT), 1.5 or 1.2 (77K). See text for detail.

Fig. 4.12 shows the TRPL for a core only NC ensemble (CdSe, Manchester University). As one would expect the core only NCs are not well passivated therefore it shows a weak exponential component from the TRPL. At 4K, the normal radiative lifetime due to bright excitons still appeared to have a substantial contribution in the TRPL, this suggested a smaller splitting that is comparable to kT at 4K. Nevertheless the shoulder at 200 ns still suggested a possible increase in radiative lifetime, although it can be ambiguous whether this small curvature is due to a longer life time or is it representing the power law tail. The power law component at RT is clear, with an exponent of 1.81, and again we observe a change upon cooling to 77K. This time up to ~1 µs, the exponent reduces to 1.0 and beyond that time it is unchanged at 1.8.

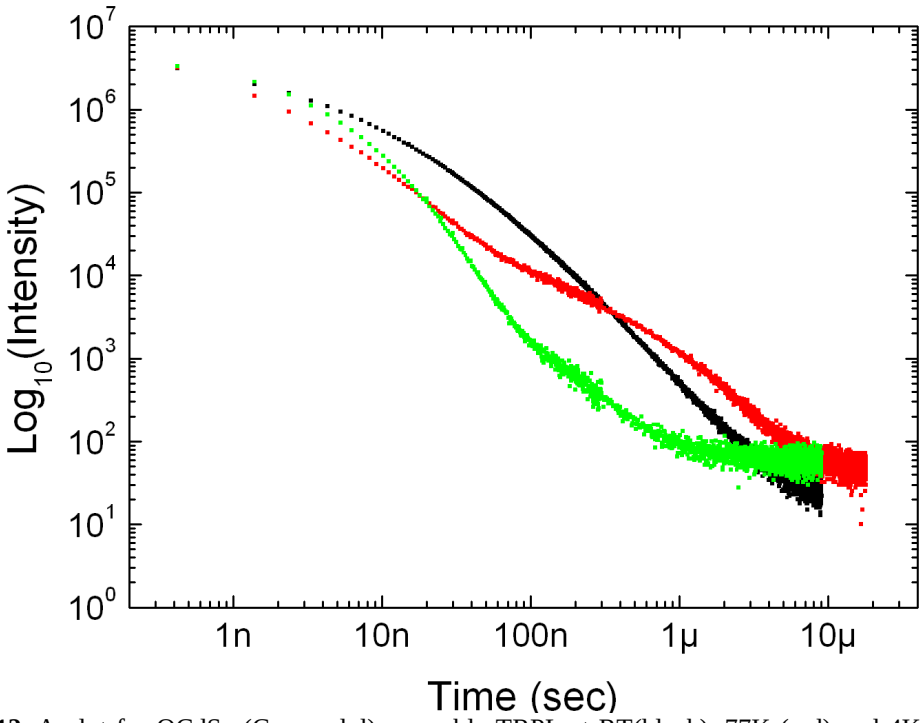

Fig. 4.12. A plot for QCdSe (Core onlyl) ensemble TRPL at RT(black), 77K (red) and 4K (green). Each curve is a combination of two data sets measured with a TAC window of 1μs and 10μs respectively. Each curve is scaled in y-axis for clarity. The power law exponents are 1.8 (RT), 1.8 or 1.0 (77K), 1.3 (4K). See text for detail.

The temperature dependent TRPL for a QDQW sample (NC3, Manchester University) is shown in Fig. 4.13. The radiative lifetime at RT and 77K is 10.3 ns and 9.5 ns respectively, and increases to 179 ns at 4K. The power law exponent at RT is 1.66 and at 77K is 1.1, although we did not observe the change in power law at 77K like the other samples, it is possible that the change will occur at a longer time delay.

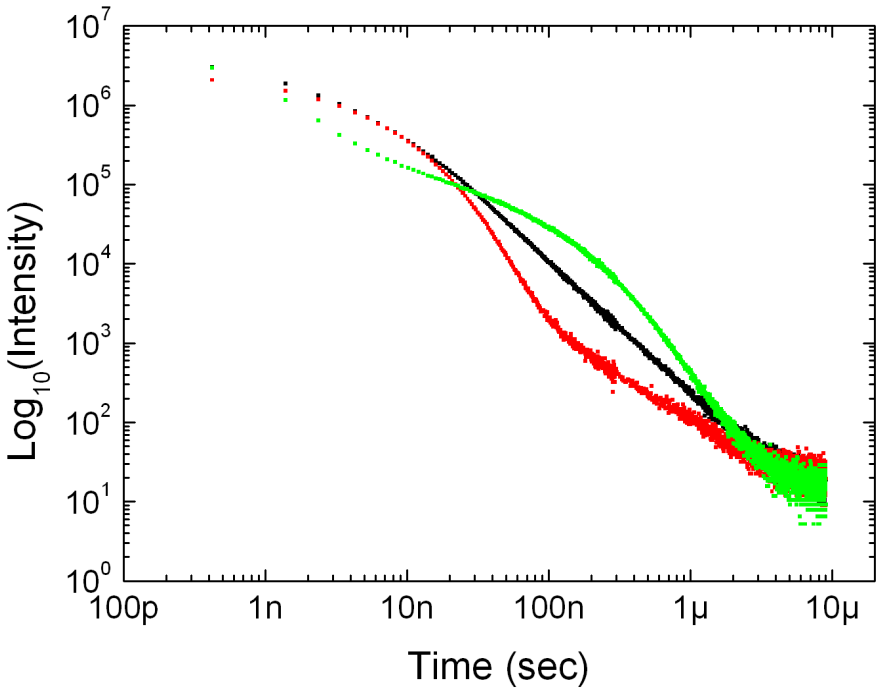

Fig. 4.13. A plot for NC3 (QDQW) ensemble TRPL at RT(black), 77K (red) and 4K (green). Each curve is a combination of two data sets measured with a TAC window of 1μs and 10μs respectively. Each curve is scaled in y-axis for clarity. The larger time constant from a bi-exponential fit (not shown) gives lifetime values as 10 ns (RT), 9.5 ns (77K), and 179 ns (4K). The power law exponents are 1.7 (RT), 1.1 (77K). See text for detail.

4.6 Discussion

The success of our three level Monte Carlo model allowed us to interpret the multiexponential nature of a single or an ensemble TRPL decay in terms of power law dynamics with the exponent μ. The power law interpretation is particularly effective at fitting the TRPL decay at longer time delays. In addition the same model can be as effective in explaining dynamics at shorter time delay. Three different publications[46, 47, 59] are devoted to investigate the fluctuation in radiative decay of single NCs at different emission intensity level. In particular, they found the TRPL decay behaving like a single exponential with a decay lifetime of ~20 ns when the emission intensity is at maximum, whereas a multiexponential decay consisting a fast component (~1 ns) is found at a much lower intensity. Fig. 4.14 re-plots Fig. 4.7(b) on a log-linear axis and we immediately noticed the similarity between the

simulation results and the experimental data presented in the three papers mention above. When the carrier escape rate is low (γ_{esc} = 1e4) the simulated data resembles the single exponential radiative decay, whereas when the carrier escape rate is high (γ_{esc} = 10e8 or τ_{esc} = 1 ns) the simulation results in a multiexponential decay and by fitting a single exponential to the fast decaying component we obtained a lifetime of 1 ns. This picture coincides with the experimental data such that at maximum intensity one would expect a small escape rate and the TRPL decay represents the radiative recombination lifetime, whereas at low emission intensity the escape rate is expected to be high. By comparing the log-linear plot and the log-log plot, we noticed the "fast" decaying component is an extension of the same power law into shorter time regime. The author of the literatures attempted to rationalise the fast decaying component through a fluctuating nonradiative rate, whereas our simulation varies the carrier escape rate. However the two interpretations can point to a similar process since the carrier escape rate may be related to the non-radiative auger recombination. In addition, by noting the multiexponential decay at short time regime (< 10 ns) may be an extension of the same power law provides evidence to the fluctuating non-radiatve rate model as a potential theory to explain power law carrier dynamics.

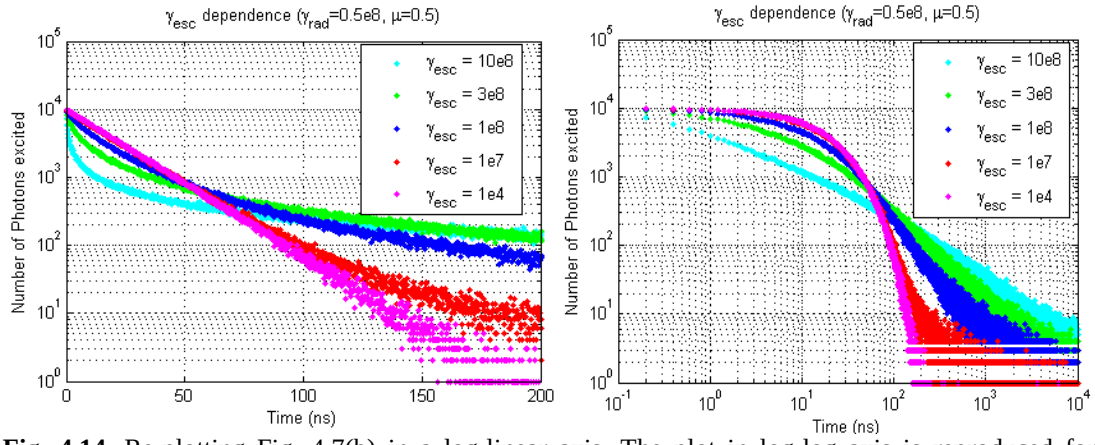

Fig. 4.14. Re-plotting Fig. 4.7(b) in a log-linear axis. The plot in log-log axis is reproduced for comparison.

Our combination of TRPL and blinking experiments at room temperature suggested the power law exponent might be continuous over 10 decades in time. However some preliminary low temperature TRPL experiments suggested a change in power law at the time regime of about 1μs when cooled to 77K. Within this picture, a diffusion-controlled model is more promising while the temperature dependency gives more clues to what mechanism is actually "diffusing". The Diffusion Controlled Electron Transfer (DCET) model assumed a spectral diffusion of the quantum dot and traps energy states along some reaction coordinate. At the vicinity of the crossing point between the two diffusing energy states the power law exponent changed to a value of 1/2. A critical time t_c is associated to diffusion process on how long the energy states remain in resonance. At higher temperature the diffusion constant can be so large that t_c is shorter than nanoseconds which can not be observed from our TRPL experiments, however as the temperature is lowered the diffusion constant becomes smaller such that t_c is extended to longer time regime that is then captured by our TRPL experiment. A full temperature dependent experiment would reveal whether t_c will change with temperature and can provide more insight into the power law dynamics.

Some results in the chapter are published in Applied Physics Letter, Volume 92, Issue 10, Article No. 101111 (2008).

Chapter 5
Single NC Analysis II –Autocorrelation

The intensity time trace of a single NC can be recorded with a minimum time resolution of 25 ns using the TCSPC card in time tagging mode. An autocorrelation function can then be calculated from this time trace to analyze the intensity fluctuations without setting an arbitrary threshold. This can potentially improve the timing resolution of the intensity fluctuation analysis significantly. Although an arbitrary threshold is not necessary, the overall contrast of the autocorrelation function is still affected by the signal to background ratio, therefore a practical limit to the minimum timing resolution of autocorrelation analysis for single NCs is about 1 μs. However in our setup the autocorrelation function in the short time regime is skewed by an artifact caused by afterpulses in the single photon detectors thus the practical limit in our setup is ~ 5 μs. Nevertheless the timing gap between TRPL decay and blinking statistics, i.e. 1 μs (for single NCs) or 10 μs (for ensembles) to 50 ms, may be filled by autocorrelation ($g^{(2)}$) measurements.

5.1 What is Autocorrelation?

In statistics, the correlation between two random variables is defined by the correlation function, while the autocorrelation function is the correlation between the

random variable with itself at a different point in space or time. The temporal autocorrelation coefficient, *R(τ)*, is defined as

$$R(\tau) = \frac{\left\langle \left(X(t) - \bar{X} \right) \left(X(t-\tau) - \bar{X} \right) \right\rangle}{\sigma^2} \qquad (5.1)$$

where *X(t)* is the value of the random variable at time *t*, $\bar{X}$ is the mean of the random variable, τ is the lag time, and σ^2 is the variance of the random variable.

Let us now switch to optics and consider an unnormalized autocorrelation function, *G(τ)*, for an array of intensities at time *t*, *I(t)*.

$$\begin{aligned} G(\tau) &= \left\langle \left(I(t) - \bar{I} \right) \left(I(t-\tau) - \bar{I} \right) \right\rangle \qquad (5.2) \\ &= \left\langle I(t) I(t-\tau) - I(t) \bar{I} - I(t-\tau) \bar{I} + \bar{I}^2 \right\rangle \\ &= \left\langle I(t) I(t-\tau) \right\rangle - \left\langle I(t) \bar{I} \right\rangle - \left\langle I(t-\tau) \bar{I} \right\rangle + \bar{I}^2 \\ &= \left\langle I(t) I(t-\tau) \right\rangle - \bar{I}^2 \qquad (5.3) \end{aligned}$$

If now we normalize *G(τ)* with the square of average intensity $\left\langle I(t) \right\rangle^2$ instead of the variance and noting that $\left\langle I(t) \right\rangle = \bar{I}$, we get the autocorrelation function, $g^{(2)}(\tau)$, in the usual form,

$$\frac{G(\tau)}{\left\langle I(t) \right\rangle^2} = \frac{\left\langle I(t) I(t-\tau) \right\rangle}{\left\langle I(t) \right\rangle^2} - 1 \qquad (5.4)$$

$$g^2(\tau) \equiv \frac{\left\langle I(t) I(t-\tau) \right\rangle}{\left\langle I(t) \right\rangle^2} \qquad (5.5)$$

The $\langle\ \rangle$ in the above equations represent ensemble or statistical averaging. However, with the assumption of ergodicity and stationarity, the ensemble average is calculated in practice using time average.

G(τ) as denoted in Eq. 5.2 monitors the fluctuation in the stream of intensity signals with respect to the mean intensity. However it requires one to keep a running

measure of the mean intensity which imposes complication in the calculation. In practice it is common to measure *I(t)* then calculate $g^{(2)}(\tau)$ that represents the correlation between the intensity at time *t*, *I(t)*, and at a later time delayed by $t+\tau$, $I(t+\tau)$. Therefore by calculating the probability of detecting a second photon at a time delay τ after the first detection, $g^{(2)}(\tau)$ provides information on whether the detection of a second photon is related to the first one, i.e. if there is any 'memory' in the underlying physical system that governs the fluctuation in intensity and how long the memory may last. For example, consider a coherent chaotic light source, one would expect the photons to arrive at random therefore no correlation between photon arrival times, $g^{(2)}(\tau) = 1$ for any value of τ. On the other hand, consider an ensemble of some free moving fluorescent particles under a confocal microscope, the fluctuation in overall intensity will depend on the number of particles diffusing in and out within the field of view and the individual phosphor intensity fluctuation. Therefore by analysing the change in $g^{(2)}(\tau)$, one can determine the diffusion coefficient and the photophysics of individual phosphors occurring at different time scales. Certainly for an immobilized ensemble or a single particle, $g^{(2)}(\tau)$ will only represent the time correlation resulting from the physical process behind the fluorescence intensity fluctuation.

The reason why one would normalize with $\left\langle I(t)\right\rangle^2$ is so that for $\tau = 0$,

$$g^{(2)}(0) = \frac{1}{\langle N \rangle} \qquad (5.6)$$

therefore relating the zero delay autocorrelation amplitude to the average number of emitting particles, $\langle N \rangle$, within the field of view. This may be proved as follows, for a random process with discrete occurrences within a certain time-interval, i.e. a Poisson distribution, the variance and the mean are equal. The average number of

particles within the field of view, <*N*>, and the fluctuation above and below this mean, δN, caused by diffusion of particle in to and out of the field of view is a Poission distribution. Hence the variance, $\langle (\delta N)^2 \rangle$, is equal to the mean, <*N*>. At $\tau = 0$

$$\frac{G(0)}{\langle I(t)\rangle^2} = \frac{\left\langle \left(I(t)-\bar{I}\right)^2 \right\rangle}{\langle I(t)\rangle^2} = \frac{\text{Variance}}{\bar{I}^2} \qquad (5.7)$$

for some constant *x*

$$\left\langle (\delta I)^2 \right\rangle = x^2 \left\langle (\delta N)^2 \right\rangle = x^2 \langle N \rangle \qquad (5.8)$$

$$\langle I \rangle = x \langle N \rangle \qquad (5.9)$$

Since both the variance and mean intensity in Eq. 5.7 is proportional to <N>, thus we obtain Eq. 5.6.

With regards to optics, first-order coherence refers to the first-order electric-field correlation function whilst the intensity autocorrelation function is regarded as the degree of second-order coherence, denoted by the superscript $^{(2)}$ in $g^{(2)}(\tau)$, because the optical intensity is related to the electric field as,

$$I(t) = E^*(t) \times E(t) = |E|^2 \qquad (5.10)$$

5.2 Relating g(2) to power law dynamics

The procedure to obtain autocorrelation function, $g^{(2)}$, from a series of photon arrival times is described in chapter 3, however to analysis the $g^{(2)}$ function and extracting the underlying power law exponents we followed the derivation published by Verberk and Orrit[60], where the relevant results are summarized as follows.

We wish to derive an analytical form of the autocorrelation function that

describes an intensity signal switching randomly between an *on*- and an *off*-state. Assuming a random telegraph with unambiguously defined *on* and *off*-periods with intensity signals 1 and 0. Let $P_I(\tau)$ and $P_O(\tau)$ represent the probability distribution of *On*- and *Off*-times of duration τ, where $p_I(s)$ and $p_O(s)$ are their corresponding Laplace transforms. We then define the average duration of *on*- and *off*-times by

$$T_I = \int_0^\infty \tau P_I(\tau) d\tau \qquad (5.11)$$

$$T_O = \int_0^\infty \tau P_O(\tau) d\tau \qquad (5.12)$$

The unnormalized correlation function, defined as $G(\tau) \equiv \langle I(t) I(t-\tau) \rangle / \langle I(t) \rangle$ in Ref[60], can be interpreted as the probability of finding a photon at time τ knowing that a photon is detected at time $t = 0$. This may be represented by the sum of different combinations of probabilities $P_I(\tau)$ and $P_O(\tau)$. For a deterministic alternation, i.e. an *off*-state immediately follows an *on*-state and vice versa, the Laplace transform of the unnormalized correlation function $G(\tau)$ is found to be,

$$g(s) = \frac{1}{s} - \frac{1}{s^2 T_I} \frac{(1 - p_I(s))(1 - p_O(s))}{1 - p_I(s) p_O(s)} \qquad (5.13)$$

For a single exponential distribution of on-times,

$$P_I(\tau) = a_I e^{-a_I \tau} \qquad (5.14)$$

its Laplace transform is,

$$p_I(s) = \frac{a_I}{s + a_I} \qquad (5.15)$$

Substituting Eq. 5.15 into Eq. 5.13 and noting that the average *on* time $T_I = 1/a_I$. With some algebra one will obtain,

$$g(s) = \frac{1}{s + a_I(1 - p_O)} \qquad (5.16)$$

If we now consider a probability distribution that follows a power law such as the one found in blinking statistics,

$$P(\tau) = A\tau^{-m} \qquad (5.17)$$

In probability theory, the Laplace transform of a probability density function for a random variable is defined through its expectation value. For a true power law distribution the average (first moment) is formally infinite therefore the Laplace transform for Eq. 5.17 is not well defined. Another way to look at this is that the Laplace transform integral will simply not converge. In order to define *p(s)* it is necessary to introduce short (θ) and long (Θ) cutoff times such that the power law distribution is valid only for $\theta < \tau < \Theta$ and outside this range it decreases to zero much faster. With the limits, the expected duration *T* (average time) drawn from this probability distribution is again well defined. The sum of probabilities within the cutoff limits is equal to one, therefore the normalization factor *A* can be determined by evaluating the integral $\int_\theta^\infty A\tau^{-m} d\tau = 1, \quad m > 1$ and found to be,

$$A = (m-1)\theta^{m-1} \qquad (5.18)$$

The cutoff limits changed the Laplace transform into an incomplete gamma function,

$$p(s) = \int_\theta^\Theta A\tau^{-m} e^{-st} d\tau \qquad (5.19)$$

This expression can be further simplified by replacing the exponential in the integral by 0 for $\tau > 1/s$ and by 1 for $\tau < 1/s$, it is then evaluated as

$$p(s) \approx 1-(\theta s)^{m-1} \qquad (5.20)$$

Substituting Eq. 5.20 into Eq. 5.16 and noting that $\langle I(t) \rangle = T_I / (T_I + T_O)$ we obtain the normalized correlation function of the form,

$$g^{(2)}(s) = T_O (\theta s)^{1-m} \qquad (5.21)$$

Noting the inverse Laplace transform $\mathrm{L}^{-1}\left[1/s^{v+1}\right] = t^v/\Gamma(v+1), \quad v > -1$ from tables, we obtain the correlation function for NCs with single exponential *on*-times and power-law distributed *off*-times,

$$g^{(2)}(\tau) = T_O \frac{\theta^{1-m}}{\Gamma(m-1)} \tau^{m-2} \qquad (5.22)$$

Finally consider the case where both *on*- and *off*-times are power law distributed. Substituting Eq. 5.20 into Eq. 5.13 with the power law exponents m_I and m_O for *on*- and *off*-times respectively.

$$\begin{aligned} g(s) &= \frac{1}{s} - \frac{1}{s^2 T_I} \frac{(\theta s)^{m_I + m_O}}{(\theta s)^{m_I+1} + (\theta s)^{m_I+1} - (\theta s)^{m_I+m_O}} \\ &= \frac{1}{s} - \frac{1}{s^2 T_I} \frac{1}{(\theta s)^{1-m_I} + (\theta s)^{1-m_O} - 1} \end{aligned} \qquad (5.23)$$

Since the short time cutoff, θ, is supposed to be small, the larger of the power law exponent m_I or m_O will dominate the denominator, thus by assuming m_O is larger, the expression can be simplified to,

$$g(s) = \frac{1}{s} - \frac{\theta^{m_O-1}}{T_I} s^{m_O-3} \qquad (5.24)$$

where the unnormalized correlation function can again be determined from Laplace transforms tables as,

$$G(\tau) = 1 - \frac{\theta^{m_O - 1}}{T_I \Gamma(3 - m_O)} \tau^{2 - m_O} \qquad (5.25)$$

Note that the approximation provides a convenient analytical solution in the τ-space that can be used to determine the magnitude of the larger exponent, however the information on the correlation between m_{on} and m_{off} are lost by doing so. Nevertheless, Eq. 5.22 and Eq. 5.25 are the main results that we can use to fit the autocorrelation function data measured from experiments.

5.3 Fitting theoretical function to data

The theoretical derivation of the autocorrelation function, $g^{(2)}(\tau)$, for single NCs with power law distribution of on- and off-times requires an arbitrary cutoff limit in both long and short time regimes. Although it is not certain whether such limits exist, there is some experimental evidence suggesting the power law behaviour of blinking statistics may not be universal over all time regimes. The on-time roll off from a pure power law in the seconds time regime has been reported[29], this suggested an upper limit to the on-time power law. The upper limit for off-time power law is not observed in single NCs experiments which leads to a claim of nonergodicity and statistical aging in NC fluorescence[11]. However a later report on the fluorescence decay from ensembles of NCs indicated that the fluorescence intensity tends to a steady state[61]. The authors claimed that this is in contrast to the previous report where a nonergodic system will predict a long term ensemble intensity towards zero due to statistical aging (i.e. all NCs will eventually enter an infinitely long off state). Instead, the experimental results have led the authors to claim an upper limit in the fluorescence off-time power law. Of course the limit

varies from sample to sample, but as the experimental result shows, it lies in the order of 10^3 seconds. From our data we also observed the exponential on-time roll off from the pure power law in the time regime of seconds (Fig. 5.1). For some NCs the long off-time tail also deviates slightly from a pure power law but not significant enough to justify an exponential roll off as in on-time statistics.

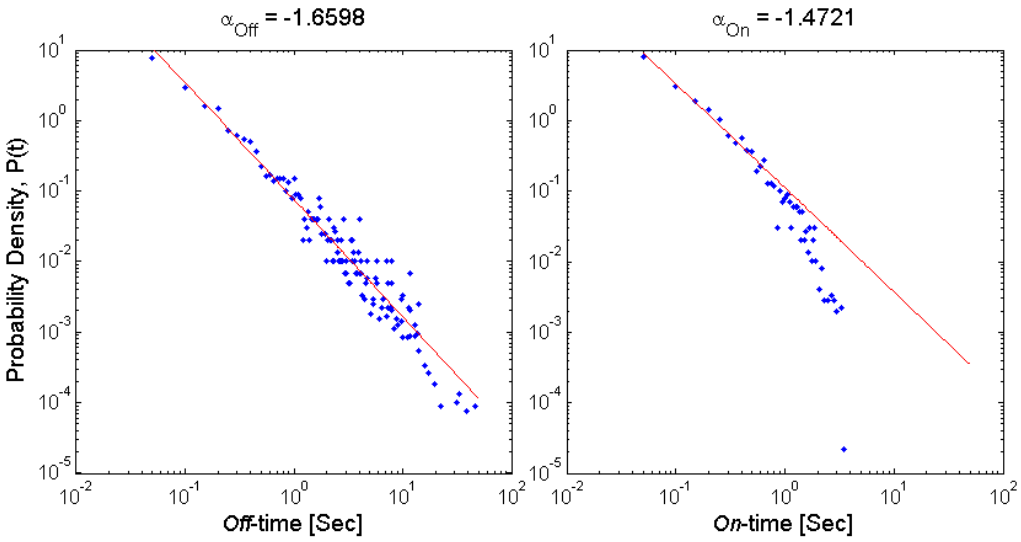

Fig. 5.1. One example of our core/shell NC blinking data with the off-time statistics showing a pure power law and the on-time statistics showing an exponential roll off from the power law at long time tail.

As previously shown from our TRPL results in the chapter 4, the power law dynamics may extend down to nanosecond regime, which is only limited by our experimental method. It is possible that other experimental techniques can probe the power law dynamics at even shorter time regime. In fact, to the best of my knowledge, the short time cutoff has never been observed experimentally. Therefore the short time cutoff, θ, needs to be introduced arbitrarily into the equation. The consequence of this arbitrary limit is that the autocorrelation analytical function presented in Eq. 5.22 and Eq. 5.25 can not be compared quantitatively to experimental results as its magnitude depends on the arbitrary short time cutoff, θ. Nevertheless, we can still qualitatively compare the analytical functions to our

autocorrelation results in order to extract the power law exponent by setting the arbitrary terms (θ, T_I, T_O) as a constant. Therefore, for NCs with exponential *on*-time, Eq. 5.22 states that

$$g^{(2)}(\tau) \propto \tau^{m-2} \qquad (5.26)$$

and for NCs with power law distributed *on* and *off* times, Eq. 5.25 states that

$$G(\tau) = 1 - B\tau^{2-m} \qquad (5.27)$$

or

$$g^{(2)}(\tau) = A\left(1 - B\tau^{2-m}\right) \qquad (5.28)$$

where A and B are constants.

For single NCs with single exponential *on*-time and power law *off*-time, Eq. 5.26 shows that the autocorrelation function on a log-log plot will be a straight line with gradient equal to *m-2*, thus by a linear fit on the log-log plot we can extract the power law exponent easily. This form of the autocorrelation function has been observed on bare NCs by Verberk et al.[32] that extends from seconds down to microseconds. We observed a similar form of autocorrelation however, only in a certain time regimes where there is an exponential roll off for the *on*-time statistics.

For the case where both the *on*- and *off*-times have a power law distribution, the autocorrelation function in the s-space is expressed by Eq. 5.23. In order to simplify the expression so that the inverse Laplace transform can be calculated analytically, the denominator involving power law exponents can by approximated by the single dominating term that has the largest exponent. We tried some figures to estimate the necessary difference between the exponents for the approximation to be valid. From our TRPL data presented in the previous chapter one can see that the power law exponent can be observed down to around 10 ns. If we assume $\theta = 1\text{x}10^{-10}$ sec then θ^{1-m} is evaluated as $1\text{x}10^{4}$(m = 1.4), $1\text{x}10^{5}$ (m = 1.5), and $1\text{x}10^{6}$

(m = 1.6), thus the difference between the exponent should roughly be larger than 0.1 for a valid approximation. Alternatively one can perform the inverse Laplace transform of Eq. 5.23 numerically to obtain a qualitative picture on the change in the autocorrelation function with respect to different *on*-and *off*-time exponents. The numerical inverse Laplace transform is computed in Matlab using a script created by Hollenbeck that makes use of the de Hoog algorithm[62]. To check whether the numerical algorithm is performing accurately, the approximated analytical expression (Eq. 5.25) is plotted with the numerical output in Fig. 5.2. The plot is generated from a set of constants, $\{\theta = 1\times10^{-9}$, $T_I = 1\times10^{-4}$ and $m_I = 1.4\}$, and with various m_o values. The numerical result follows the analytical solution closely when the difference between m_I and m_o is large (>0.2), hence it indicates the robustness of the numerical algorithm. When the difference between m_I and m_o is small (<0.1) the numerical solution provides a more accurate representation of the autocorrelation function.

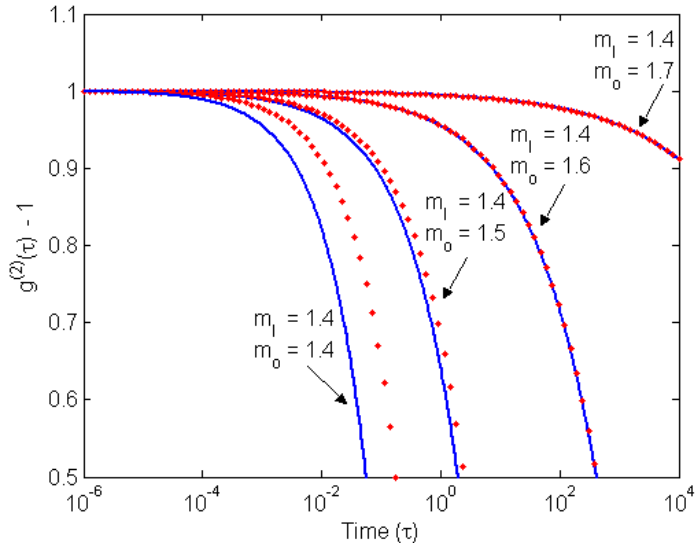

Fig. 5.2. Inverse Laplace transform of Eq. 5.25 from the approximated analytical expression (solid blue lines) and from the numerical algorithm (red dots). Outputs from different sets of m_I and m_O are indicated in the plot.

For samples with sufficiently large difference between m_{on} and m_{off}, one can

fit Eq. 5.28 to the measured autocorrelation function in order to extract the *on*- or *off*-time power exponent. Fig. 5.3 shows an example of the fit, for this particular sample the best fit is with the exponent m = 1.9, a larger m fails to fit the curvature of the autocorrelation function while a smaller m deviates from the autocorrelation function at the longer time delay tail.

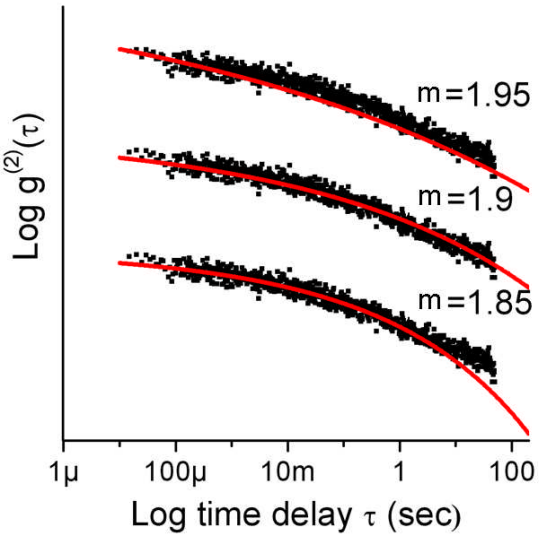

Fig. 5.3. An example of the analytical autocorrelation function fitting to experimental result.

On can see from Eq. 5.25 that θ and T_I are interrelated, if both are allowed to vary then a fixed set of fitting values can not be obtained. As discussed earlier, the short time cut-off, θ, can not be defined from experiment. The average *on*-time, T_I, is not well defined if the arbitrary cutoffs do not exist, therefore it will depend on the duration of the total measurement time. Nevertheless, the choice of θ/T_I or B will change where the curvature occurs but will not change the degree of the curvature. Plotting Eq. 5.28 with values of m ranging from 1 to 2 as shown in Fig. 5.4 provides a better illustration on the dependence of autocorrelation function with different m.

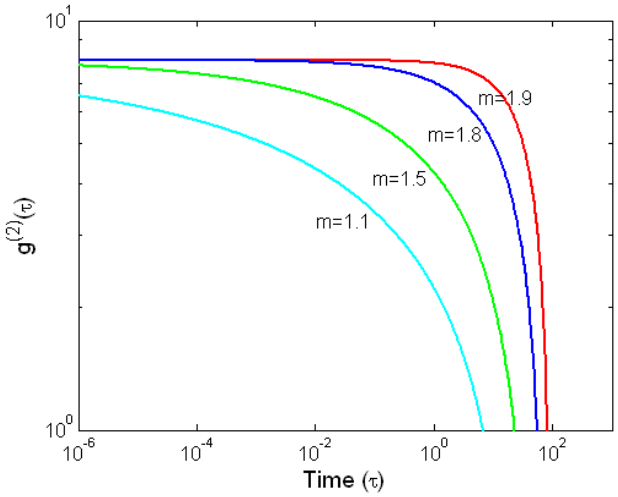

Fig. 5.4. A plot of Eq. 5.28 to show the effect of power law exponent, *m*, on the autocorrelation function.

We will now turn our attention to the different scenarios when the power law exponent may have changed at some time t_c. The average duration for an *on*- or *off*-event, T_I or T_O, will depend on the respective power law exponents. Therefore the shape and the relative magnitude of $g^{(2)}(\tau)$ before and after time τ_c will depend on $m_{on/off}$, $T_{I/O}$ and possibly $\theta_{mI/mO}$, hence the interpretation can be complicated. Nevertheless we can see qualitatively how the autocorrelation function can change if we plot Eq. 5.28 with different *m* for $\tau < \tau_c$ and $\tau > \tau_c$ whilst holding the variables A and B constant, then join them together in the y-axis arbitrarily. The time t_c when the change occurred is indicated by the vertical solid black line in each plot. We describe four different scenarios in Fig. 5.5. (a) If both m_I and m_O are large at $\tau > \tau_c$ and then one of the exponents changes to a smaller value at $\tau < \tau_c$ while the other exponent holds constant, the overall autocorrelation function will follow the unchanged larger exponent. Therefore the change in exponent can not be detected by the autocorrelation function. (b) If one of the exponents is larger than the other one at $\tau > \tau_c$, then the autocorrelation function will follow the larger exponent in this time regime. If then the larger exponent changed to a value less than the smaller exponent at $\tau < \tau_c$ then the autocorrelation function will follow the smaller exponent at this

shorter time regime. We may be able to notice this change of power law at time τ_c by inspecting the autocorrelation function. The change would seem more abrupt rather than a smooth curvature. In addition the short time regime will appear flatter and the long time regime will "decay" slower than what is expected from the flat short time regime. The change in the autocorrelation function can appear convex if m_I has changed. With a smaller m_I we will expect the average duration T_I to increase.From the numerical inverse Laplace transform, an increase in T_I will shift the curvature to a longer time delay, hence the autocorrelation will appear flatter in the short time regime. Although a change in power law exponent may be observed by inspection, whether or not we can extract this changed exponent depends on its magnitude compared to the unchanged exponent. (c) Similar to case (b) but the change in autocorrelation function can appear as concave if m_o has changed. With a smaller m_o we will expect the average duration T_O to increase. We can check how these change will affect the autocorrelation function by using the numerical inverse Laplace transform on the normalised $g^{(2)}(s)$. One will find the curvature of the autocorrelation function to "shift" towards shorter time and higher in y-axis, thus results in the red line as shown. This results in the concaved appearance of the overall autocorrelation. (d) Finally, if both exponents change at time $\tau_{c,}$ a change in autocorrelation may still be detected, however the shape of the autocorrelation may look similar to either (b) or (c) depending on the relative magnitude of the changed exponents. From the above discussion, we can expect to observe a change in autocorrelation function to some extent if the power law exponents have changed at some time τ_c. However, from the autocorrelation function alone, it may be difficult to determine which exponent has changed or to extract the magnitude of the changed exponent.

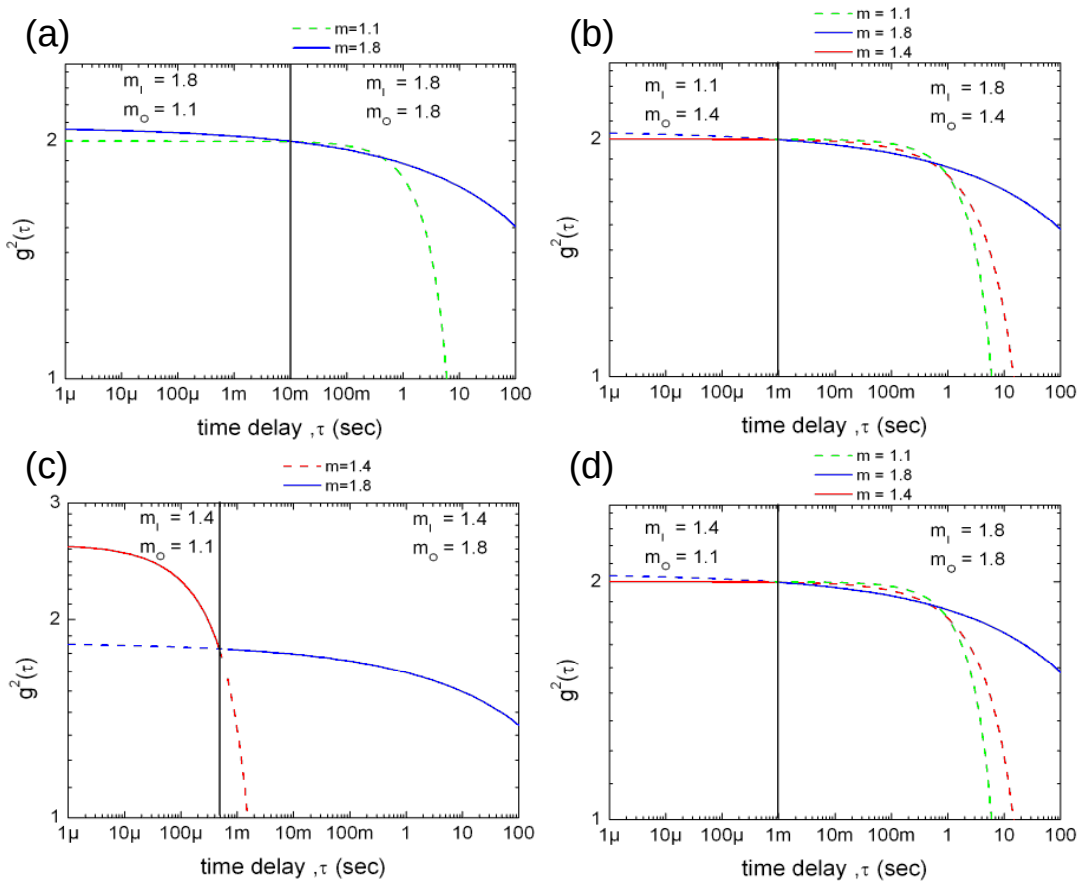

Fig. 5.5. Autocorrelation functions modelled by Eq. 5.28 to show the possible scenarios if the power law exponent has changes at some time τ_C. Autocorrelation functions with different power law exponents are joined together arbitrarily in y–axis at the point of change indicated by the vertical solid black line in each graph. Different line colour in the plot represent different $g^{(2)}(\tau)$ calculated from the power law exponents, m=1.8 (blue), m=1.4 (red) and m=1.1 (green) respectively. The solid colour lines represent the expected autocorrelation function due to the change of exponent, while the dashed colour lines represent the extension of the autocorrelation function with unchanged exponent. See text for detail.

If the photons are not correlated at long time scales we will expect an asymptotic value of one in $g^{(2)}(\tau)$ like in the case of uncorrelated random light shown Fig. 3.11 However, due to the finite probability at all time scales possessed by power law dynamics, the longer the total measurement time the more long on/off events will appear, thus we are expected to see roll offs starting at the time scale comparable to the total measurement time but not reaching the asymptotic value of one. In other words, the normalised peak at $g^{(2)}(0)$ depends on the total measurement time.

5.4 Combining $g^{(2)}$, TRPL and blinking data for single NCs

5.4.1 Bare NCs

The following data is measured using core only (bare) NCs purchased from Evident technology (nominal emission peak at 608 nm, lot no. MZP24DCC). These are CdSe core NCs with oleic acid as ligands around the NC. Some representative $g^{(2)}$ data with corresponding TRPL and blinking data for selected single NCs are shown below to illustrate the different dynamics. The TRPL decay data is processed by deleting the background counts as described in previous chapter, the original data is included for Evicore0831NC2 to show the difference, whereas only the background deleted TRPL decay is shown for the other NCs. Each nanocrystal is coded using the following rule,

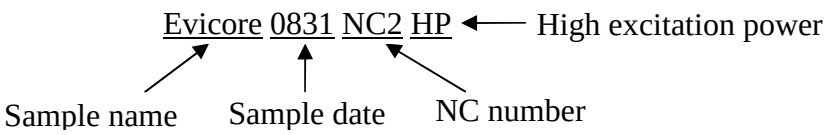

5.4.1.1 Evicore0831NC2

The original TRPL decay curve for this NC is shown as green dots in Fig. 5.7(a), the data from 100 ns to 500 ns clearly shows the tail of the TRPL fades into the background. As discussed in previous chapter, this background counts is subtracted from the decay (about 140 counts for this case) to reveal the true power law gradient on a log-log plot. The power law decay appeared as an asymptotic gradient at the tail of the TRPL, the red solid line is an 'apparent linear least-square fit' from Origin® to extract the power law exponent as m = -1.44. The autocorrelation function is shown in Fig. 5.7(b) with a minimum timing resolution of 5 μs. Switching to Fig. 5.7 (c) first, one can see there are two 'dips' in the intensity time trace at ~300 sec for ~20

sec and at ~500 sec for ~75 sec. These are experimental artifact caused by a redirection of the signal from the SPAD to an imaging mode CCD in order to check if the NC has moved out of focus or if it is dead. This action will not affect the TRPL data and the $g^{(2)}$ data at short time delays, but it will influence the $g^{(2)}$ data at a longer time delay, particularly when $\tau \approx 20$ and 75 sec, for example, the long time correlation does decay to a value below one when $\tau > 10$ sec. Therefore the analytical $g^{(2)}$ function is only fitted to the data for $\tau < 10$ sec, and a power law exponent of $m = 1.47$ is extracted. To proof this argument, we randomly generated two time series with an arbitrarily introduced period that has a lowered count rate as shown in **Fig.** 5.6, we then plot the calculated autocorrelation function for each time series. As one can see the "curvature" due to the introduced lower counts begins at a time that corresponds to the duration of the arbitrary period. At a time delay shorter than the induced period, $g^{(2)}$ is shifted up in y-axis by an arbitrary constant, however its shape is not changed. Also noted from the simulation that $g^{(2)}$ has dropped to a value below one for the time series with a longer "dark" time.

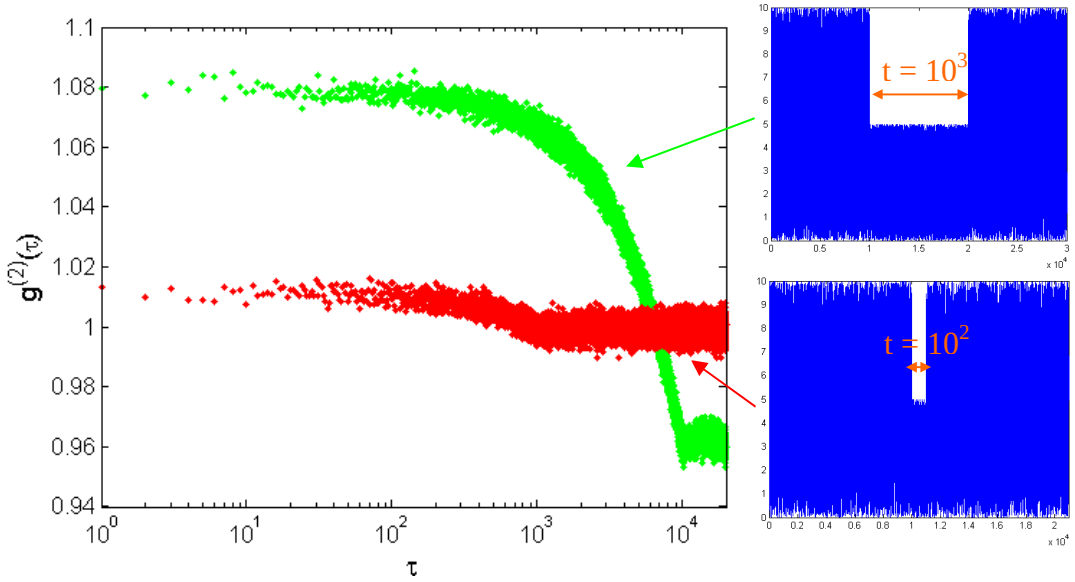

Fig. 5.6. Autocorrelation function calculated from two randomly generated time series. The "higher" and "lower" counts in each time series is generated by multiplying a random number between 0 and 1 by a factor of ten and five respectively. The duration of the lower counts is set to 10^3 and 10^2 unit times respectively

By setting a threshold value indicated by the dash red line shown in Fig. 5.7(c), the on- and off-time power law exponents are found to be αoff = 1.27 and αon = 1.58. Since αon is larger than αoff therefore the power law exponent extracted from g(2) data should represent the on-time statistics. Finally mg2 and αon does match up within experimental errors.

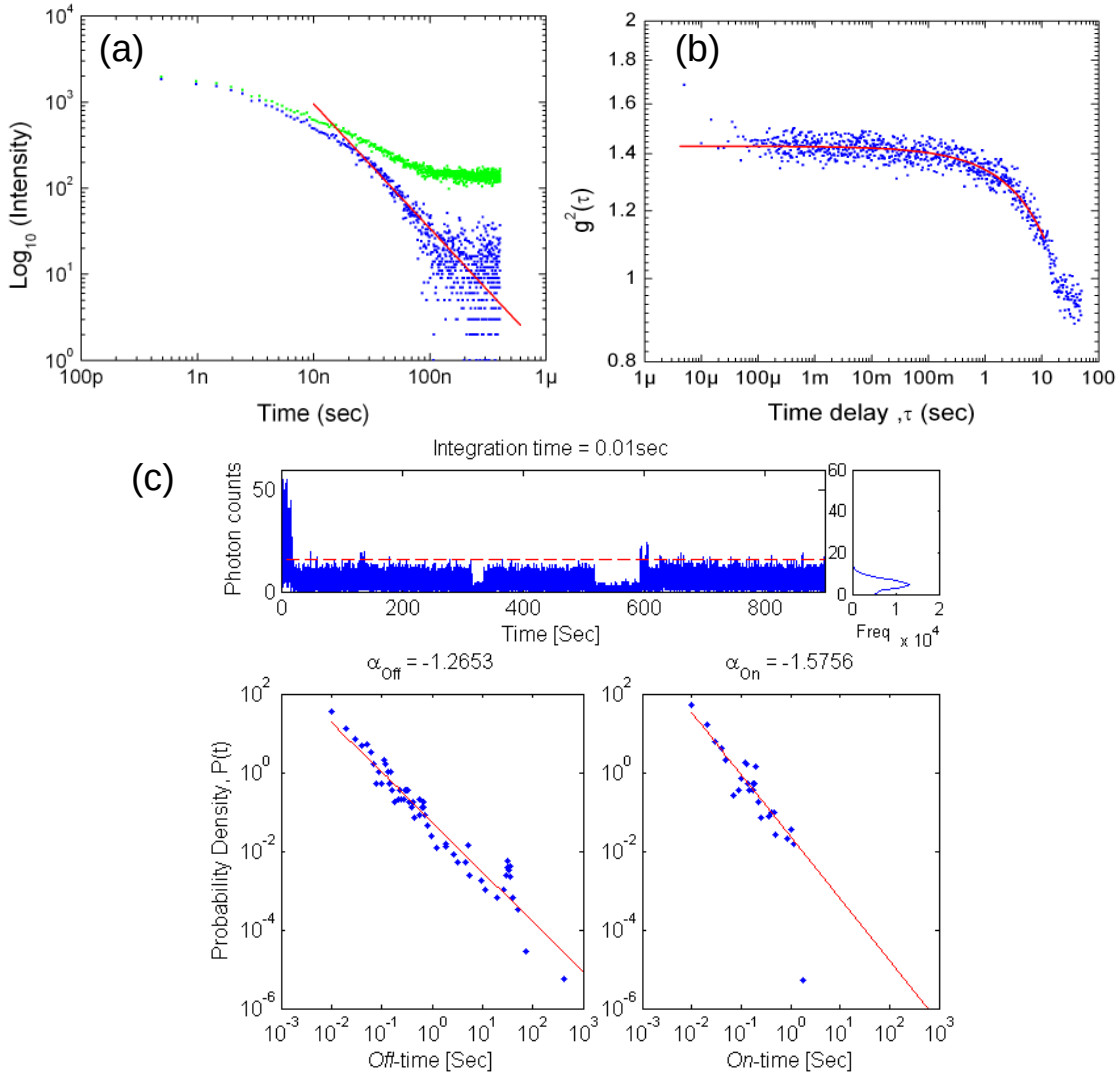

Fig. 5.7. (a) TRPL decay curve of the single NC, original data (green), and background deleted (blue). Red solid line is a linear fit to the tail of the TRPL with a gradient = -1.44. (b) Autocorrelation function of the same NC (blue). Red solid line is a theoretical fit to extract the power law exponent, *m* = 1.47. (c) Blinking statistics extracted from the intensity time trace at the threshold level set by the red dash line.

5.4.1.2 Evicore0831NC3

Fig. 5.8(a) shows the TRPL decay with a power law gradient of -1.23. Auto-correlation function is shown in Fig. 5.8(b) with a minimum resolution of 5 μs (blue dots). The reason why the 5 μs data point ($g^{(2)} \approx 1.4$) is slightly above all other data points is most likely due to the SPAD after pulse effect. Meanwhile, the same correlation function but with the raw data binned at 500 μs (green dots) reveals that the correlation after $\tau = 10$ sec is mostly due to background noise since it fluctuates near $g^{(2)} = 1$, thus the fitting does not include these points. A power law exponent of $m = 1.82$ is extracted from the $g^{(2)}$ data. Moreover, the flat tail of the autocorrelation at $\tau > 10$ suggested that there is no switching between *on*- and *off*-state at a time scale above 10 sec. In other words the *off*-events can last longer than 10 sec but *on*-events will be shorter than that. If we turn to the intensity time trace, a low average intensity that holds constant over a period longer than 10 sec is probably noise, i.e. NC is off. This helped us to select a seemly higher threshold level from the multileveled intensity time trace shown in Fig. 5.8(c). The exponents are found to be $\alpha_{off} = 1.58$ and $\alpha_{on} = 2.02$. The *on*-time probability distribution appears to roll-off from a power law at longer times or at the tail, however the limited data points render it difficult to justify where exactly the roll-off starts. Nevertheless the power law exponent extracted from the autocorrelation will again represent the *on*-time power law.

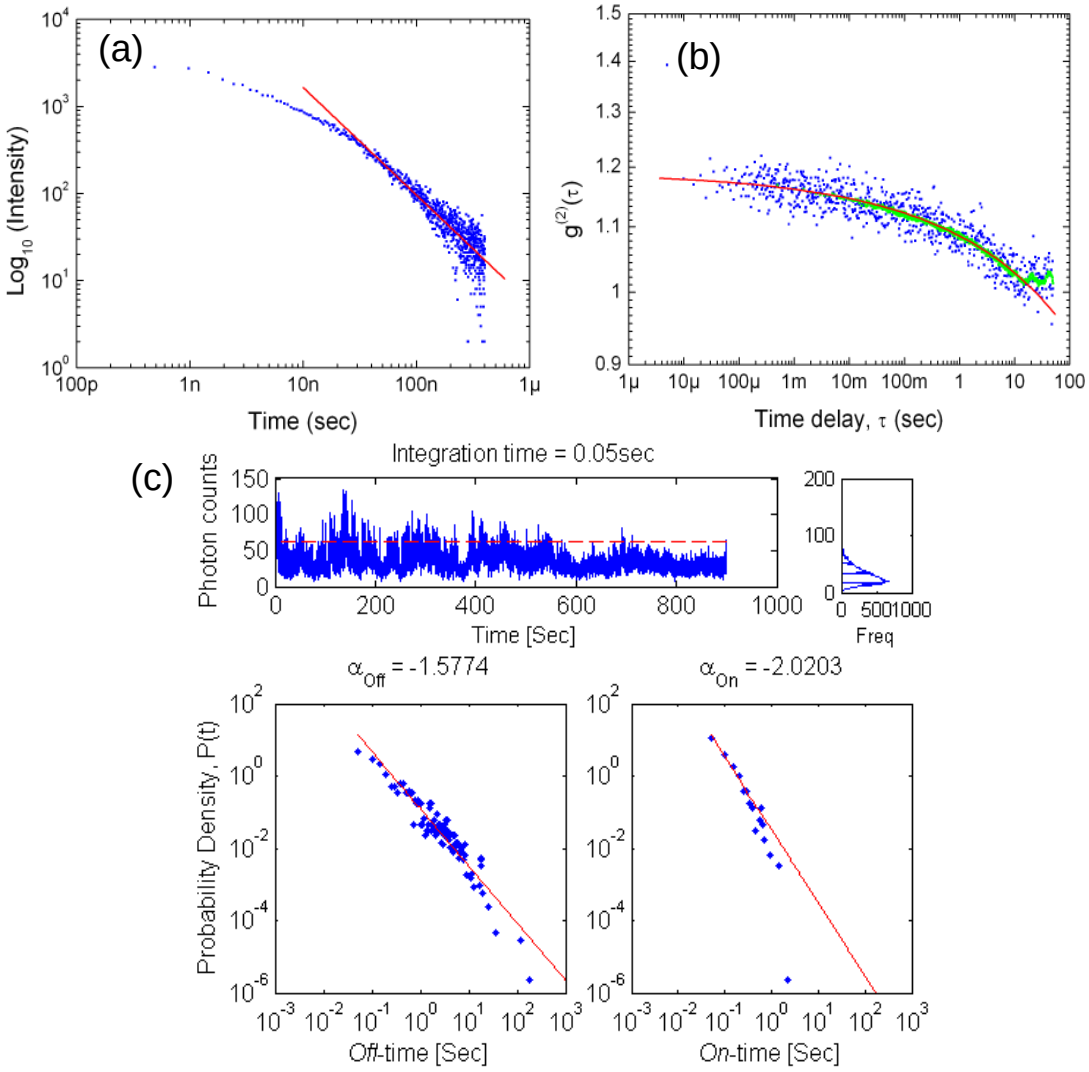

Fig. 5.8. (a) Background corrected TRPL decay curve of the single NC (blue). The Red solid line is a linear fit of the TRPL tail with a gradient = -1.23. (b) Autocorrelation function of the same NC ((blue, 5μs bin time; green, 500μs bin time). Red solid line is a theoretical fit to extract the power law exponent, *m* = 1.82. (c) Blinking statistics extracted from the intensity time trace at the threshold level set by the red dash line.

5.4.1.3 Evicore0225NC3

The TRPL decay in Fig. 5.9(a) gives a power law exponent of -1.35. The autocorrelation function again suggests no correlation at a time delay above τ = 2 sec, this is also supported by the long off-events and short spike on-events from the intensity time trace shown in Fig. 5.9(c). The peak at time delay below τ = 100 μs cannot be due to SPAD afterpulse since it is very unlikely the defects in silicon detector that causes afterpulsing would have such a long lifetime. However it is not

clear at this stage whether this phenomenon is an experimental artifact or genuine thus it is omitted in the analytical fitting. The fitting in the range from 100 μs to 2 sec shows a power law exponent of 1.87. Blinking statistics suggest a power law exponent of α_{off} = 1.31 and α_{on} = 1.88.

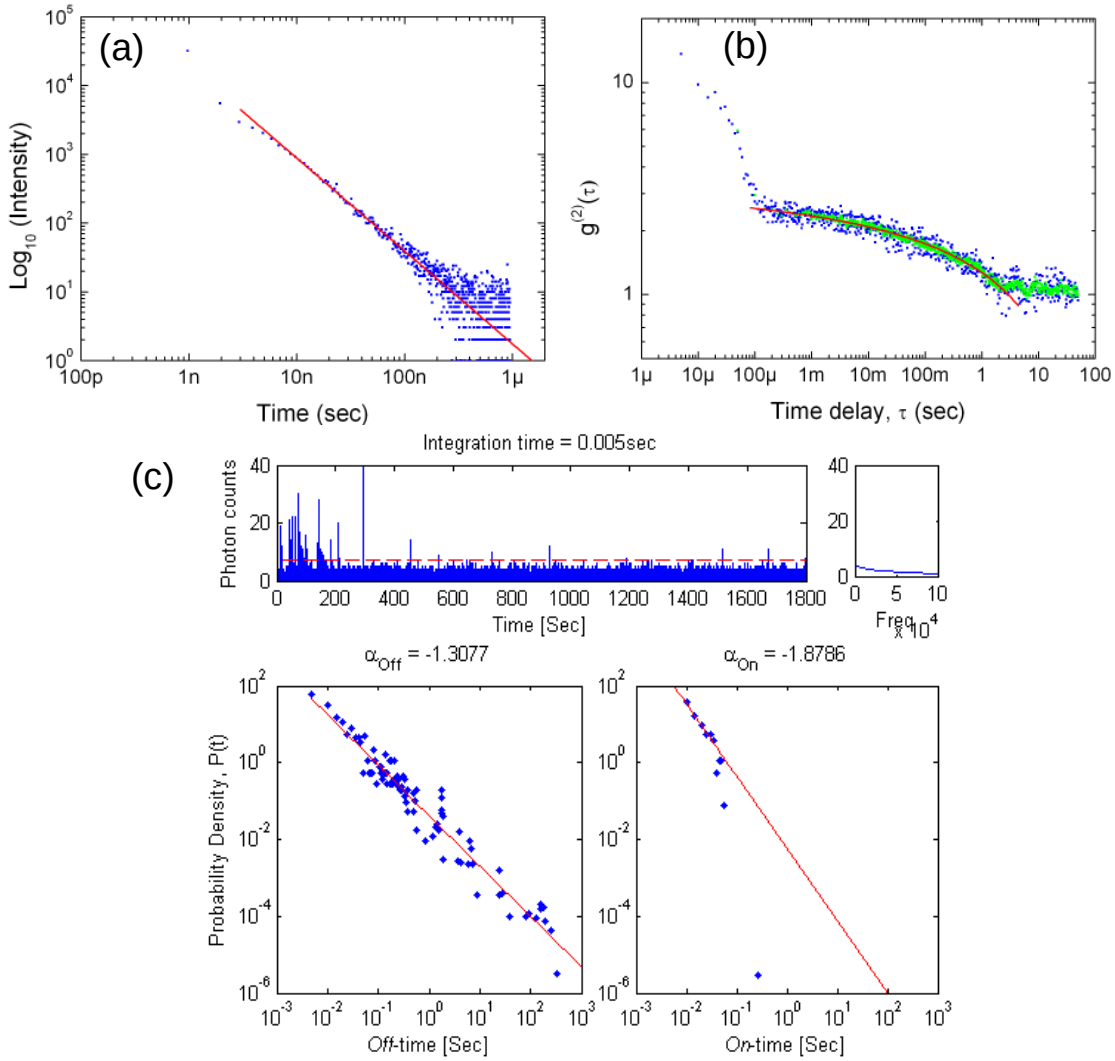

Fig. 5.9. (a) Background corrected TRPL decay curve of the single NC (blue). The Red solid line is a linear fit to the tail of the TRPL with a gradient = -1.35. (b) Autocorrelation function of the same NC (blue, 5μs bin time; green, 50μs bin time). Red solid line is a theoretical fit used to extract the power law exponent, *m* = 1.87. (c) Blinking statistics extracted from the intensity time trace at the threshold level set by the red dash line.

5.4.1.4 Evicore0225NC1

The TRPL decay in Fig. 5.10(a) gives a power law exponent of -1.35. The $g^{(2)}$ data for this particular NC appears to be linear, fitting a straight line gives a gradient of -0.04, from Eq. 5.26 this translates into a power law exponent of 1.96. Eq. 5.26 assumes a single exponential *on*-time thus the extracted exponent should represent the *off*-time statistics. Although it is difficult to justify from the limited data points whether the *on*-time statistics follows a power law or a single exponential, the *off*-time exponent, α_{off} = -1.19, is in contrast to the value obtained from $g^{(2)}$ with a linear fit. In addition, from all the NCs measured within this sample, this particular NC shows a more linear-like autocorrelation function. The general trend over the other NCs have shown a power law distributed *on*- and *off*-times, therefore Eq. 5.28 is chosen again to fit the $g^{(2)}$ data. The 50 μs binned $g^{(2)}$ data (Fig. 5.10(b), green) revealed an unusual rise in the correlation after τ >1, this is caused by the artificial dip in the intensity time trace (~380 sec) as discussed in section 5.4.1.1. Therefore the $g^{(2)}$ data is only fitted up to τ < 1 and the power law exponent shown to be 1.99, in good agreement to α_{on}.

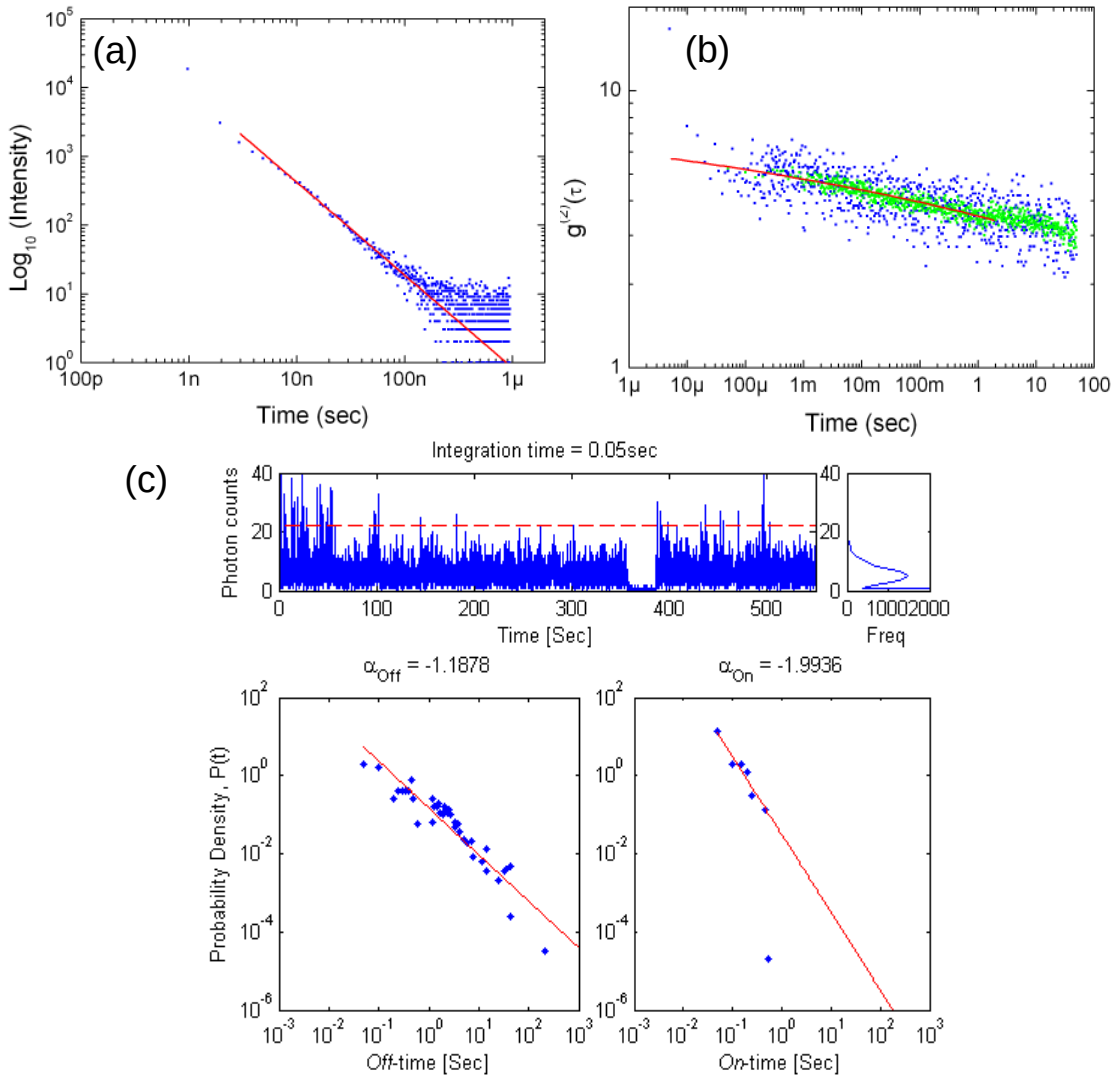

Fig. 5.10. (a) Background deleted TRPL decay curve of the single NC (blue). Red solid line is a linear fit to the tail of the TRPL with a gradient = -1.35. (b) Autocorrelation function of the same NC (blue: 5μs bin time; green: 50μs bin time). Red solid line is a theoretical fit to extract the power law exponent, m = 1.99. (c) Blinking statistics extracted from the intensity time trace at the threshold level set by the red dash line.

5.4.1.5 A summary of the Evicore single NCs observed

A summary of all the NCs observed from this sample (Evident Tech., core only) is shown in Table 5.1. For all the NCs observed, the blinking *on*-time power law exponents are greater than the *off*-time exponents, hence the exponents extracted from autocorrelation functions are all assigned to m_{on}. Comparing m_{on} and α_{on} ,one can observe a close correlation suggesting the *on*-time power law statistics is continuous and unchanged over the time range from 5 μs to 1 sec. Since we do not

obtain the *off*-time power law exponents from the autocorrelation analysis, the time gap between TRPL and blinking *off*-statistics can not be joined up directly. However the autocorrelation analysis suggests that both the *on*-time and *off*-time statistics are power law distributs and a good correlation exists between m_{on} and α_{on} which points to the fact that $m_{off} < m_{on,}$ thus it is plausible that m_{off} is also continuous and unchanging.

Table 5.1. Summary of single NC power law exponents extracted from the sample Evicore

	TRPL (10ns-1μs)	$g^{(2)}$ (5μs-10s)		Blinking (50ms-100s)	
	m_{off}	m_{on}	m_{off}	α_{on}	α_{off}
0225NC1	1.35	1.99	-	1.99	1.19
0225NC2	1.43	1.98	-	2.02	1.11
0225NC3	1.35	1.87	-	1.88	1.31
0225NC4	1.27	1.97	-	2.16	1.09
0831NC1	1.61	1.71	-	1.77	1.34
0831NC2	1.47	1.44	-	1.58	1.27
0831NC3	1.23	1.81	-	2.02	1.58
0831NC5	1.30	1.71	-	1.77	1.51
0831NC6	1.07	1.88	-	1.83	1.74
0831NC7	1.31	1.85	-	1.91	1.51

The four TRPL decay curves shown in Fig. 5.11 are from (1) an ensemble made from the original solution purchased from Evident Tech. (green), (2) an ensemble diluted to 1.2k:1 (Cyan), (3) an ensemble diluted to 13k:1 (Blue), (4) and a single NC from a sample diluted to 250k:1 (purple). The two diluted ensembles give a similar power law gradient, where the 1.2k:1 sample allows us to measure decay to a longer delay due to the higher signal count rate. However the ensemble sample made from the concentrated original solution gives a higher power law exponent, we may justify this by considering the relative distance between nanocrystals. For the single NC sample, the average distance between NCs as seen from the spectrograph in image mode is about 2 μm, hence by considering the difference in concentration,

the average distance between NCs for the ensembles is estimated to be 500 nm (13k:1), 200nm (1.2k:1), and 5 nm (1:1) respectively. When the NCs are well separated, the ejected carrier can be argued to stay in the vicinity of the NC or trapped by the trap site near the NC, therefore the interrelation between adjacent blinking NCs is low. However when the NCs are closely packed, as for the 1:1 sample, the ejected carrier may well be captured by the adjacent NC therefore forcing it to switch to an *on*- or *off*-state depending on its carrier configuration before the intrusion of the foreign carrier. In other words, one blinking NC will increase the probability for a neighbouring NC to blink as well and the effect may continue to spread to other NCs, hence the overall blinking activity of the ensemble will increase thus we see an increase in the power law exponent. A similar blinking enhancement is reported by Yu et al.[63] From a NC cluster formed by two single NCs sticking together, they have observed a higher blinking frequency, however the enhancement is not observed when single NCs are few tens of nanometres apart.

We will expect the power law exponent from the ensembles to represent the expected exponents for single NCs, however most of the exponents we obtained from single NCs tend to be smaller then the ensemble value. This can be argued by the limited single NC samples measured or it could be the fact that we are selectively picking only the dimmer and blinking NCs, thus producing higher long off-time probabilities and lower short off-time probabilities and hence smaller exponent, to be sure it is a single NCs.

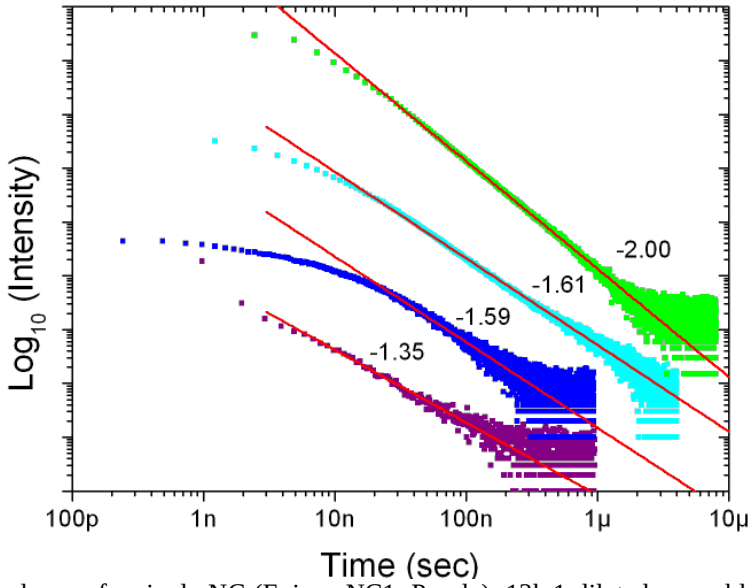

Fig. 5.11. TRPL decay of a single NC (EvicoreNC1, Purple), 13k:1 diluted ensemble (Blue), 1.2k:1 diluted ensemble (Cyan), and 1:1 ensemble(Green). Red solid line is a linear fit to the tail of the decay; corresponding gradient is shown to the right of the data. See text for detail.

5.4.2 Core/Shell NCs

CdSe/ZnS core/shell NCs were purchased from Evident technology®. Evi600 is a newer sample that emits at 600 nm and the core composition is similar to the Evicore sample described above. Evi620 is an older sample that emits at 620 nm, the core contains a small amount of Zinc that act as an alloying agent. The shell for both samples in terms of anneal and growth times, passivating ligands, and thickness are the same. Two typical data sets are described below.

5.4.2.1 Evi600 1016NC14

The Evi600 sample are well passivated NCs as indicated by the high fluorescence intensity and the binary on/off states. However the good passivation means the trapping rates will be low therefore the TRPL data in the nanosecond regime is dominated by the radiative decay. In fact, a single exponential fits the TRPL decay nicely with a lifetime of 19.6 ns. This is in good agreement with the published fluorescence lifetime[64]. Unfortunately this poses some difficulty in extracting the

off-time power law exponent from the single NC TRPL decay. In fact, the ensemble data shown in Fig. 5.14 show the power law component only become apparent after 300 ns. In this time regime the single NC TRPL is dominated by background noise. However, considering all the other types of samples measured, a good correlation is found between the power law exponents obtained from the TRPL of all the ensemble and a single NC, thus we may safely regard the exponent extracted from the ensemble as the expected exponent value for the majority of single NCs found in this sample. From the intensity frequency distribution of Fig. 5.12(c), there is a distinct features to distinguish between *on* and *off* states, therefore there is less ambiguity in the choice of the threshold limit and hence a smaller error bar in the extract power law exponents. The *off*-time power law has a large exponent of 2.0 whilst the *on*-time power law has a smaller exponent of 1.1. The exponential roll off for the *on*-time statistics appears to start at ~200 ms. The red solid line in Fig. 5.12(b) is an analytical fit to the whole set of autocorrelation data with an extracted exponent of 1.9, however the fit is not satisfactory as it over estimates in the short time regime and does not describe the curvature of the data accurately. We then divide the autocorrelation into two time regimes, set by the onset of the *on*-time exponential roll off at ~200ms (solid black line). The green line is a linear fit in the long time regime and the extracted exponent is 1.96, in good agreement with the blinking *off*-time power law exponent. The orange line illustrates an analytical fit in the short time regime with an extracted exponent of 1.62. This figure is much larger than the blinking *on*-time exponent, therefore it must represent the *off*-time power law rather than *on*-time power law in this time regime. However we can not extract the small *off*-time exponent of 1.21 from the autocorrelation function since an exponent of 1.6 or 1.2 will appear similarly flat at a short time regime (~ 1 μs to 100μs) as shown in

the model curves of Fig. 5.5. In addition, this figure is an intermediate value between the large blinking *off*-time exponent (2.0) and the small *off*-time exponent from ensemble TRPL (1.21) suggesting a slow gradual change in the *off*-time exponent over the time regime of the curvature, i.e. around 1 ms to 200 ms.

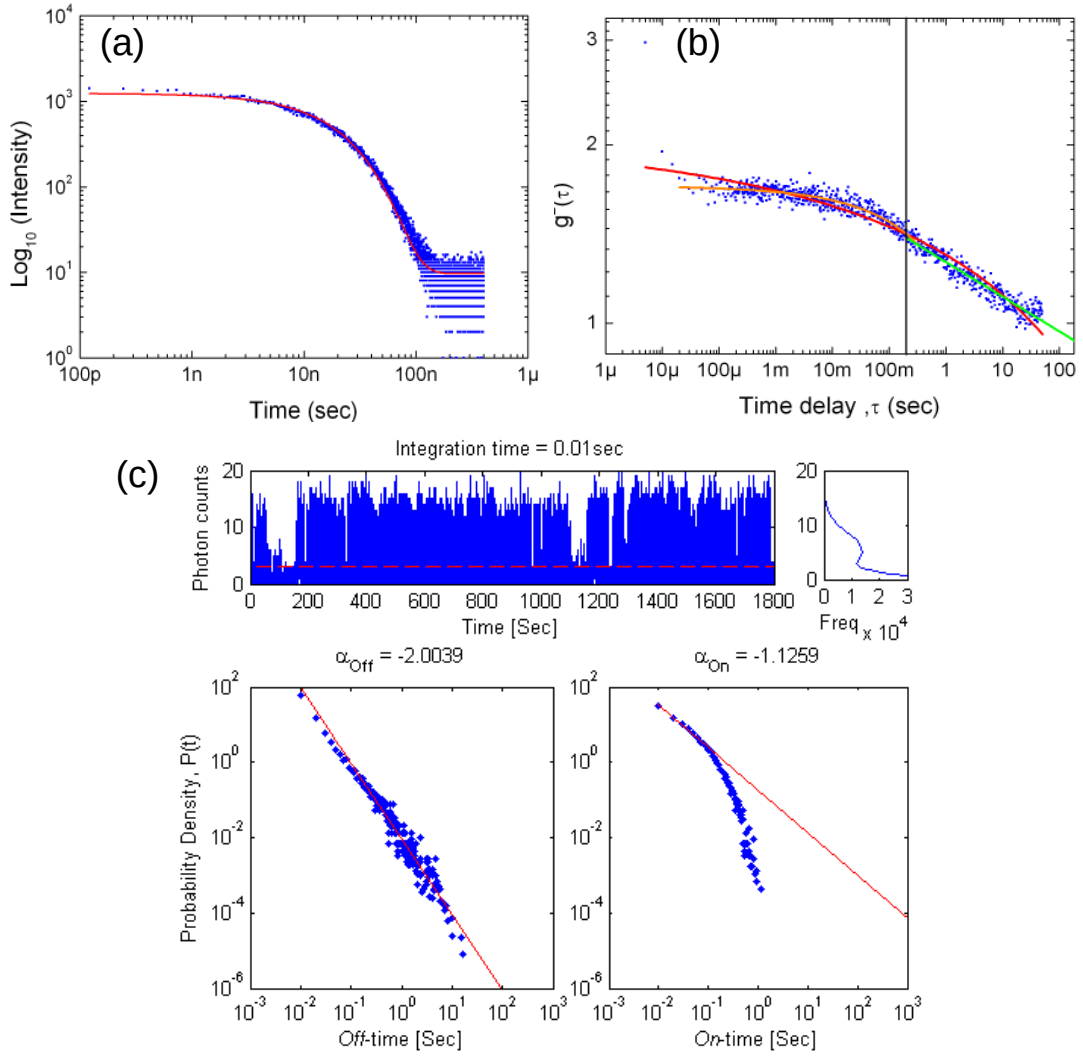

Fig. 5.12. (a) TRPL decay curve for this core/shell single NC. Red solid line is a single exponential fit that gives decay lifetime of 19.6 ns. (b) Autocorrelation data with a time resolution of 5 μs (blue dots). Red solid line is an analytical fit to the whole data set. Black solid line represents where the on-time exponential roll off appears to begin. Orange solid line is an analytical fit to the shorter time regime, the extracted exponent is 1.62. Green solid line is a linear fit to the longer time regime, the extracted exponent is 1.96. (c) Blinking statistics extracted from the intensity time trace at the threshold level set by the red dash line. A clear binary on/off state can be observed from the two peaks of the frequency distribution.

5.4.2.2 Evi600 1016NC16

Similar to Evi600 1016NC14 the single NC TRPL is dominated by the fluorescence decay, a single exponential fit to the data gives a lifetime of 12.7 ns. We again observe a distinct *on*- and *off*-state such that the valley in the intensity frequency distribution may be used to set a threshold with less ambiguity. The large *off*-time exponent (2.2) and a small *on*-time exponent (1.4) is similar to Evi600 1016NC14. An analytical fit to the autocorrelation data as illustrated by the solid red line in Fig. 5.13(b) extracts an exponent of 1.74. The small misfit at longer time delays is argued to be due to the exponential roll off of *on*-time. A similar but slightly smaller exponent of 1.66 is extracted if we set a time division like in Evi600 1016NC14. Following the same argument as above, the data suggests a slow gradual change in the *off*-time power law but this change is suggested to occur over a longer time period (1 ms to 1 s). It is uncertain why the change in power law is not observed in the blinking *off*-time statistics, a suggest reason for this be due to the limited timing resolution and the limited statistical data.

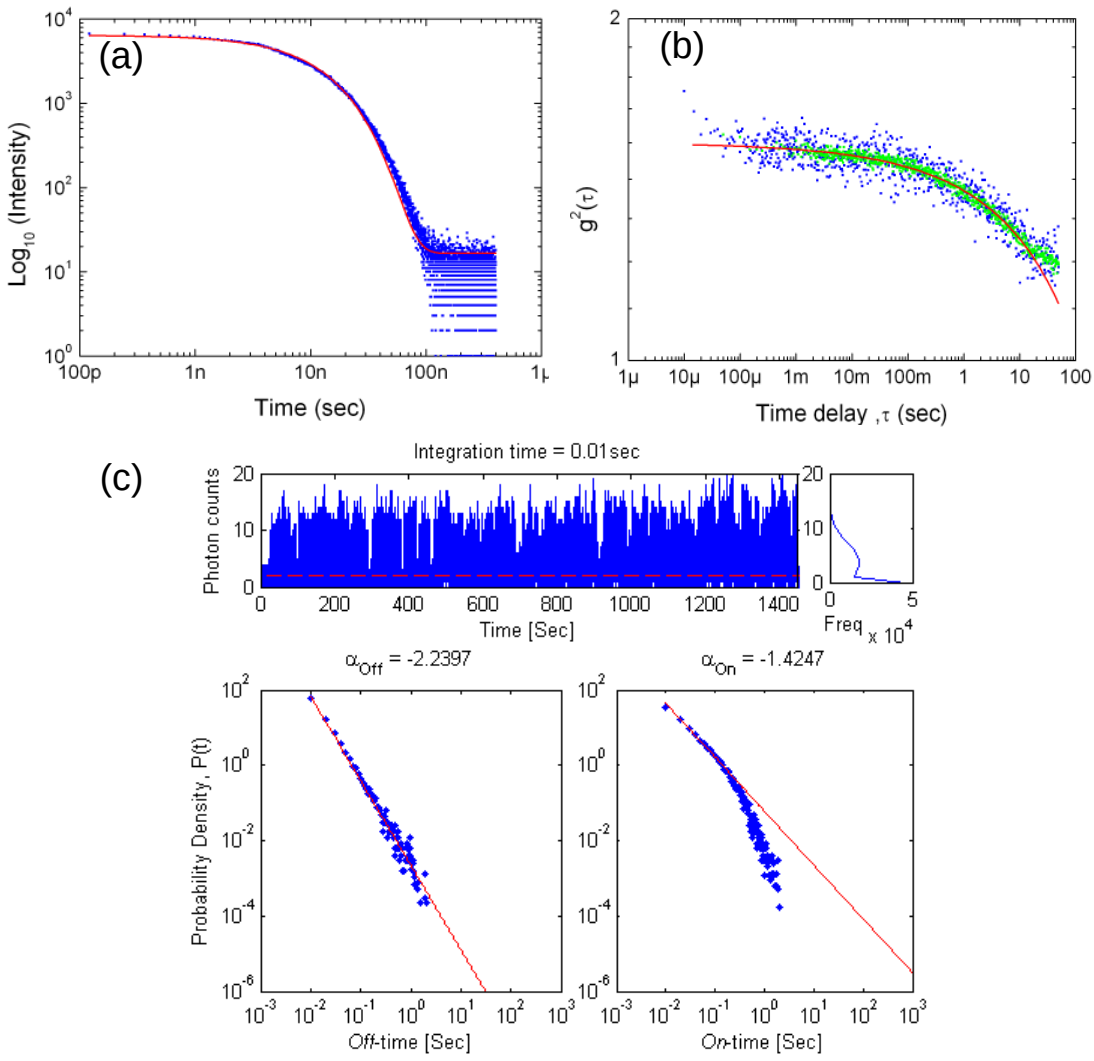

Fig. 5.13. (a) TRPL decay curve for this core/shell single NC. Red solid line is a single exponential fit that gives decay lifetime of 12.7 ns. (b) Autocorrelation function of the same NC (blue: 5μs bin time; green: 50μs bin time). Red solid line is an analytical fit to the whole data set that gives an extracted exponent of 1.74. (c) Blinking statistics extracted from the intensity time trace at the threshold level set by the red dash line. A clear binary on/off state can be observed from the two peaks of the frequency distribution.

5.4.2.3 A summary of the Evi600 single NCs observed

As shown by all, the characteristic power law in single NC TRPL tail is not obvious, however, as suggested from the ensemble measurement, the expected value for the *off*-time exponent in this time regime can be regarded as 1.21. The blinking statistics suggest a large off-time power law exponent in the time regime from milliseconds to seconds with an average value of ~2, moreover the *on*-time power law exponent is

small and the average value is ~1.2. This is in contrast with core only NCs where the power law exponents extracted from autocorrelation functions is larger than the corresponding *on*-time exponents therefore all of then are assigned to m_{off}. The value of the autocorrelation m_{off} exponents is an intermediate figure between the extracted from TRPL and blinking exponent, combining the *off*-time power law exponents measured at the three different time regimes provides an evidence for a change in the off-time exponents. The single NC analysis suggests a slow and gradual change in the time regime of about 1 ms to 100 ms.

Table 5.2. Summary of single NC power law exponents extracted from the sample Evi600

	TRPL (10ns-1μs)	$g^{(2)}$ (5μs-10s)		Blinking (50ms-100s)	
	m_{off}	m_{on}	m_{off}	α_{on}	α_{off}
1015NC9		-	1.68	1.20	2.22
1015NC10		-	1.75	1.15	2.45
1015NC10HP		-	1.83	1.29	1.96
1015NC11		-	1.75	1.52	1.99
1015NC12		-	1.76	1.02	1.79
1016NC13		-	1.71	1.01	2.06
1016NC14		-	1.62	1.13	2.00
1016NC15		-	1.71	1.58	1.95
1016NC16	1.21	-	1.74	1.43	2.24
1016NC17		-	1.75	1.01	1.87
1017NC18		-	1.78	1.20	1.92
1017NC19		-	1.95	1.36	2.19
1017NC19HP		-	1.91	1.39	2.21
1017NC20		-	1.67	1.54	2.14
1017NC21		-	1.86	1.22	2.55
1017NC21HP		-	1.74	1.11	1.80
1022NC22		-	1.75	1.39	1.84

The TRPL data for the Evi600 ensemble sample is shown in Fig. 5.16. The green dots represent an ensemble measured with settings of, TAC window = 5μs, pulse frequency = 250kHz, and stop (signal) rate = 12.5kHz. The same ensemble is measured again (orange dots) with settings of, TAC window = 10μs, pulse frequency = 125kHz, and stop (signal) rate = 6kHz. Care must be taken when correcting the

background counts since the the TRPL tail is still at a gradient rather than a flat background, i.e. one cannot simply regard the end time intensity as background counts. We estimate the background counts by using the fact that different TAC window should give us the same TRPL but only with a different resolution. Therefore the ensemble represented by green dots is scaled in y-axis by a factor of 2 so that its peak coincide with the orange ensemble. The offset at the tail of the TRPL between green ensemble and orange ensemble is a contribution of the background counts. The offset is found to be about 80 counts, therefore the background counts is estimated to be 80/2 = 40 counts. A separate control sample with no NCs was taken for 45 minutes and acquired a background count of 10. The ensemble TRPL is acquired over a period of 180 minutes, hence a similar estimation of 40 counts contributed from the background. The background corrected TRPL is illustrated by blue dots and the tail gives a power law exponent of 1.21. We note that in the shorter time regime the TRPL is dominated by the single exponential fluorescence decay with a lifetime of 23.5 ns, the onset of the power law only begins at about 300 ns. This strong exponential component is due to well passivation and high quantum yield of the NCs, however it also posses difficulty in extracting the power law exponent from the tail of the single NC TRPL. Nevertheless the ensemble result tells us that the majority of the single NCs will have a power law exponent of about 1.2 on average at this time regime. Comparing this to the average blinking *off*-time exponents and considering the indication of a change in exponent from the autocorrelation functions, this data suggested a change of the *off*-time exponent for the majority of NCs in this particular sample.

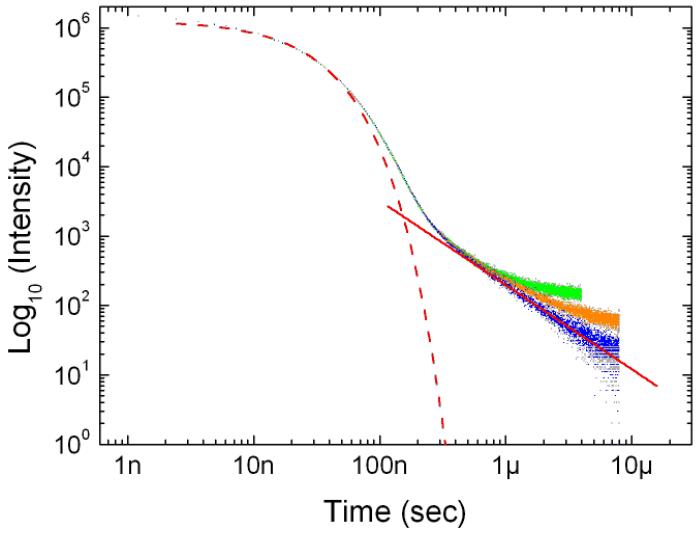

120

Fig. 5.14. TRPL decay measured from an ensemble of Evi600 NC sample. Green dots are not corrected for background and is measured with a TAC window of 5 μs. The orange dots are measured with a TAC windows of 10 μs and is background uncorrected while the background corrected data are represented by blue dots. Red solid line is a linear fit to the tail of the TRPL and corresponds to a gradient of 1.21. Red dashed line is a single exponential fit to the TRPL decay and gives a fluorescence lifetime of 23.5 ns.

5.4.2.4 Evi620 0812NC1

We now turn attention to the 620 nm emitters. This NC is a typical example for the few NCs measured for this sample. A linear fit to the tail of the TRPL gives a power law exponent of 1.54 in the nanosecond regime. Fig. 5.15(b) illustrates an attempt to fit the autocorrelation data with the analytical expression, this shows a power law exponent of 1.99. However it is clearly a poor fit as it overshoots the flat region in the short time regime and does not fit the curvature of the data. From the *on*-time blinking data one can observe an exponential roll off from the power law starting at about 100 ms. If we use that to divide the autocorrelation into two time regimes then fit the shorter time regime with the analytical function and the longer time regime with a linear gradient we can extract a power law exponent of 1.62 in the short time regime and 1.87 in the long time regime. The exponent of 1.62 from the short time regime fits well with the exponent extracted from TRPL and *off*-time statistics. The exponent of 1.87 from long time regime is larger than the *off*-time exponent, we

argue that it is due to the *on*-time roll off is not a pure single exponential. Combining the three different measurements, we can suggest a constant *off*-time power law exponent down to 20 ns but it is uncertain whether there is any change in the *on*-time exponent at the time regime shorter than the blinking statistics.

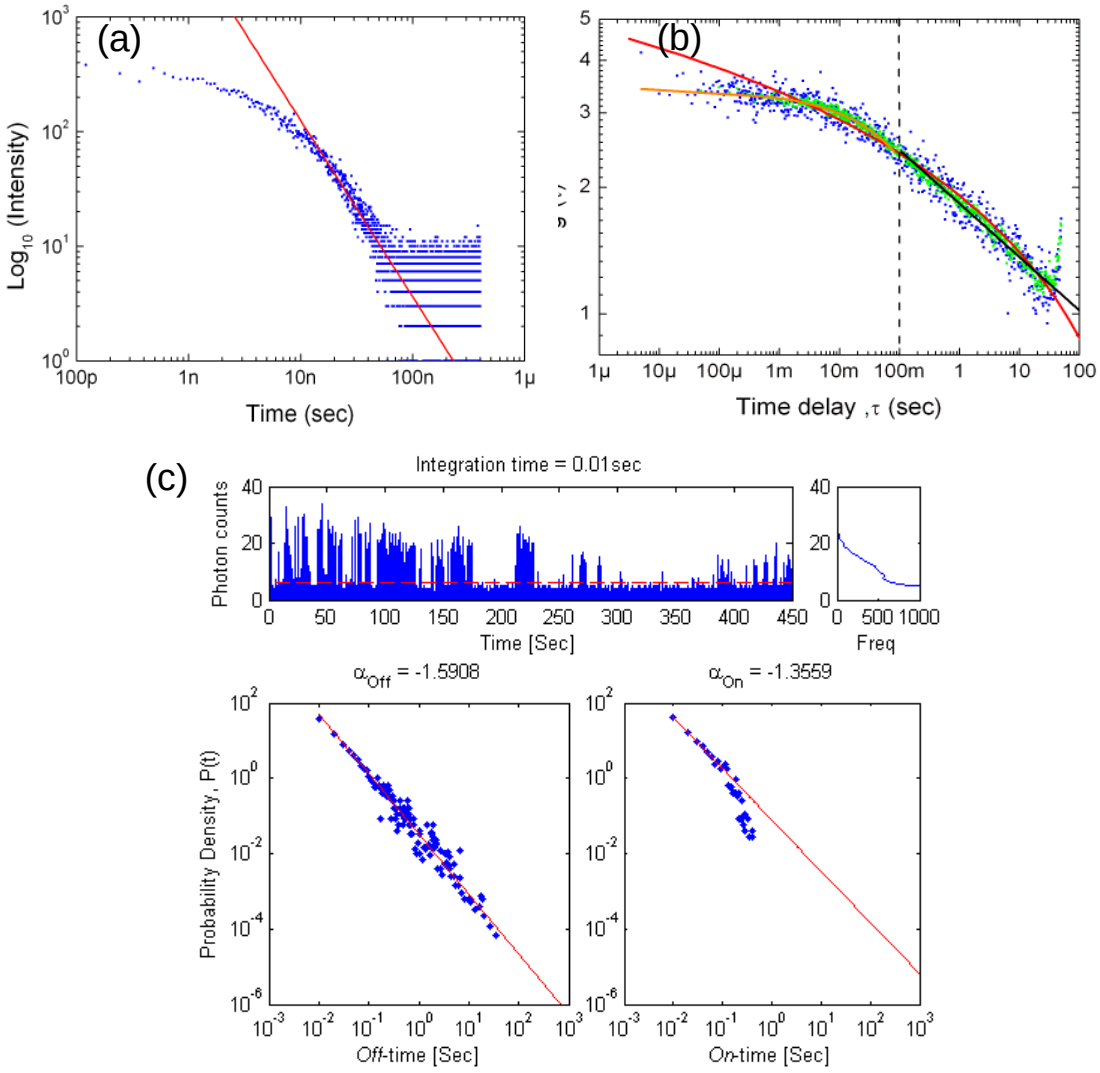

Fig. 5.15. (a) Background corrected TRPL decay curve of the single NC (blue). Red solid line is a linear fit to the tail of the TRPL with a gradient = -1.54. (b) Autocorrelation function of the same NC (blue: 5μs bin time; green: 50μs bin time). Red solid line is a theoretical fit to the whole data set. Black dash line represent where the blinking *on*-time appeared to tail off from the power law (~100ms). Orange solid line is an analytical fit to the shorter time regime to extract a power law exponent of 1.62. Black solid line is a linear fit to extract the power law exponent of 1.88(c) Blinking statistics extracted from the intensity time trace at the threshold level set by the red dash line.

5.4.2.5 A Summary of the Evi620 single NCs observed

The ensemble TRPL shown in Fig. 5.16 fades into a flat background at the tail of the TRPL (green dots). The background corrected TRPL is illustrated by blue dots where a fit to the tail gives a power law exponent of 1.81 (red solid line). In shorter time regime (t < 100ns) the TRPL is still dominated by the single exponential lifetime as a signature of the well passivation and high quantum yield of core/shell NCs. However the 1.81 power law exponent extracted from the ensemble TRPL fits well with the average blinking *off*-time exponents suggesting the power law is held constant over the time range measured. The power law exponent from TRPL for 0827NC6 is not extracted since the data is dominated by the fluorescence decay.

Table 5.3. Summary of single NC power law exponents extracted from the sample Evi620

	TRPL (10ns-1μs)	$g^{(2)}$ (5μs-10s)		Blinking (50ms-100s)	
	m_{off}	m_{on}	m_{off}	α_{on}	α_{off}
0812NC1	1.54	-	1.62	1.36	1.59
0812NC2	1.36	1.95	-	1.90	1.45
0827NC3	1.76	-	1.73	1.45	1.73
0827NC4	1.70	-	1.83	1.55	1.88
0827NC5	1.82	-	1.69	1.53	2.13
0827NC6	-	-	1.63	1.50	1.74
0827NC7	1.88	-	1.91	-	1.84
0827NC8	1.86	-	1.72	1.60	1.87

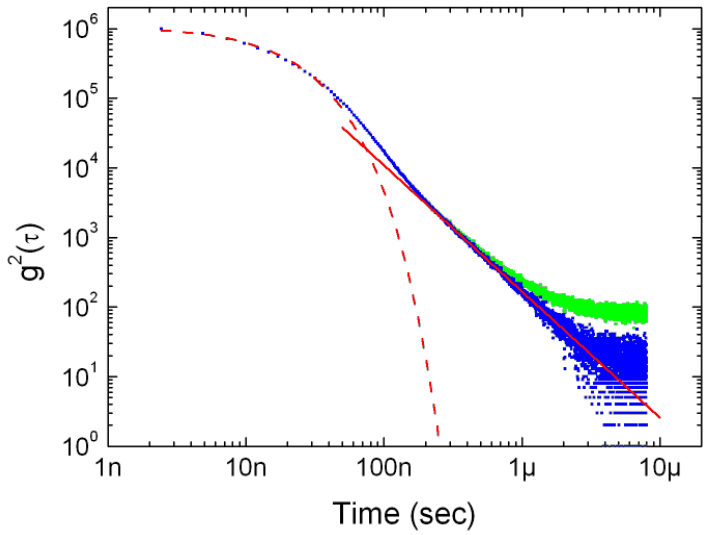

Fig. 5.16. TRPL measured from the Evi620 ensemble sample. Green dots represent the TRPL not corrected for background while blue dots are background corrected. Red solid line is a linear fit to the tail of the decay and corresponds to a gradient of 1.81. Red dashed line is a single exponential fit to the TRPL decay and gives a fluorescence lifetime of 18.3 ns.

5.4.3 QDQW

The QDQW sample used in this section is made by Steve Daniels from the Department of Chemistry, University of Manchester [50]. The emitting layer consist of CdSe while the centre "core" is an alloy of $Zn_{0.5}Cd_{0.5}S$ and the outer shell is made from ZnS. The code name for the sample is SD452.

5.4.3.1 SD452 1018NC2

This NC shows a typical data set obtained from the sample SD452. The TRPL decay in Fig. 5.17 shows a power law gradient of -2.00. The autocorrelation function with a bin time of 5 μs is fitted with the analytical function to extract a power law exponent of 1.92. A threshold is selected near the centre between the two intensity peaks of the intensity time trace to obtain the blinking data. The values extracted are α_{on} =1.82

and α_{off} = 1.97, since α_{off} is larger than α_{on} therefore we assign the extracted $g^{(2)}$ exponent to be m_{off}.

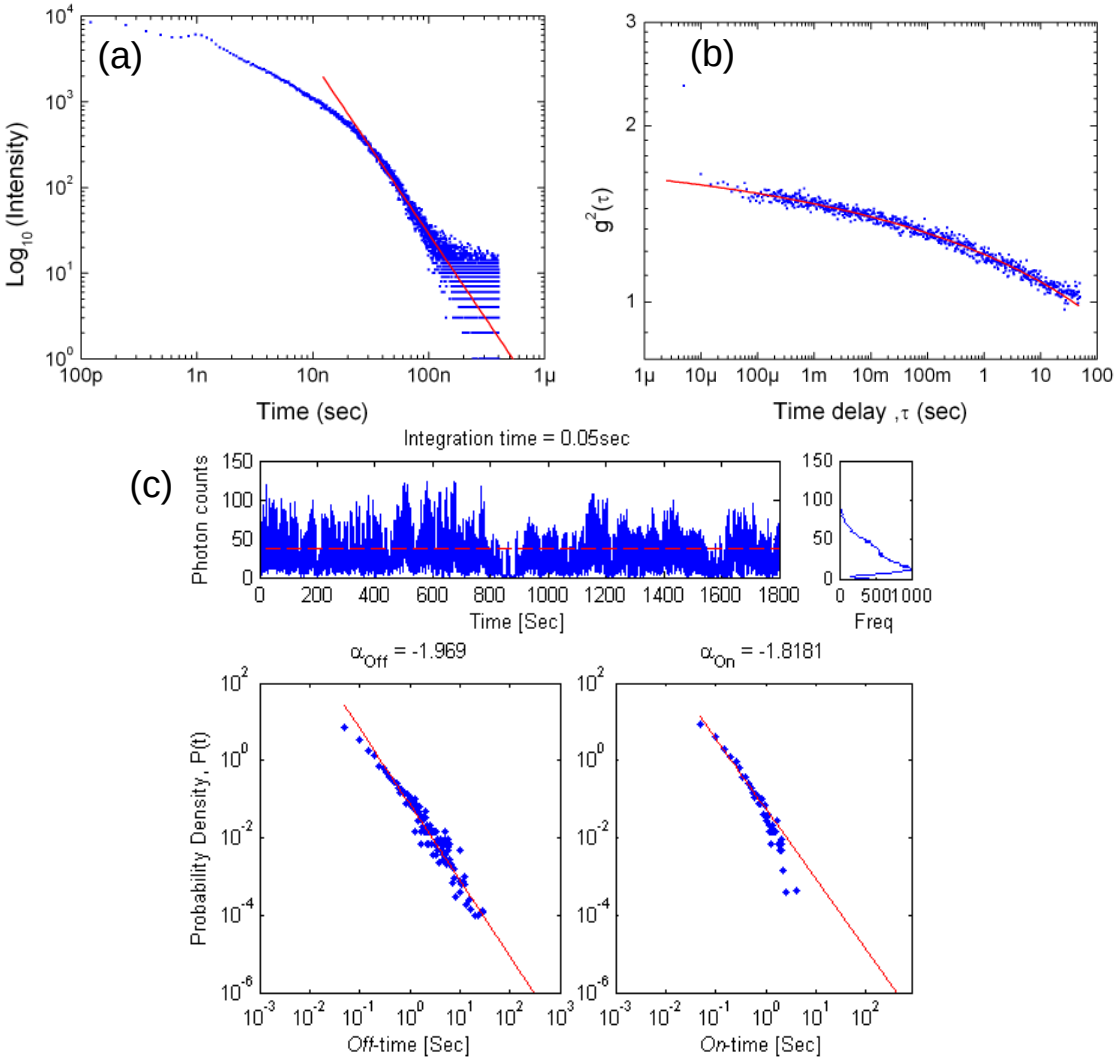

Fig. 5.17. (a) Background corrected TRPL decay curve of the single NC (blue). Red solid line is a linear fit to the tail of the TRPL with a gradient = -2.00. (b) Autocorrelation function of this NC (blue: 5μs bin time). Red solid line is a theoretical fit to extract the power law exponent, *m* = 1.92. (c) Blinking statistics extracted from the intensity time trace at the threshold level set by the red dash line.

5.4.3.2 SD452 1020NC9HP

The TRPL decay in Fig. 5.18(a) gives a power law gradient of -1.94. The autocorrelation data is shown in Fig. 5.18(b). From the intensity-time trace in Fig. 5.18(c), the NC appears to be a strong emitter before it dies after ~800 sec. We believe it is dead and not in a long *off*-state due to the high peak power used (the

laser used in this particular case to excite the NC is of the order of 10 $kWcm^{-2}$). This high laser intensity causes the NC to chemically photobleach over the period from 200 sec to 700 sec as seen from the gradual decrease in the fluorescence intensity. Although the slow varying envelope of the photobleaching activity seems to decay in the time regime of about 1-10 sec, but the actual bleaching mechanism could be in action at a faster rate, therefore we fit the analytical $g^{(2)}$ function to the data at short time regime only and extracted an exponent of 1.91. The power law exponents from blinking threshold analysis are α_{on} =1.50 and α_{off} = 1.89 respectively. Since α_{off} is larger therefore the exponent extracted from $g^{(2)}$ is assigned to m_{off}.

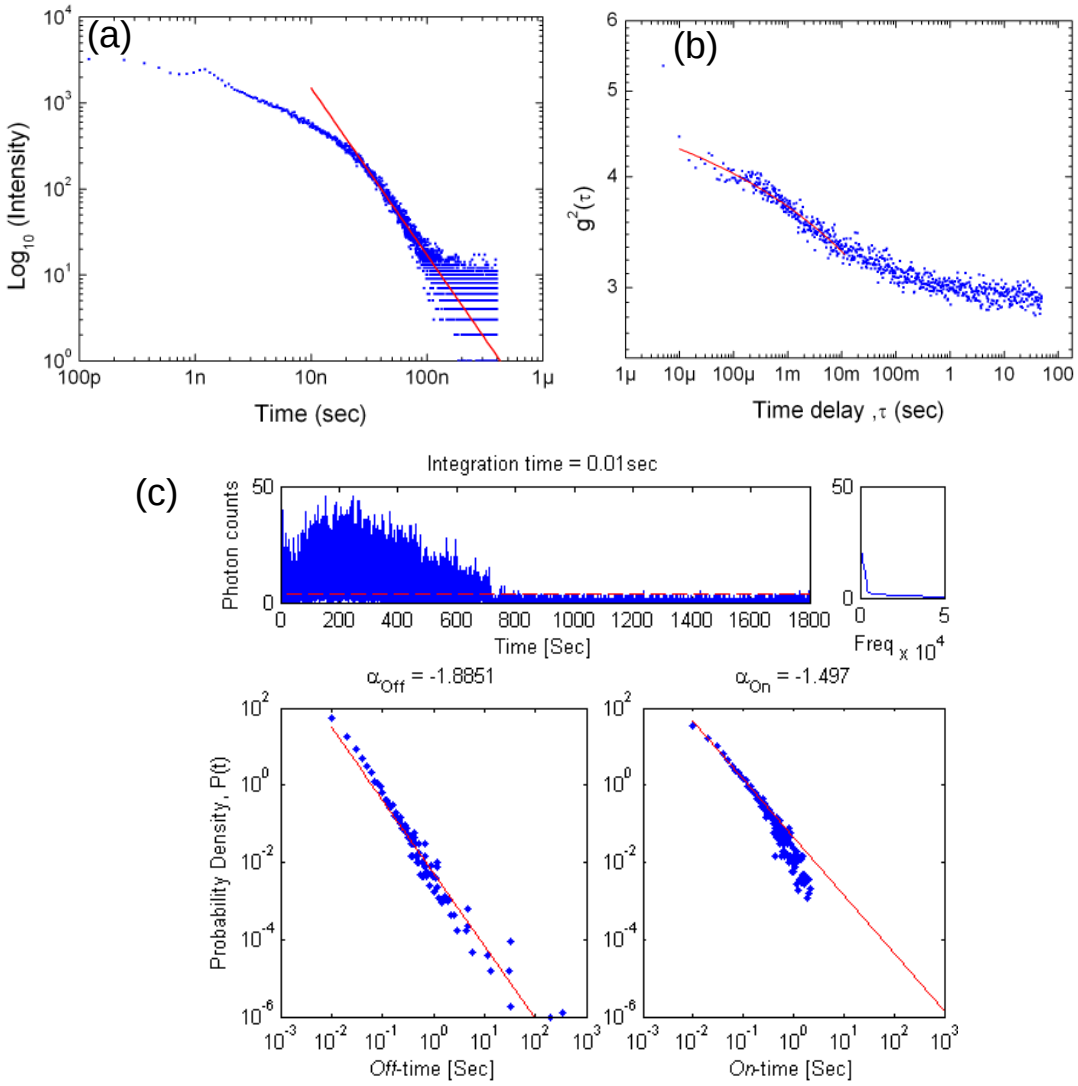

Fig. 5.18. (a) Background corrected TRPL decay curve of the single NC (blue). Red solid line is a linear fit to the tail of the TRPL with a gradient = -1.94. (b) Autocorrelation function of the same NC (blue: 5μs bin time). Red solid line is a theoretical fit to extract the power law exponent, m = 1.91. (c) Blinking statistics extracted from the intensity time trace at the threshold level set by the red dash line.

5.4.3.3 SD452 1021NC16HP

The TRPL data shows a power law gradient of 1.10 in the time regime from 5 ns to 500 ns in Fig. 5.19(a). The intensity time trace shows that the NC is photobleaching and it appeared to be dead after being illuminated for 1000 sec under high laser intensity (in the order of 10kWcm^{-2}), therefore we set the threshold to be above the average background intensity when the NCs is not fluorescing. This gives an *off*-time power law exponent of 1.84, however there is a hint that the power law exponents

may have changed to a smaller value in the time regime below 50 ms. Fitting a linear gradient at this shorter time scale suggested a power law exponent of 0.8 as shown by the solid green line in Fig. 5.19(c). The *on*-time statistics appears to be like a single exponential in the milliseconds regime as seen by the linear gradient in the log-linear plot in Fig. 5.19(c). In addition, if one tried to fit a power law to the data points it will result in an exponent of 2.75, much larger than what is usually expected from blinking statistics. However the limited data points make it difficult to justify in either case. Comparing the TRPL exponent and the off-time statistics we are led to suspect there may be a change in *off*-time power law exponent in the tens of milliseconds time regime, we will now turn to the autocorrelation function to find more clues. Although the autocorrelation data has a concaved curvature similar to SD4521020NC9HP, our TRPL and blinking data suggested a change in the *off*-time power law exponent and a single exponential *on*-time distribution, therefore we try to analyze the autocorrelation data slightly different to what we have done before. Assuming the *on*-time distribution is single exponential from 10 ms onwards, we attempt to fit a linear gradient to the segment of autocorrelation data with longer time delay and obtained an *off*-time exponent of 1.95, this figure is comparable to the blinking *off*-time exponent in the same time regime. However this gradient slightly misses the data at the shorter time regime, therefore we fit it again using the analytical function described by Eq. 5.28 with the assumption that the *on*-time follows a power law at the shorter time regime and the single exponential we see is a roll-off from the power law. This gives us an exponent of 1.90 which may be a signature of the *on*-time power law if we assume the *off*-time power law exponent has changed to 1.1 in the shorter time regime. The intersection where the two fittings meet is about 20 ms, roughly equal to time where we see a deviation from the *off*-

time power law. The autocorrelation function may have been complicated by different dynamics thus unable to provide a firm evidence to confirm the change in power law. However combining data from the three time regimes provides a hint to a possible change in *off*-time power law for this particular NC.

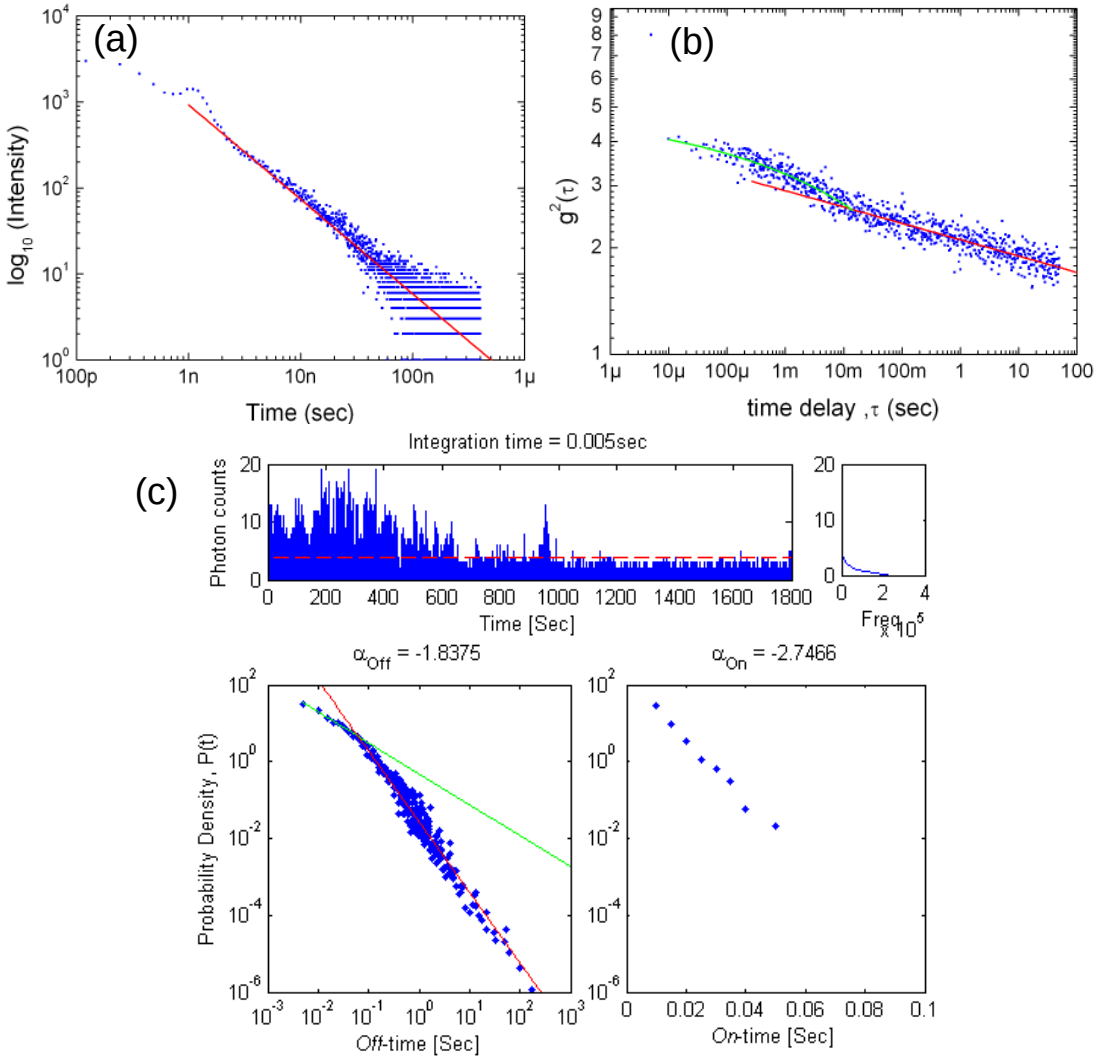

Fig. 5.19. (a) Background corrected TRPL decay curve of the single NC (blue). Red solid line is a linear fit to the tail of the TRPL with a gradient = -1.10. (b) Autocorrelation function of the same NC (blue: 5μs bin time). Red solid line is a linear fit assuming exponential *on*-time to extract the power law exponent, m = 1.95, at longer time delay. Green solid line is a theoretical fit assuming both *on*- and *off*-time power law at shorter time regime, the extracted power law exponent is m = 1.90. (c) Blinking statistics extracted from the intensity time trace at the threshold level set by the red dash line. Off-time power law in the short time regime appeared to deviate from the exponent of 1.84 for the longer time regime. The change in gradient starts at around 50 ms, a linear fit at the short time regime gives a gradient of 0.8 shown by the solid green line.

5.4.3.4 A summary of the SD452 single NCs observed

"HP" in the sample name stands for high power, the peak laser intensity used to excite these NCs lies in the order of 10kWcm^{-2}, whereas other NCs are excited by a peak intensity in the order of 1kWcm^{-2}. The ensemble TRPL is shown in Fig. 5.20. The average distance between NCs in the ensemble is estimated to be about 5 nm thus no enhanced blinking is expected from this sample. The power law gradient extracted from the ensemble TRPL coincides well with the average power law gradient obtained from single NCs, therefore it suggested that the majority of the NCs would have a power law gradient of 1.79 in the nano- to micro-second time regime. This figure coincides well with the average *off*-time power law exponents obtained from the 18 single NCs measured and is supported by the autocorrelation data in the mid-time regime, hence it may suggest that the *off*-time power law exponent is continuous and unchanged over the 9 decades in time measured. However as we can see from the single NC data, it is possible that a few NCs (1021NC16HP) may have a change in power law exponent from ~1.8 down to ~1.1 where the change happens at around 10ms time regime. Pelton et al. have observed a similar change in the exponent in terms of magnitude and time for the *on*-time power law[37], however our data suggested that although some NCs do experience a change in power law exponent but the majority of the NCs in this sample would have a constant exponent over the time regime we have measured.

Table 5.4. Summary of single NC power law exponents extracted from the sample SD452

	TRPL (10ns-1μs)	$g^{(2)}$ (5μs-10s)		Blinking (50ms-100s)	
	m_{off}	m_{on}	m_{off}	α_{on}	α_{off}
1018NC1	1.86	-	1.94	1.74	1.86
1018NC2	2.00	-	1.92	1.82	1.97
1018NC3	1.82	-	1.85	1.52	1.94
1019NC4	2.00	1.96	-	1.90	1.76
1019NC5	1.72	-	1.77	1.58	1.80
1019NC6	2.00	-	1.80	1.24	1.83
1019NC6HP	1.97	-	1.92	1.44	1.76
1019NC7	2.04	-	1.89	1.88	2.19
1019NC7HP	1.66	1.95	-	2.06	1.69
1020NC8	1.98	-	1.91	1.36	1.93
1020NC9HP	1.94	-	1.91	1.50	1.89
1021NC11HP	1.54	1.90	-	2.19	1.60
1021NC12HP	1.97	-	1.89	1.87	2.20
1021NC13HP	1.79	-	1.82	1.66	1.79
1021NC14HP	1.65	-	1.94	1.57	1.79
1021NC15HP	1.15	1.51	-	1.69	1.42
1021NC16HP	1.10	-	-	-	1.84
1022NC17	1.76	1.95	-	1.80	1.73
1022NC18	2.38	-	1.87	1.59	2.27

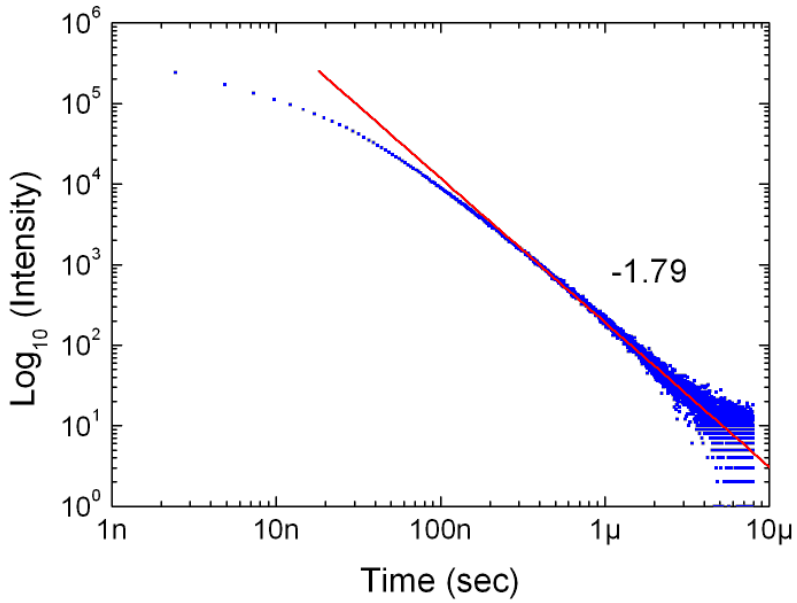

Fig. 5.20. TRPL measured from a SD452 ensemble sample. Red solid line is a linear fit to the tail of the decay; corresponding gradient is shown to the right of the data.

5.5 Discussion

From the data presented above, we only observed a systematic change in the *off*-time power law from one of our core/shell samples (Evi600) that was purchased from Evident Technology®. All other samples, including a different core/shell sample from Evident Technology (Evi620), suggest a constant and continuous power law exponent spanning over the time regime from 10ns to 100 sec. The two core/shell samples from Evident Technology are identical in terms of the shell chemistry where the difference lies in the core. Evi620 contains a small amount of zinc in the core that acts as an alloying agent whereas Evi600 does not contain zinc in the core. In addition, the core of the Evi600 core/shell sample is identical to the core only Evicore sample, therefore from a chemical standpoint one would suspect the Evi600 and Evicore to show a similar characteristic. However our results suggested the opposite, both Evi620 and Evicore demonstrated a constant *off*-time power law exponent whereas Evi600 shows a change in the *off*-time power law exponent. A constant power law exponent would favour the tunnelling model to an exponential distribution of trap sites whereas the diffusion model (either in energy or space) predicts a change in the power law exponent at some time t_c. A 1D/2D normal diffusion naturally gives the nominal -1.5 power law exponent and predicts a change down to -0.5 at $t < t_c$. However the model needs to incorporate anomalous diffusion in order to account for power law exponents other than -1.5 and -0.5 at time at $t > t_c$ and $t < t_c$ respectively. If we consider the three samples that shows a constant power law, both the core only and QDQW has a relatively weaker confinement for the carriers compared to the Evi600 core/shell sample. Although Evi620 is also a core/shell structure, the alloying between the core and the shell may weaken the

confinement, and by inspecting the intensity time trace shown in Fig. 5.15(c), we see spike like *on*-times suggesting the NC is not as well passivated. Hence the less confined carrier wave functions would mean tunnelling to the surrounding trap sites have a larger influence to the blinking statistics. The Evi600 core/shell NCs having a well confined carrier wave function but displays a diffusion dynamics suggested an intermediate diffusing mechanism that affects the carrier dynamics. It is possible that the ejected carrier will undergo some kind of diffusion process (in space or energy) before it finally tunnels out of the shell and being captured by the surrounding trap sites.

Chapter 6
Embedding Single NC in ZnO thin film using Atomic Layer Deposition

6.1 Reasons for embedding

Controlling the particle size during the period of crystal growth for colloidal semiconductor nanocrystals provides some flexibility in bandgap engineering. Such ability makes the colloidal semiconductor nanocrystals an attractive building block for devices that utilised the semiconductor bandgap. Some examples includes macroscopic devices such as LEDs[65], photodetectors[66], solar cells[67], and sensors[68], or if used individually as single electron transistors[69] and single photon sources[70]. Many of these applications involve the optical absorption or emission properties of the nanocrystals, and require that they be embedded into a semiconductor p-n junction for carrier extraction or injection. Many also require that the properties of the nanocrystals be stable over long time periods, and that phenomena such as photobleaching, spectral drift and fluorescence blinking be minimal. Therefore the purpose of embedding nanocrystals in an inorganic matrix is twofold: first, to create a platform for future device fabrication, and secondly to provide effective passivation for the trap sites on the nanocrystal surface. One puzzling mystery of nanocrystals is that their unsteady dynamics, particularly for

fluorescence intermittency, seems to be related to a disordered surrounding environment. Epitaxial quantum dots grown in an ordered crystalline structure appear to have a higher degree of optical stability. Blinking is generally not observed in these quantum dots, or at least its dynamic is not as diverse as a power law. Embedding the nanocrystals in a coherent inorganic lattice is an attempt towards answering that question.

6.2 Summary of the embedding process

Our collaborator from Chonbuk National University, Korea, carries out the actual process of embedding NCs into a ZnO thin film through Atomic Layer Deposition[71]. A summary of the process is presented below.

6.2.1 Brief introduction of Atomic Layer Deposition

As the name suggests, Atomic Layer Deposition (ALD) is a process that grows thin films, monolayer by monolayer. The principle of ALD lies in a self-limited surface reaction between reactants. As the reactant is injected into the ALD chamber it is chemisorbed to the surface, i.e. absorbed onto the surface by forming a chemical bond. The control of exactly “half” a monolayer growth at each precursor injection lies in the precursor gas flow and reaction temperature. The gas flow of the precursors needs to be sufficiently high so that full exposure of the surface to the reactant is completed in a reasonable time. The precursors can then be absorbed to the surface by physisorption that involves weak van der Waal’s forces or by chemisorption that requires some activation energy to form strong chemical bonds. At a sufficiently high temperature chemisorption dominates and the formation of a

single monolayer in each cycle is achieved. The ALD system for ZnO growth in our collaborator's site uses Diethyl Zinc (DEZn, $Zn(C_2H_5)_2$) and oxygen gas as Zn and oxygen sources respectively. Argon is utilized both as a carrier for the precursor and as a purging gas. In addition, the noble gas creates an inert environment for the reaction growth. Fig. 6.1 illustrates the growth of one monolayer of ZnO in a single cycle. (a) At the first injection of DEZn precursor, chemisorption of Zn at the substrate surface is achieved by losing one of the C_2H_5 molecules. Excessive DEZn molecule may be bounded as a secondary layer by weak physisorption. (b) Subsequent Ar gas purging removes the excessive reactants by a physical process and a "half" monolayer remains on the surface. (c) The second injection of O_2 gas is chemisorbed to the surface of the first half monolayer and undergoes some exchange reaction to replace the remaining C_2H_5 molecule. (d) Subsequent Ar purge removes the excessive gas and molecules leaving behind one monolayer of ZnO on the surface. One cycle of the ALD takes ~40 seconds and the growth rate is about 2.1~2.4 Å per cycle. Since the reactants are gaseous and are absorbed by the surface through a chemical bonding, the step coverage of ALD is good.

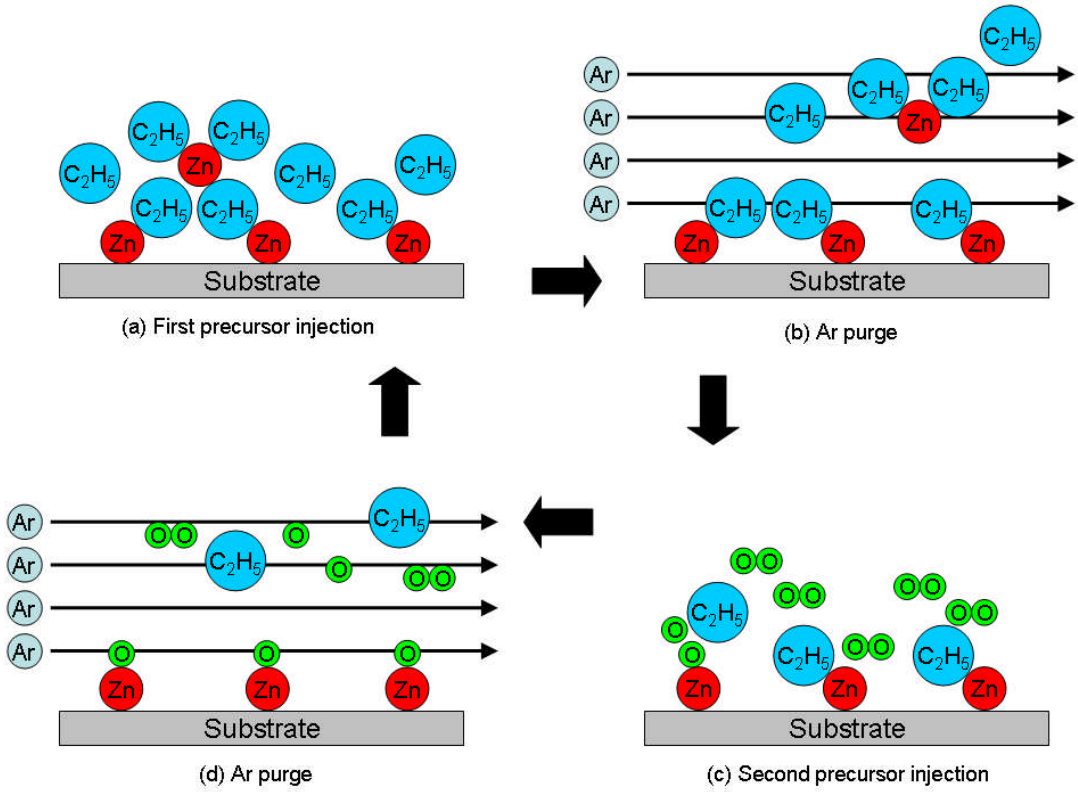

Fig. 6.1. Schematic for a single cycle of ALD to grow one monolayer on ZnO

6.2.2 Experimental details of the embedding process.

Core/Shell nanocrystals purchased from Evident Technology® are used in the embedded sample. Fig. 6.2 (created by S H Kim) illustrates the embedding process: (1) deposition of ZnO buffer layer (20 nm) onto Si substrate at 220 °C, (2) spin coating of the NC solution onto ZnO/Si then baking at 220 °C for 30 min in the ALD chamber to remove organic ligands from the NC, and (3) overgrowth with ZnO cap layer (30 nm) over NCs/ZnO/Si. Samples were prepared with two different densities of nanocrystals: approximately 100 NCs per μm^2 for ensemble measurements and 0.01 NCs per μm^2 for single nanocrystal measurements. Control samples were prepared using nanocrystals spin-cast from solution of toluene with 0.5 wt% polymethyl methacrylate (PMMA) directly onto quartz substrates.

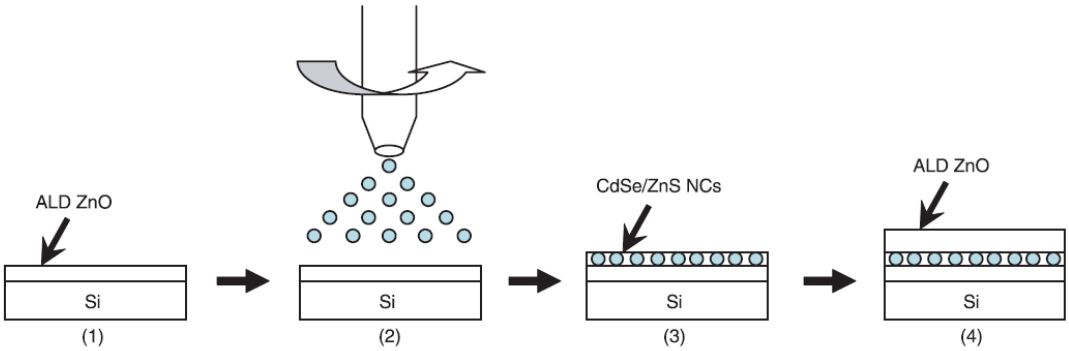

Fig. 6.2. Schematic illustration of embedding CdSe/ZnS nanocrystals into ZnO layer

To ensure the embedded NCs are homogeneously surrounded by the ZnO matrix, it is essential to remove the long chain organic ligands bonded to the NC surface before the capping layer is deposited. It is well known that the organic ligands can provide extra surface passivation even for a NC core that has an inorganic shell grown over it, therefore it is expected that as the ligands are removed the ensemble QY will drop. Three highly concentrated ensemble samples are made by spin coating the original concentrated NC solution (Evi620) purchased from Evident Technology onto a silicon substrate with a ZnO buffer layer. Two of the samples are annealed at 100 ^{o}C and 200 ^{o}C respectively in the ALD chamber with a base vacuum of 10^{-4} torr and a nitrogen flow at 50 sccm. The ensemble PL is measured with a standard spectrophotometer for a quick characterisation. However, the sensitivity of the standard spectrophotometer is relatively low compared to our custom-made single emitter capable system, hence the highly concentrated sample containing about 2000 NCs per μm^2 is required. The PL intensity of the control sample and the 100 ^{o}C annealed sample are comparable whereas the 200 ^{o}C annealed sample shows a PL drop by about a factor of two. The PL intensity drop of the 200 ^{o}C annealed sample is likely to be due to detached ligands rather than oxidation accelerated by the thermal energy, owing to the inert annealing environment. Subsequent ZnO capping further reduced the PL intensity by a factor of 10 for these

samples. The drop in ensemble PL intensity upon capping could be due to two reasons. Firstly, the excess oxygen may cause oxidation to the NC core whereby reducing its size and resulting in a decrease of the absorption cross-section[72]. Secondly, the close packing of the NCs result in an inhomogeneous growth of the ZnO capping layer thus creating more defects around the NCs that can act as nonradiative decay routes. Further characterisation with our more sensitive spectrometer reveals that the sample without pre-annealing but capped with ZnO at 220 ^{o}C has far more emitting NCs (>20 times) compared to the samples pre-annealed at 100 ^{o}C and 200 ^{o}C that are also capped with ZnO at 220 ^{o}C. The main difference for the samples is that the pre-annealed samples were removed from the chamber after annealing to measure its PL intensity, therefore the NCs are exposed to the atmospheric environment with the ligands removed, such condition may render the NCs more prone to degradation. On the other hand, in order to apply ZnO capping to the non-annealed sample, the temperature was raised to 220 ^{o}C in a controlled environment inside the ALD chamber. Once the temperature reached 220 ^{o}C, the capping layer is immediately applied, we did not leave the sample at this temperature for further annealing thus it leaves no time for the NCs to degrade with ligands detached. As a result, we believe that it is crucial for the baking procedure in step 2 to be carried out inside the ALD chamber and the capping layer is applied immediately after the ligands are removed.

6.2.3 Structural characterization of the embedded samples

S H Kim from Chonbuk National University provides the structural characterization of the embedded samples presented in this sub section.

Fig. 6.3 shows AFM images of 500 nm × 500 nm area at different stages of

preparation. Comparing Fig. 6.3(a) and (b), the NCs are clearly visible as white and evenly distributed on the smooth Si substrate. However since the ZnO thin film consists of nanosize ZnO particles (i.e. polycrystalline), as it is grown with an uneven surface, it is difficult to assess the density of the NCs on the ZnO layer (Fig. 6.3(c)). The NCs as shown in Fig. 6.3(b) are about 13-15 nm in size whereas the expected size for these NCs is ~6 nm. The reason for such an increase is when the AFM tip scans across the NC, the size profile is broadened by the finite width of the tip.

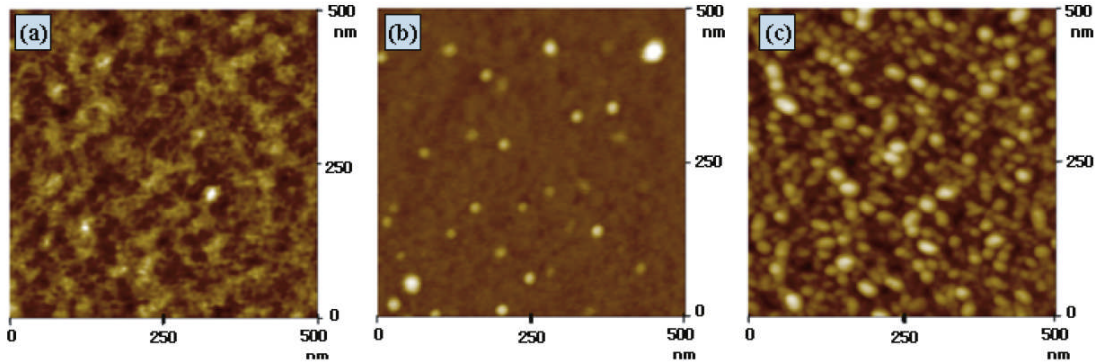

(a) Si (b) NCs/Si (c) NCs/ZnO/Si

Fig. 6.3. AFM images of (a) bare Si substrate, (b) CdSe/ZnS nanocrystals on Si and (c) on ZnO(30nm)/Si.

Fig. 6.4 shows the SIMS spectra of the CdSe/ZnS nanocrystal spun on ZnO/Si. The NCs compositions were analysed with a Ga^+ source at 6kV and 3nA with minimum beam size of 10 μm. The base pressure was kept at 1.18×10^{-6} Torr, while the pressure was increased to 3.36×10^{-4} Torr during analysis. SIMS analysis is essentially a sputtering process. As the sample surface is bombarded with high-energy ions, atoms or molecules are removed from the surface. Some of the ejected particles are charged and are known as secondary ions. Passing the secondary ions through a mass spectrometer provides information on the chemical composition.

SIMS analysis is very sensitive to small amounts of elements present on the sample surface, however the sensitivity can vary from element to element therefore the relative intensity of peaks is not suitable to calibrate for the composition concentration. Nevertheless the existence Zn, S, Cd and Se peaks from SIMS analysis indicates the presence of nanocrystals. Also note that the sputtering effect of the primary ions can go quite deep into the surface (>10 μm) hence the observation of silicon and silicon oxide peaks.

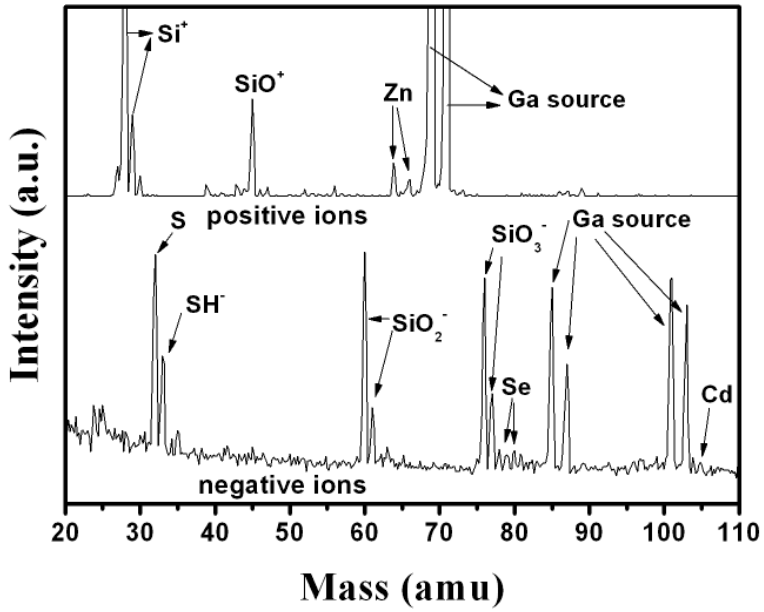

Fig. 6.4. SIMS spectra of the CdSe/ZnS nanocrystal spun on ZnO/Si substrate.

6.3 Optical Characterization of Embedded NCs

The structural characterisation provides some evidence for the physical existence of single NCs in the embedded sample. Photoluminescence spectroscopy is carried out to probe the effect of the embedding on the optical properties of the core/shell nanocrystals.

6.3.1 Ensemble Photoluminescence Spectra

The ensemble PL spectrum is acquired in order to investigate the overall effect of the embedding. The results are illustrated in Fig. 6.5, both the ZnO and PMMA embedded ensembles show a strong PL peak near 590 nm. These two peaks originate from the embedded NCs alone is confirmed by a control sample of pure ZnO and PMMA under 473 nm excitation that shows no peak at this wavelength. The two PL peaks are normalized for direct comparison. We did not compare the QY with and without embedding in ZnO from the relative peak intensities of the two ensembles for two reasons, firstly we have not taken steps to optimize the uniformity of the NC density and secondly embedding ensembles will require further refinement to the process recipe in order to reduce defects in the ZnO thin film caused by the presence of excessive NCs. However comparing single NC QY is possible and will be discussed later.

The fluorescence peak of the core/shell NCs in PMMA is at $\lambda = 593.6$ nm with a full-width-half-maximum (FWHM) of 31 nm. Upon embedding in ZnO we observed that the peak has shifted slightly to the blue at $\lambda = 586.1$ nm, with a slightly larger FWHM. One may expect the ZnO matrix, having a smaller bandgap compared to the organic matrix, to slightly reduce the confinement energy of the photogenerated exciton in the nanocrystals and hence to cause a small red-shift. The most likely explanation is that diffusion of oxygen atoms from the ZnO film through the ZnS shell causes some oxidation of the CdSe core, thus increasing the band gap and reducing the effective core size. This would also provide an explanation for the concomitant increase in inhomogeneous broadening, since it has been shown that smaller nanocrystals photooxidize, and therefore blue-shift, more quickly than larger nanocrystals[73].

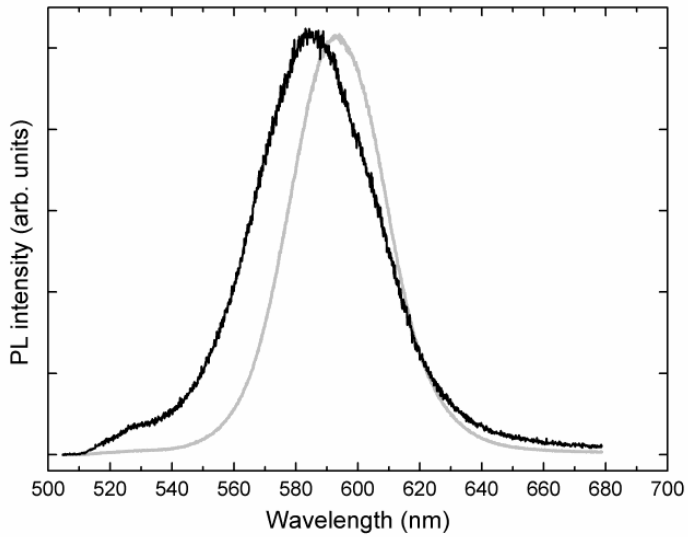

Fig. 6.5. PL spectra from ensembles of nanocrystals. Black and grey lines represent ZnO and PMMA embedded samples respectively. PL peaks are normalized for direct comparison.

6.3.2 Single NC Photoluminescence Spectra

We believe one possible cause for the decrease in PL intensity for the concentrated ensembles after capping with ZnO layer may be due to an inhomogeneous growth of ZnO around the closely packed NCs. Excessive amount of defects such as zinc and oxygen vacancies or interstitials, and antisite defects can actively quench the PL through nonradiative routes. However if the NCs are sufficiently far apart the ZnO layers could have a greater relaxation flexibility thus introducing less defects especially in the area further away from the NCs, hence it can still provide some passivation for embedded single NCs. Although the embedding process certainly requires further refinement and optimization, we have had some success in a few samples with embedded single NCs.

We compared the PL spectra of single NCs embedded in a ZnO film to the single NCs embedded in PMMA, at room temperature and at 78 K. Several NCs were measured in each case, and typical spectra are shown in Fig. 6.7 (note that each spectrum is from a different NC). Spectra from both samples show strong

homogeneously broadened zero phonon emission. The intensity of the brightest nanocrystals is relatively unchanged by the ZnO embedding process under similar illumination intensity as shown in Fig. 6.6. Since the nanocrystals are only 30 nm beneath the surface, much less than the optical wavelength, refraction effects of the ZnO–air interface can safely be neglected, and the measured intensities can be compared directly. We conclude that with the right process conditions, the ZnO embedding process has not adversely affected the quantum yield of the nanoparticles. This is quite a remarkable result, particularly since the baking process that is used to remove the organic ligands from the nanocrystals' surface drastically reduces the single particle emission intensity so that we are unable to measure single NC PL on baked but non-embedded NCs. The capping of the NCs with the 30 nm ZnO layer therefore appears to restore the quantum yield to that of the NCs with ligands, presumably by providing passivation of surface trap states with the deposited ZnO as an alternative to the organic ligands.

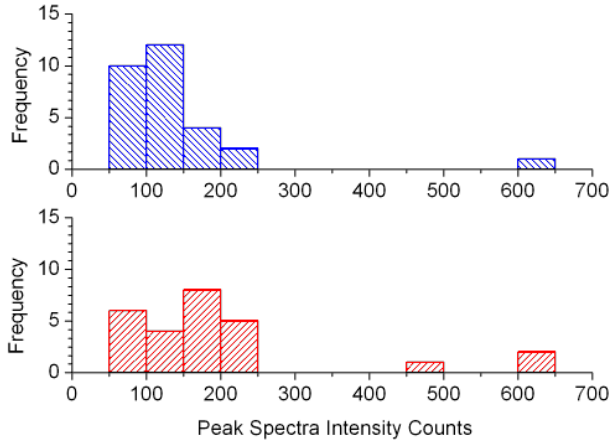

Fig. 6.6. Histogram of peak intensities in single NC spectrum acquired with a 60 sec integration time at room temperature. The top plot (blue) is for single NCs in PMMA and the bottom plot (red) is for single NCs embedded in ZnO.

The widths of the zero phonon emission lines are very similar for the ZnO and PMMA embedded NCs, suggesting that ZnO embedding did not substantially

change the electronic or vibronic states of the nanocrystals. The 78 K spectra show a clear phonon satellite located about 27 meV to the red of the main PL peak. These are also of similar intensity in the ZnO and PMMA embedded nanocrystals, indicating that both the energy and the coupling strength of the optical phonon remain approximately unchanged. Fluorescence blinking of the single nanocrystals is qualitatively similar for the two samples.

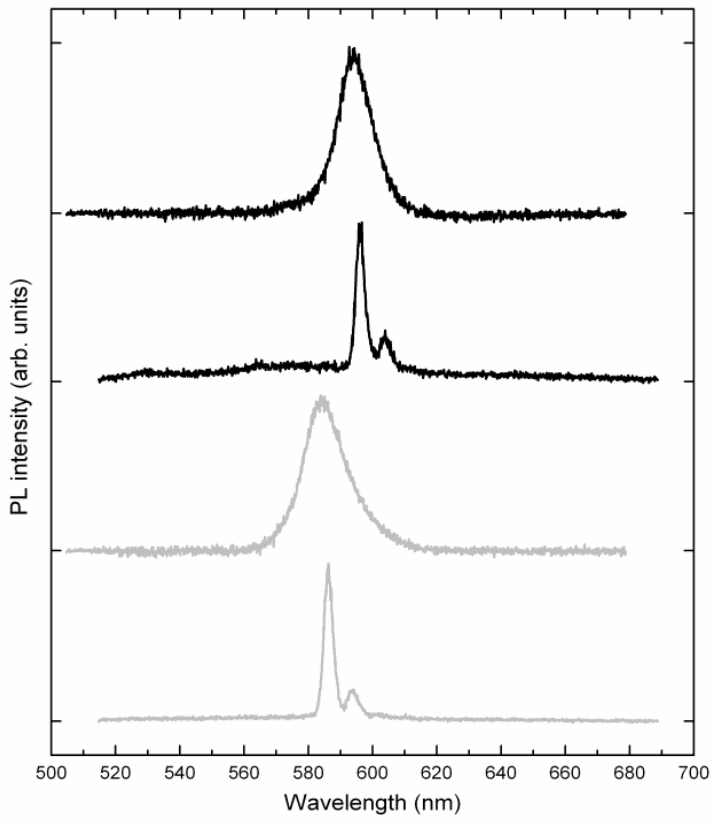

Fig. 6.7. Typical single nanocrystal spectra measured from ZnO embedded (black) and PMMA embedded (grey) samples. Both samples were measured at RT (upper curve) and at 78 K (lower curve)

To test whether the similarity between the ZnO and PMMA embedded NCs held for the less concentrated ensemble, we measured several NCs from each sample at room temperature. Note that in doing so we selected only the brighter NCs in the ensemble, so the data do not represent an average for all NCs in the sample but a snapshot of some of the strongest emitters in each case. Fig. 6.8 shows a histogram

of the FWHM results. All of the line shapes are predominantly Lorentzian for most of the peak, but show some Gaussian character towards the edges. These Gaussian portions are likely to result from spectral drift, commonly observed in single nanocrystal fluorescence, particularly at high excitation powers that result in greater carrier movement in the surrounding matrix. In making each of our single NC PL measurements we have reduced the excitation power to a level at which further reductions in power do not affect the line shape, so providing a basis for comparison between the line widths measured.

When considering our statistical sample we find that the emission line shapes of the ZnO embedded NCs generally have slightly less Gaussian character, and narrower line width (FWHM = 12.2±1.9 nm), than the NCs in PMMA(FWHM = 13.3 ± 1.8 nm). We illustrate this result by fitting normal distributions to the two histograms in Fig. 6.8. A t-test of the data sets reveals a confidence level of 97% that the observed difference between the two mean line widths is not by chance and that a systematic reduction in the line width occurs upon embedding the NCs in the ZnO. This suggests, as expected, that spectral drift caused by fluctuations in the local electric field is slightly reduced in the crystalline matrix as compared with the amorphous surroundings.

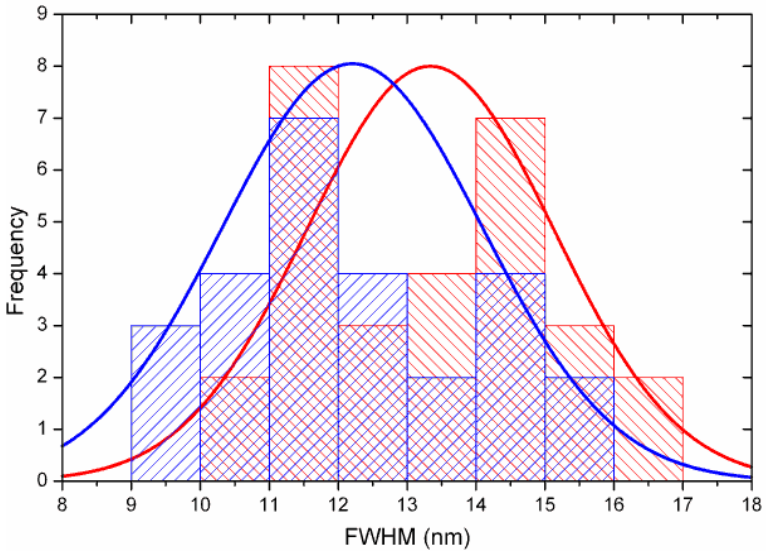

Fig. 6.8. Histogram of the FWHM of single nanocrystal PL emission (bin size = 1 nm) for ZnO embedded (solid blue) and PMMA embedded (solid red) single nanocrystals. The normal distribution illustrate the mean and standard deviation of the two sets of data.

6.4 Summary and future work

The fact that the spectral diffusion of the core/shell NCs has been reduced in the embedded sample suggests that some degree of surface passivation is provided by the ZnO matrix. In addition, we can still detect single NC photoluminescence from the embedded sample after the sample is left in an atmospheric environment for over a year, in sharp contrast to samples embedded in PMMA where single NC photoluminescence tends to degrade to an undetectable level after about two months. This is another indication of the ZnO matrix providing a stable and isolated environment for the nanocrystals. However it is also true that blinking statistics are not changed for the embedded single NCs, although some embedded NCs did demonstrate a prolonged *on*-state (~5 min) the majority of the NCs blink equally frequently as the NCs in PMMA matrix. Although our initial tests demonstrated some positive results for the embedded samples, the embedding process certainly needs more refinement. Apart from recipe tuning to achieve the optimum growth

conditions, a different embedding material such as ZnS may be a more promising route as it removes oxygen from the process thus minimised the possibility for oxidation during the embedding process.

Some results in this chapter are published in Nanotechnology Volume 19, Number 36, Article No. 365202 (2008).

Chapter 7
Conclusion and future work

Carrier dynamics in single semiconductor NC leading to power law behaviour is a mystery that may be shared among different nanomaterials. Our combined analysis to TRPL decay, $g^{(2)}(\tau)$ autocorrelation function and blinking statistics provide an experimental method to explore the power law dynamics over 10 decades in time. By doing so we have shed light on some of this power law mystery yet also raised some other questions. For the three types of NCs (core only, core/shell and QWQD) we have investigated at room temperature, samples of each type have shown a continuous and constant *off*-time power law exponent over ten decades in time. However one well passivated core/shell sample (Evi600) have indicated a change of *off*-time power law exponent in the time regime around 10 ms. Pelton et al.[37] analysed the power spectra density function for single core/shell NCs and observed a similar change in the *on*-time power law exponent where the cross over point, t_c, is around 5-35 ms as well. They derived an equation for the critical time as, $t_c = \frac{4k_B T}{\kappa t_{diff} k_r^2}$, where T is the temperature and k_B is Boltzmann's constant; κ, t_{diff}, and k_r are variables associated with the diffusion model. Two different sets of data appear to support two different carrier dynamics models, namely, the continuous and constant power law exponent supports the charge-tunnelling model while the switch

of exponents supports the diffusion model. At this point we are led to postulate the tunnelling model may be more significant for the not so well passivated samples (core only, QDQW, and one less well passivated core/shell), since their electronic wave function extends more into the surrounding hence traps on the NC surface or in the environment will play a more dominate role. Jones et al.[64] have measured and modelled a distribution of surface traps and core/shell interface traps on NCs. On the other hand a well passivated core/shell NC having a more confined electronic wave function may render the tunnelling less probable hence an electron transfer will rely on the diffusion controlled resonance of excited state and traps state energy levels. Another possible explanation is that switching of power law exponents existed for the less well passivated NCs, but the critical time of switching is faster than the time regime probed by our TRPL experiments. Our preliminary low temperature TRPL experiments seems to provide evidence for this picture since we observed a change in power law exponent for all three types of NCs when the temperature is lower to 77K. At this temperature, t_c is ~1μs for core only and core/shell NCs while $t_c > 10$ μs for QDQWs. However observing the change at 77K but not at RT seems to contradict with the relationship between t_c and temperature derived by Pelton et al. (expected t_c to increase when T increases). We also note that although a change in power law exponent is observed, the magnitude of change is smaller than what is predicted by the DCET model, even when anomalous diffusion is considered. The model predicts a sum of two for the exponents before and after switching while the observed sum by Pelton et al. and us are always greater than two. Nevertheless, a more detailed temperature dependent experiment on different NC ensembles or possibly single NCs would provide more insight into this discrepancy. It will also be

interesting to see if the blinking suppressed thick shell NCs[74, 75] will show a power law tail in the TRPL decay and what happens to it when it is cooled.

Bibliography

1. *SCENARIOS FOR THE FUTURE,* in *How might IP regimes evolve by 2025? What global legitimacy might such regimes have?* 2007.
2. Yu, W.W., et al., *Experimental Determination of the Extinction Coefficient of CdTe, CdSe, and CdS Nanocrystals.* Chemistry of Materials, 2003. **15**(14): p. 2854-2860.
3. Robelek, R., F.D. Stefani, and W. Knoll, *Oligonucleotide hybridization monitored by surface plasmon enhanced fluorescence spectroscopy with bio-conjugated core/shell quantum dots. Influence of luminescence blinking.* Physica Status Solidi (A) Applied Research, 2006. **203**(14): p. 3468-3475.
4. Bowers, M.J., J.R. McBride, and S.J. Rosenthal, *White-light emission from magic-sized cadmium selenide nanocrystals.* Journal of the American Chemical Society, 2005. **127**(44): p. 15378-15379.
5. Dukes, A.D., et al., *Pinned emission from ultrasmall cadmium selenide nanocrystals.* Journal of Chemical Physics, 2008. **129**(12): p. 121102.
6. Evans, C.M., et al., *Ultrabright PbSe magic-sized clusters.* Nano Letters, 2008. **8**(9): p. 2896-2899.
7. Ki, W. and J. Li, *A semiconductor bulk material that emits direct white light.* Journal of the American Chemical Society, 2008. **130**(26): p. 8114-+.
8. Qian, L., D. Bera, and P.H. Holloway, *Temporal evolution of white light emission from CdSe quantum dots.* Nanotechnology, 2008. **19**(28): p. 285702.
9. Schreuder, M.A., et al., *Encapsulated white-light CdSe nanocrystals as nanophosphors for solid-state lighting.* Journal of Materials Chemistry, 2008. **18**(9): p. 970-975.
10. Bowers, M.J., et al., *Structure and Ultrafast Dynamics of White-Light-Emitting CdSe Nanocrystals.* Journal of the American Chemical Society, 2009. **131**(16): p. 5730-+.
11. Brokmann, X., et al., *Statistical Aging and Nonergodicity in the Fluorescence of Single Nanocrystals.* Physical Review Letters, 2003. **90**(12): p. 120601.
12. Dabbousi, B.O., et al., *(CdSe)ZnS core-shell quantum dots: Synthesis and characterization of a size series of highly luminescent nanocrystallites.* Journal of Physical Chemistry B, 1997. **101**(46): p. 9463-9475.
13. Norris, D.J. and M.G. Bawendi, *Measurement and assignment of the size-dependent optical spectrum in CdSe quantum dots.* Physical Review B, 1996. **53**(24): p. 16338-16346.
14. Norris, D.J., et al., *Size dependence of exciton fine structure in CdSe quantum dots.* Physical Review B, 1996. **53**(24): p. 16347-16354.
15. Nirmal, M., et al., *Fluorescence intermittency in single cadmium selenide nanocrystals.* Nature, 1996. **383**(6603): p. 802.
16. Efros, A.L. and M. Rosen, *Random telegraph signal in the photoluminescence intensity of a single quantum dot.* Physical Review Letters, 1997. **78**(6): p. 1110.
17. Chepic, D.I., et al., *Auger ionization of semiconductor quantum drops in a glass matrix.* Journal of Luminescence, 1990. **47**(3): p. 113.
18. Klimov, V.I., et al., *Electron and hole relaxation pathways in semiconductor quantum dots.* Physical Review B, 1999. **60**(19): p. 13740-13749.

19. Klimov, V.I., *Optical nonlinearities and ultrafast carrier dynamics in semiconductor nanocrystals.* Journal of Physical Chemistry B, 2000. **104**(26): p. 6112-6123.
20. Krauss, T.D. and L.E. Brus, *Charge, Polarizability, and Photoionization of Single Semiconductor Nanocrystals.* Physical Review Letters, 1999. **83**(23): p. 4840-4843.
21. Krauss, T.D., S. O'Brien, and L.E. Brus, *Charge and photoionization properties of single semiconductor nanocrystals.* Journal of Physical Chemistry B, 2001. **105**(9): p. 1725-1733.
22. Kuno, M., et al., *Nonexponential `blinking' kinetics of single CdSe quantum dots: A universal power law behavior.* Journal of Chemical Physics, 2000. **112**(7): p. 3117.
23. Kuno, M., et al., *Modeling distributed kinetics in isolated semiconductor quantum dots.* Physical Review B: Condensed Matter, 2003. **67**: p. 125304.
24. Cichos, F., C. von Borczyskowski, and M. Orrit, *Power-law intermittency of single emitters.* Current Opinion in Colloid & Interface Science, 2007. **12**(6): p. 272-284.
25. Frantsuzov, P., et al., *Universal emission intermittency in quantum dots, nanorods and nanowires.* Nature Physics, 2008. **4**(7): p. 519-522.
26. Tang, J. and R.A. Marcus, *Diffusion-Controlled Electron Transfer Processes and Power-Law Statistics of Fluorescence Intermittency of Nanoparticles.* Physical Review Letters, 2005. **95**(10): p. 107401.
27. Tang, J. and R.A. Marcus, *Mechanisms of fluorescence blinking in semiconductor nanocrystal quantum dots.* Journal of Chemical Physics, 2005. **123**(5): p. 054704.
28. Frantsuzov, P.A. and R.A. Marcus, *Explanation of quantum dot blinking without the long-lived trap hypothesis.* Physical Review B: Condensed Matter, 2005. **72**: p. 155321.
29. Shimizu, K.T., et al., *Blinking statistics in single semiconductor nanocrystal quantum dots.* Physical Review B: Condensed Matter, 2001. **63**: p. 205316.
30. Issac, A., C.v. Borczyskowski, and F. Cichos, *Correlation between photoluminescence intermittency of CdSe quantum dots and self-trapped states in dielectric media.* Physical Review B: Condensed Matter, 2005. **71**: p. 161302.
31. Kuno, M., et al., *"On"/"off" fluorescence intermittency of single semiconductor quantum dots.* Journal of Chemical Physics, 2001. **115**(2): p. 1028-1040.
32. Verberk, R., A.M.v. Oijen, and M. Orrit, *Simple model for the power-law blinking of single semiconductor nanocrystals.* Physical Review B: Condensed Matter, 2002. **66**: p. 233202.
33. Tang, J., *The effects of anomalous diffusion on power-law blinking statistics of CdSe nanorods.* Journal of Chemical Physics, 2008. **129**(8): p. 084709.
34. Margolin, G., et al., *Power-Law Blinking Quantum Dots: Stochastic and Physical Models.* Fractals, Diffusion, and Relaxation in Disordered Complex Systems, Part A, 2006. **133**: p. 327-356.
35. Pólya, G., *Über eine Aufgabe der Wahrscheinlichkeitsrechnung betreffend die Irrfahrt im Straßennetz.* Mathematische Annalen, 1921. **84**(1): p. 149-160.
36. Kuno, M., et al., *Fluorescence intermittency in single InP quantum dots.* Nano Letters, 2001. **1**(10): p. 557-564.

37. Pelton, M., et al., *Evidence for a diffusion-controlled mechanism for fluorescence blinking of colloidal quantum dots.* Proceedings of the National Academy of Sciences of the United States of America, 2007. **104**(36): p. 14249-14254.
38. Tang, J., et al., *Short-time power-law blinking statistics of single quantum dots and a test of the diffusion-controlled electron transfer model.* Journal of Chemical Physics, 2009. **131**(6).
39. Heyes, C.D., et al., *Effect of the shell on the blinking statistics of core-shell quantum dots: A single-particle fluorescence study.* Physical Review B, 2007. **75**(12): p. 125431.
40. Koberling, F., A. Mews, and T. Basche, *Oxygen-induced blinking of single CdSe nanocrystals.* Advanced Materials, 2001. **13**(9): p. 672-676.
41. Kobitski, A.Y., C.D. Heyes, and G.U. Nienhaus, *Total internal reflection fluorescence microscopy - A powerful tool to study single quantum dots.* Applied Surface Science, 2004. **234**: p. 86-92.
42. Verberk, R., et al., *Environment-dependent blinking of single semiconductor nanocrystals and statistical aging of ensembles.* Physica E: Low-Dimensional Systems and Nanostructures, 2005. **26**(1-4): p. 19-23.
43. Gomez, D.E., et al., *Blinking and surface chemistry of single CdSe nanocrystals.* Small, 2006. **2**(2): p. 204-208.
44. Peterson, J.J. and D.J. Nesbitt, *Modified Power Law Behavior in Quantum Dot Blinking: A Novel Role for Biexcitons and Auger Ionization.* Nano Letters, 2009. **9**(1): p. 338-345.
45. Loudon, R., *The quantum theory of light*. 2003: Oxford University Press.
46. Schlegel, G., et al., *Fluorescence Decay Time of Single Semiconductor Nanocrystals.* Physical Review Letters, 2002. **88**(13): p. 137401.
47. Fisher, B.R., et al., *Emission intensity dependence and single-exponential behavior in single colloidal quantum dot fluorescence lifetimes.* Journal of Physical Chemistry B, 2004. **108**(1): p. 143-148.
48. Flomenbom, O., et al., *Stretched exponential decay and correlations in the catalytic activity of fluctuating single lipase molecules.* Proceedings of the National Academy of Sciences of the United States of America, 2005. **102**(7): p. 2368-2372.
49. Chen, X., *Ph.D. thesis*. 2007, University of Oxford.
50. Daniels, S.M., *Ph.D. thesis*. 2006, University of Manchester.
51. Gupta, J.A., et al., *Spin dynamics in semiconductor nanocrystals.* Physical Review B, 2002. **66**(12): p. 125307.
52. Crooker, S.A., et al., *Multiple temperature regimes of radiative decay in CdSe nanocrystal quantum dots: Intrinsic limits to the dark-exciton lifetime.* Applied Physics Letters, 2003. **82**(17): p. 2793-2795.
53. Rothe, C., S.I. Hintschich, and A.P. Monkman, *Violation of the exponential-decay law at long times.* Physical Review Letters, 2006. **96**(16): p. 163601.
54. Fonda, L., G.C. Ghirardi, and A. Rimini, *Decay Theory of Unstable Quantum Systems.* Reports on Progress in Physics, 1978. **41**(4): p. 587-631.
55. Bardou, F., *Lévy statistics and laser cooling : how rare events bring atoms to rest*. 2002, Cambridge: Cambridge University Press. xiii, 199 p.
56. Klimov, V.I., et al., *Quantization of multiparticle Auger rates in semiconductor quantum dots.* Science, 2000. **287**(5455): p. 1011-1013.

57. Tachiya, M. and K. Seki, *Unified explanation of the fluorescence decay and blinking characteristics of semiconductor nanocrystals.* Applied Physics Letters, 2009. **94**(8): p. 081104.
58. Wang, S., et al., *Fluorescence blinking statistics from CdSe core and core/shell nanorods.* Journal of Physical Chemistry B, 2006. **110**(46): p. 23221-23227.
59. Zhang, K., et al., *Continuous distribution of emission states from single CdSe/ZnS quantum dots.* Nano Letters, 2006. **6**(4): p. 843-847.
60. Verberk, R. and M. Orrit, *Photon statistics in the fluorescence of single molecules and nanocrystals: Correlation functions versus distributions of on- and off-times.* Journal of Chemical Physics, 2003. **119**(4): p. 2214-2222.
61. Chung, I.H. and M.G. Bawendi, *Relationship between single quantum-dot intermittency and fluorescence intensity decays from collections of dots.* Physical Review B, 2004. **70**(16): p. 165304.
62. Hollenbeck (1998), K.J., *INVLAP.M: A matlab function for numerical inversion of Laplace transforms by the de Hoog algorithm,* *http://www.isva.dtu.dk/staff/karl/invlap.htm*.
63. Yu, M. and A. Van Orden, *Enhanced fluorescence intermittency of CdSe-ZnS quantum-dot clusters.* Physical Review Letters, 2006. **97**(23): p. 237402.
64. Jones, M., S.S. Lo, and G.D. Scholes, *Quantitative modeling of the role of surface traps in CdSe/CdS/ZnS nanocrystal photoluminescence decay dynamics.* Proceedings of the National Academy of Sciences of the United States of America, 2009. **106**(9): p. 3011-3016.
65. Mueller, A.H., et al., *Multicolor Light-Emitting Diodes Based on Semiconductor Nanocrystals Encapsulated in GaN Charge Injection Layers.* Nano Letters, 2005. **5**(6): p. 1039-1044.
66. Konstantatos, G., et al., *Ultrasensitive solution-cast quantum dot photodetectors.* Nature, 2006. **442**(7099): p. 180-183.
67. Gur, I., et al., *Air-Stable All-Inorganic Nanocrystal Solar Cells Processed from Solution.* Science, 2005. **310**(5747): p. 462-465.
68. Potyrailo, R.A. and A.M. Leach, *Selective gas nanosensors with multisize CdSe nanocrystal/polymer composite films and dynamic pattern recognition.* Applied Physics Letters, 2006. **88**(13): p. 134110-3.
69. Klein, D.L., et al., *A single-electron transistor made from a cadmium selenide nanocrystal.* Nature, 1997. **389**(6652): p. 699-701.
70. Michler, P., et al., *Quantum correlation among photons from a single quantum dot at room temperature.* Nature, 2000. **406**: p. 968-970.
71. Lee, S., Y. Im, and Y.-B. Hahn, *Two-step growth of ZnO films on silicon by atomic layer deposition.* Korean Journal of Chemical Engineering, 2005. **22**(2): p. 334-338.
72. Gaponenko, S.V., *Optical properties of semiconductor nanocrystals*. Cambridge studies in modern optics. 1998, Cambridge: Cambridge University Press.
73. Cordero, S.R., et al., *Photo-Activated Luminescence of CdSe Quantum Dot Monolayers.* Journal of Physical Chemistry B, 2000. **104**(51): p. 12137-12142.
74. Mahler, B., et al., *Towards non-blinking colloidal quantum dots.* Nature Materials, 2008. **7**(8): p. 659-664.

75. Chen, Y., et al., *"Giant" multishell CdSe nanocrystal quantum dots with suppressed blinking.* Journal of the American Chemical Society, 2008. **130**(15): p. 5026-+.